A Square-Wave-Driven Radiofrequency Quadrupole Cooler and Buncher for TITAN

by

Mathew Jonathon Smith

B.Sc., The University of York, 2001

A THESIS SUBMITTED IN PARTIAL FULFILMENT OF
THE REQUIREMENTS FOR THE DEGREE OF

MASTER OF SCIENCE

in

The Faculty of Graduate Studies

(in Physics)

THE UNIVERSITY OF BRITISH COLUMBIA

June 13, 2005

Abstract

The TITAN (TRIUMF's Ion Trap for Atomic and Nuclear science) project at TRIUMF will use the unique combination of an Electron Beam Ion Trap (EBIT) charge state breeder and a precision Penning trap to carry out high accuracy mass measurements ($\delta m/m \approx 1\times10^{-8}$) on short-lived ($t_{1/2} \approx 50\,ms$) isotopes. In order to obtain fast and efficient charge state breeding it is necessary to inject a cooled and bunched beam into the EBIT. For radioactive isotopes this can be achieved by employing a segmented, gas-filled, RadioFrequency Quadrupole (RFQ). Such a device has been developed for use in the TITAN experiment. Previous RFQ coolers have been driven sinusoidally, however this device will be driven with a large amplitude ($\mathrm{V_{pp}} = 400\,V$) high frequency ($f = 1\,MHz$) square-wave. This makes a broadband, linear, cooling trap possible for the first time.

Using matrix methods the motion of ions in a square-wave-driven trap were studied and the acceptance and the space charge limit of the trap calculated as a function of the operating parameter, q. A simple viscous drag model for the cooling process was then used to prove the cooling concept. A Monte Carlo routine was developed and used to simulate the cooling of cesium ions in a helium buffer gas. At an operating parameter of $q = 0.4$ a cooling time of $600\,\mu s$ was found at a gas pressure of $2.5\times10^{-2}\,mbar$. The final temperature, T_f, of the ion cloud was found as a function of q (for $q < 0.4$, $T_f < 400\,K$). Ion optics for the injection and the extraction of ions from the trap were designed and simulated. Transverse rms emittances on the order of $3\,\pi\,mm\,mrad$ and longitudinal rms emittances on the order of $2\,eV\,\mu s$ for the extracted beam were demonstrated at an extraction energy of $2.5\,keV$.

Simulations of a previously designed and manufactured stable ion source system were carried out to try and match the emittance of the beam to the acceptance of the RFQ. Through a combination of simulation and experimental results it was shown that with minor modification the system would give a relatively good approximation to the actual radioactive ion beam produced at TRIUMF. Further simulations showed that an acceptance of 99.8% of the modified beam by the RFQ will be possible.

Contents

List of Tables

List of Figures

Acknowledgements

I would like to thank Dr. Jens Dilling. You took a chance on a student from the UK and have been paying for it ever since. Thank you for your continued support.

Second on the list comes Dr. Joe Vaz. It took a little longer than the year you predicted but we are finally getting there.

There have been a lot of students who have worked with me on this project I would like to thank them all sincerely for their help especially Laura Blomeley, Rob Cussons, Ori Hadary and Amar Kamdar (in no particular order). Thanks for not getting too mad when I pointed out what was wrong with what you were doing and not gloating too much when the shoe was on the other foot.

I should also like to thank Dr. Matthew Pearson I can't estimate the number of times your advice has proven to be invaluable.

There were also a large number of technical staff at TRIUMF who worked on this project: people from the controls group, the kicker group, the vacuum group, the machine shop, the design office, etc, etc. To name everyone who has helped with the project would take all day. I would especially like to thank Hart Sprenger for the design work he did for the RFQ and Mel Good for all his help in putting all the stuff together.

On a personal note I would like to thank my parents (both sets). I know that if I had done it in England I would have my Phd by now and I would have stopped being the financial burden that I continue to be. I would especially like to thank my father for helping me to realize that this was indeed what I wanted to do and encouraging me to follow the academic route rather than selling my soul to the Devil for the cash.

I suppose I better thank my brother and sisters too. If only for the fact that it won't be pleasant the next time I see them if I don't.

To my future mother and father inlaw Phyllis and Steve thank you for accepting me as part of your family. Steve without your priceless advice, "get it done, eh!", I don't know how I would have got through this. To Naomi your classic sense of humour never fails to bring a smile to my face, even after three months of corrections.

Finally to my future wife Masumi, I really cannot put into words how much your continued love and support has meant to me through out this ordeal. I think that it is fair to say that you really did save my thesis.

I said to him one day that the very slender reward which God had attached to the pursuit of serious inquiry was a sufficient proof that He disapproved of it, or at any rate that He did not set much store by it or wish to encourage it.

—Samuel Butler from The Way Of All Flesh.

Chapter 1

Introduction

The TITAN (TRIUMF's Ion Trap for Atomic and Nuclear science) experiment aims to use the unique combination of an Electron Beam Ion Trap (EBIT) and precision Penning trap to perform high precision mass spectrometry, ($\delta m/m \approx 1 \times 10^{-8}$), on short-lived ($t_{1/2} \approx 50\,ms$) radio-isotopes. This thesis details the design, simulation and construction of a square-wave-driven, gas-filled, RadioFrequency Quadrupole (RFQ) ion trap as well as further simulations of the optics required to inject/extract a stable ion beam into/outof the system. The RFQ will be used to prepare the radioactive ion beams produced at the ISAC (Isotope Separator and ACcelerator) facility, located at the TRIUMF National Laboratory in Vancouver, Canada, for injection into the EBIT.

In the first chapter an overview of the types of ion traps and typical experiments using them is presented. An introduction to the TITAN experiment is given including an overview of the ISAC facility, the motivation for high precision mass measurements, the motivation for building the RFQ and the system designed to test the RFQ. Chapters two and three detail the work done in the development of the RFQ design. Chapter two shows the mathematical treatment of an ion's motion in a square-wave-driven RFQ. This, combined with a simple damping model for the interaction of the ions with a buffer gas, is then used to prove the feasibility of the RFQ cooler. In the third chapter details and results of a Monte Carlo simulation used to model the ion-atom interaction in the RFQ and hence the cooling process are given. The necessary ion optics for injection and extraction of an ion beam from the system are also presented along with simulated properties of the extracted beam. Based on the results of the simulations the RFQ was designed and built the final design is shown along with details of the experimental setup. The penultimate chapter details simulations of the ion optics needed for the test stand. The simulated results are then compared to experimental results and based on the simulations improvements to the test ion source are suggested. The final chapter gives a summary of the work in this thesis.

1.1 Ion Traps and their Uses

Particles that carry electric charge feel forces due to electromagnetic fields. This fact is the underlying principle behind ion traps (devices that use electromagnetic fields to trap charged particles in two or three spatial dimensions). Such traps allow for the study of charged particles in a well defined environment,

making them ideal for precision measurements.

There are basically two different kinds of ion trap:

1. The Penning trap. This trap, developed by Hans Dehmelt on a Penning pressure gauge principle, uses a combination of electrostatic and magnetic fields in order to confine particles spatially.

2. The Paul trap. This trap provides confinement using electrodynamic fields. It is named after its inventor Wolfgang Paul who along side Hans Dehmelt won the 1989 Nobel prize in physics for their work with ion traps.

The principle of operation of both of these traps will be outlined in this section as well as a short overview of the science which can be done utilizing such devices. A brief review of square-wave-driven traps is also given.

1.1.1 Penning Traps

Consider an ion moving under the influence of a linear magnetic field with its velocity perpendicular to the magnetic field lines. The Lorentz force law, $F = q(\vec{E} + \vec{v} \times \vec{B})$, tells us that the ion will feel a force that will cause it to move on a circular path around the field lines. We can say that the effect of the linear magnetic field is to trap the ion in the two dimensional plane perpendicular to the field.

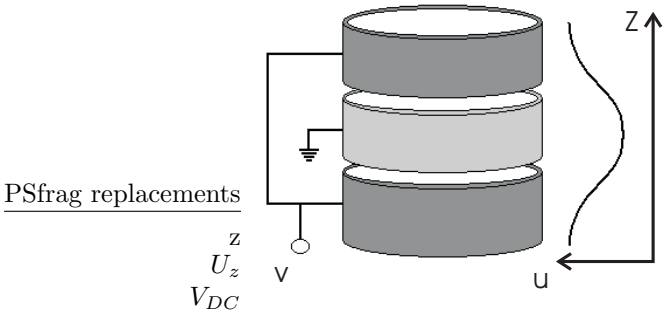

Figure 1.1: A simple cylindrical electrode geometry which can be used to trap ions in one dimension.

Now consider a positive ion inside the simple three electrode geometry shown in figure 1.1 with its velocity parallel to the z- axis. By the application of a positive potential, $+V_{DC}$, to the two end electrodes a one dimensional potential well can be formed. Positive ions placed at the center of the trap will be confined along the z- axis as long as their kinetic energy is less than $+V_{DC}$. This is an example of a simple one dimensional electrostatic trap. It is possible to imagine any number of electrode geometries that will provide a similar trapping potential but it is of note that Gauss' law, $\vec{\nabla} \cdot \vec{E} = 0$, tells us that it is not possible to trap ions in more than one dimension electrostatically (see figure 1.2).

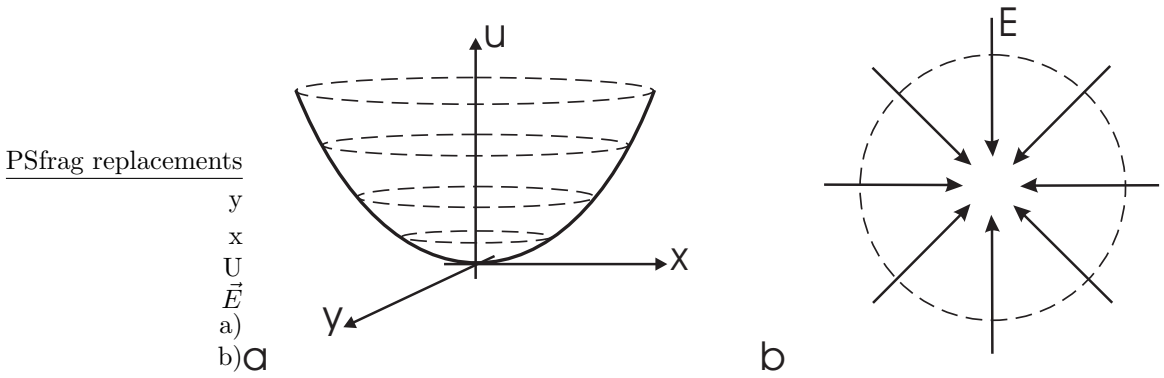

Figure 1.2: A typical two dimensional trapping potential (a) and the corresponding electric field lines (b). In order to obtain such a field it would be necessary to have a charge distribution at the potential minimum, however when trapping ions this is undesirable as the ions will be lost via collisions with the distribution.

The Penning trap uses the combination of a magnetic and an electrostatic field so as to trap ions in all three spatial dimensions. Although the electrode geometry used to provide the necessary electrostatic field is in theory somewhat arbitrary, in practice it is useful to choose a geometry which provides a field which can be easily analyzed. Modern Penning traps are in general categorized into two groups:

- Hyperbolic or Precision Penning Traps. These traps use a hyperbolic electrode configuration to form a harmonic potential such that the electrostatic force exerted on the trapped ions is proportional to the distance from the center of the trap (see figure 1.3). They are used in high precision experiments due to the mathematical simplicity of the fields produced inside.

- Cylindrical or Penning-Malmberg Traps. These traps use some variant on the cylindrical electrode geometry shown in figure 1.1. They offer the advantage that the cylindrical geometry is much easier to machine than the electrodes of the hyperbolic trap. The use of compensation electrodes inside such a trap make it possible to recreate with great accuracy the fields of the precision trap.

Penning traps are successfully used as mass spectrometers for both stable and short-lived ions (see appendix A) as well as for electrons, positrons, protons and anti-protons. Comparison between the mass of matter and anti-matter currently serves as the most precise test of CPT (Charge-Parity-Time) invariance [Blu98]. They have been used to create anti-hydrogen, by combination of positrons and anti-protons [Gab02] [Amo02]. It is hoped that in the future it

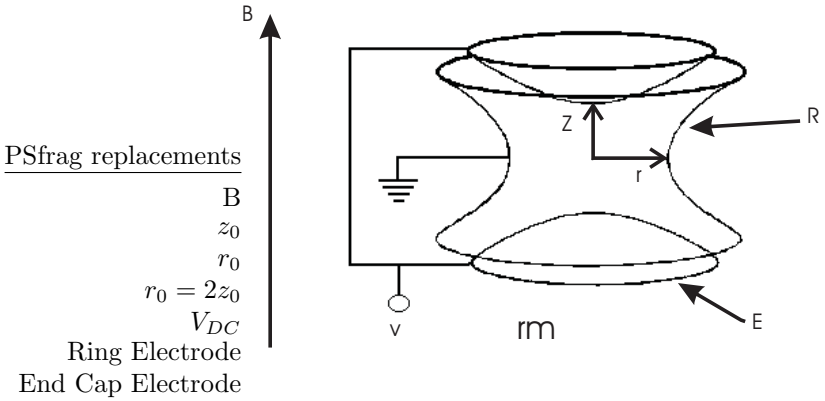

Figure 1.3: This hyperbolic electrode geometry very closely approximates the ideal harmonic potential along the z- axis.

will be possible to use a combination of neutral atom trapping techniques and ion trapping techniques to create and store anti-hydrogen. If this is achieved laser spectroscopy on the trapped anti-hydrogen would allow for further tests of CPT invariance. Bound electron g-factors can be measured using Penning traps. This allows for precise tests of bound-state QED [Wer03]. Ions in Penning traps can also be used as precision frequency standards leading to improved definitions of the S.I. second [Tan95].

1.1.2 Paul Traps

As previously stated it is impossible to trap ions electrostatically in more than one dimension. However, using electrodynamic fields it is possible to create a net focusing force on a charged particle and hence trap in more than one dimension. Consider the standard quadrupolar two dimensional electrode geometry shown in figure 1.4 with positive potential applied to one pair of opposing electrodes and an equal but opposite (negative) potential applied to the other pair of opposing electrodes. A positive ion inside this geometry will feel an attractive force due to the negative electrodes and a repulsive force due to the positive electrodes. This means that it will move toward one of the negative electrodes. If we switch the potentials on the electrodes, before the ion reaches the negative electrode, from positive to negative and vice versa the ion now moves towards one of the newly negative electrodes. By switching the potentials on the rods fast enough we can make it such that the ions never have enough time to reach any given electrode and are effectively trapped. This explanation is slightly simplistic in that it ignores the fact that the applied oscillating field also has the effect of driving the ion motion. However, by proper selection of the properties of the oscillating potential it is possible to trap ions in two dimensions. This kind of trap is known as a two dimensional or linear Paul trap. Due to

it quadrupolar structure this kind of trap is also known as an RFQ (RadioFrequency Quadrupole).

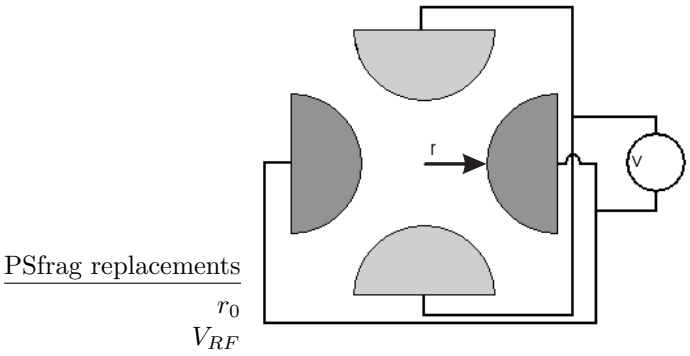

Figure 1.4: A two dimensional Paul trap in which ions can be trapped using RF fields.

The stability of an ions motion in the trap, i.e. whether an ion motion is bound or unbound, depends on the amplitude and frequency of the applied RF field, the size of the trap and the charge-to-mass ratio of the trapped species. The stability can also be affected by the application of a DC quadrupolar field to the trapping electrodes or, in the case of the square-wave-driven trap, by adjusting the duty cycle of the applied RF [Ric73]. Thus linear Paul traps are commonly used as mass filters [Daw95]. Such traps have been used as storage devices for simple quantum computers [Bin04] [Kep02]. As previously mentioned the use of gas-filled, linear Paul traps to improve beam quality at radioactive beam facilities has also been proven [Her01] [Nie01].

The extension of RF trapping to three dimensions is straight forward. Consider the geometry of the hyperbolic Penning trap. By taking the cross-section of this geometry in a plane parallel to the axial direction of the trap we obtain something similar to the two dimensional quadrupole above. The only difference being the ratio of the axial to the radial dimensions. Hence, by applying RF-fields to the ideal trap geometry we can trap ions in three dimensions. This kind of trap is known simply as a Paul trap.

Laser cooled ions in three dimensional RF traps, [Mon95], can be used in order to do precision laser spectroscopy [Tho94]. These traps have also been applied in the field of quantum computing and in the field of frequency standards [Tan03].

1.1.3 Square-Wave-Driven Traps

RFQ's use four rods driven with an RF potential in order to trap ions in two dimensions. One pair of rods has an applied potential that is 180° out of phase with the potential on the other pair. Traditionally such devices have been driven

with a sinusoidally varying RF potential. The potential is generated using an RF amplifier then ferrite cores are used to split the phase of the field before it is applied to the trap electrodes (see figure 1.5).

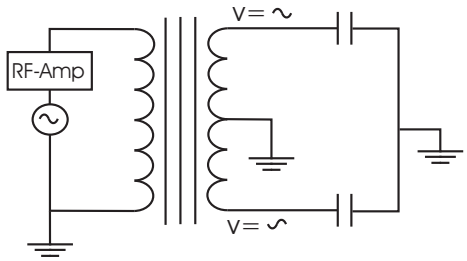

Figure 1.5: A schematic of a traditional sinusoidal driving system. The phase of the amplified RF is spilt using an inductor before being applied to the RFQ rods. The rods present an effective capacitance to ground.

The stability of an ion's motion in an RFQ is dependent both on the amplitude and the frequency of the applied potential, as well as on the charge-to-mass ratio of the ion. It is desirable to keep the amplitude of the RF as large as possible as this increases the depth of the trapping potential and hence the transfer efficiency of the trap (this is particularly important for radioactive ions because they are difficult to produce). Ferrite cores often have small bandwidths. Driving a core off resonance causes a large amount of energy to be dissipated in the core itself. This in turn heats the core, changing its magnetic properties. This leads to a distorted induced signal with a reduced amplitude. Thus, for a given ferrite, it is only possible to trap ions over a limited mass range whilst still maintaining a suitable trapping potential.

A square-wave-driven linear Paul trap was first demonstrated by J. A. Richards [Ric73]. Using bipolar junction transistors a square-wave of $80\,V$ maximum peak-to-peak amplitude was generated at frequencies of up to $1\,MHz$. This was used to drive a small quadrupole for use as a mass filter. The use of square-waves eliminates the need for ferrite cores and as such it is possible to build a broadband trap. More recently the cooling and bunching of ion beams in a square-wave-driven three dimensional Paul trap has been demonstrated by the CPT (Canadian Penning Trap) group at the ANL (Argonne National Laboratory) [Vaz02]. Using two fast switching MOSFETs in a push-pull configuration, the group was able to create a square-wave with a peak-to-peak amplitude of $100\,V$ at frequencies of up to $300\,kHz$. A number of papers have also recently appeared on the use of square-wave-driven ion traps as mass filters from the Shimadzu research laboratory in the UK (see for example [Sud02] or [Din02]) where three dimensional Paul traps were driven with $500\,V$ peak-to-peak amplitude at up to $1\,MHz$.

The main limiting factor in square-wave generator design is the energy dis-

sipated in the switching transistors. This energy scales linearly with the capacitance of the driven system. An RFQ cooler and buncher is typically much larger than any previous square-wave-driven system and hence presents a larger capacitive load. For this reason a square-wave-driven RFQ cooler and buncher has been heretofore unrealizable experimentally. However, it was realized that existing technology at TRIUMF developed by the KICKER group, for the MuLan experiment [Bar03], could be adapted in order to make a square-wave generator to drive such a trap. The group had previously developed a method for stacking MOSFETs such that the total energy dissipated in each chip was reduced. Initially the driver was commissioned to operate at $400\,V_{pp}$ switching at frequencies of up to $1\,MHz$ (for a description of the driving system see appendix C). Modifications are currently underway to upgrade the system such that it will be able to switch voltages of up to $1\,kV$ at frequencies up to $3\,MHz$.

1.2 The TITAN experiment

1.2.1 Overview of the TITAN Experiment

As previously stated the ultimate goal of the TITAN experiment is to carry out high precision mass spectrometry, ($\delta m/m \approx 1 \times 10^{-8}$), on short-lived ($t_{1/2} \approx 50\,ms$) radio-isotopes.

To date the most accurate mass measurements have been carried out using Penning trap mass spectrometers. In such devices the mass of the ion is deduced by measuring it's cyclotron frequency, ω_c, and using the fact that:

$$\omega_c = \frac{q}{m} B, \tag{1.1}$$

where q is the ions charge, B is the strength of the applied magnetic field and m is the ions mass (a detailed description Penning trap mass spectrometry is given in appendix A). The uncertainty associated with the measurement of the cyclotron frequency can be used to obtain an expression for the ultimate possible accuracy of Penning trap mass measurements as: [Bol01]:

$$\frac{\delta m}{m} \simeq \frac{m}{TqBN^{\frac{1}{2}}}, \tag{1.2}$$

where N is the number of ions detected and T is the observation time for ions in the trap.

For stable ions high resolution can be obtained by increasing the observation time. However, for short-lived ions this is not possible and at present the experimentally achieved resolution is on the order of 5×10^{-8} (see appendix A for an overview of existing facilities for Penning trap mass spectrometry). In order to improve this accuracy one can therefore either increase the number of observations (normally limited by the yield of the required ion species and the beam time available at on-line facilities), increase the magnetic field strength (technically very difficult beyond around $10\,T$) or increase the charge state of the ion to be measured (see figure 1.6).

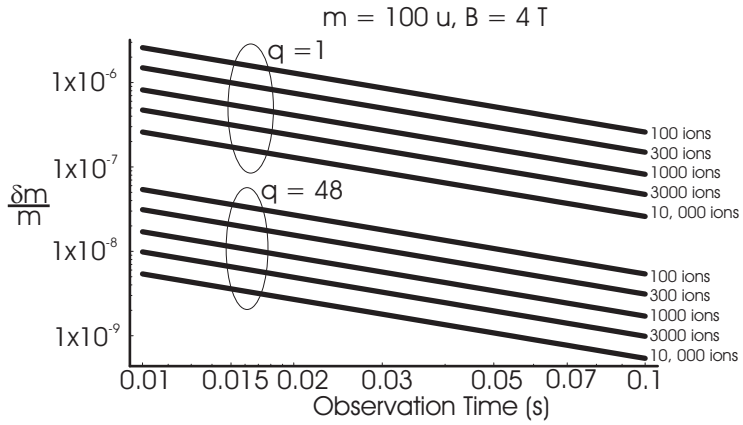

Figure 1.6: Comparison between the accuracy in mass measurement for singly and highly charged ions in a $4\,T$ Penning trap for given numbers of observed ions.

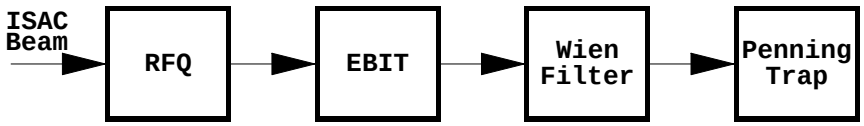

Figure 1.7: Overview of the TITAN experiment.

An overview of the proposed stages of the TITAN experiment is shown in figure 1.7. The continuous, low energy ($E \leq 60\,keV$) ISAC beam will be cooled and bunched by the RFQ. The ion bunches will then enter an EBIT for charge state breeding. The Wien velocity filter will be used to select a particular charge-to-mass ratio of the highly charged ions before they enter a $4\,T$ Penning trap where the mass measurement will be made. For the first time TITAN will be able to perform mass spectrometry on highly-charged, short-lived ions. Equation 1.2 can be used in order to compare the ultimate accuracy possible for mass measurements at TITAN and those made at other systems (see figure 1.8). For singly charged ions TITAN's resolution is worse than that at other systems. However, for highly charged ions (only available at TITAN) the resolution is much better than that achievable at other facilities.

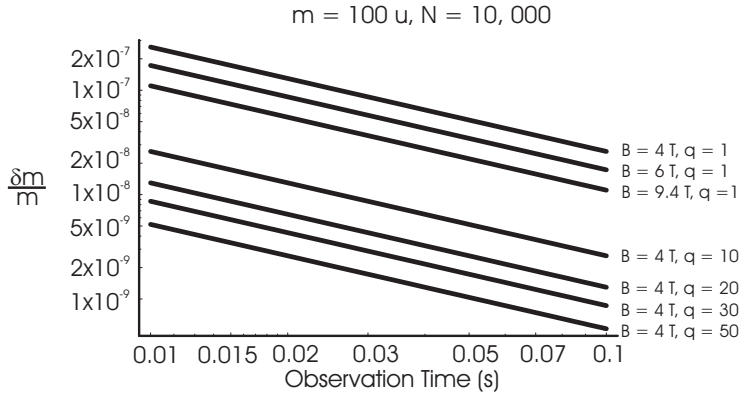

Figure 1.8: Comparison of the maximum possible accuracy in mass measurements for 10,000, mass 100 ions in TITAN's $4\,T$ Penning trap with those made at other facilities with $6\,T$ (ISOLTRAP, SHIPTRAP, JYFLTRAP and CPT) and $9.4\,T$ (LEBIT) Penning trap systems.

1.2.2 The ISAC Facility at TRIUMF

The ISAC (Isotope Separator and ACcelerator) facility produces radioactive ions for use in a variety of different experiments using the ISOL (Isotope Separator On Line) method [Dom02]. The proton beam produced by the TRIUMF (TRI-University Meson Facility) cyclotron ($I \leq 100\,\mu A$, $E = 500\,MeV$) impinges on a solid target. At these energies nuclear reactions such as spallation and fragmentation take place and radioactive species are produced. These nuclei diffuse out of the target, are ionized, and are subsequently electrostatically accelerated to around 30 to $60\,keV$. A two stage magnetic dipole separator is then used to select ions with a specific charge-to-mass ratio which are delivered to the experimental area (see figure 1.9).

The ISAC facility uses a number of different targets in order to provide a

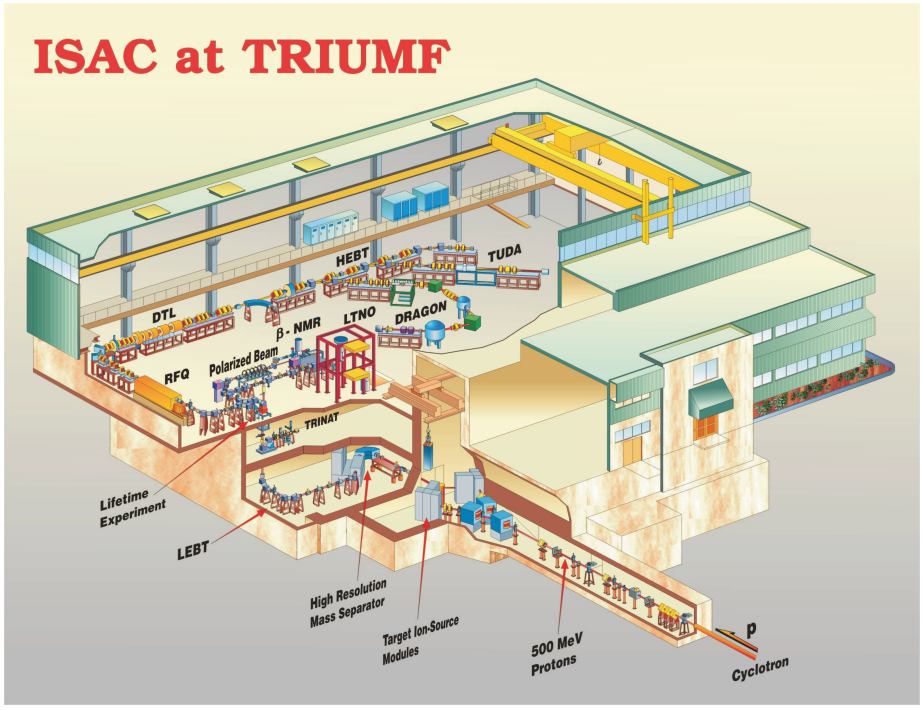

Figure 1.9: Overview of the ISAC facility. The TITAN experiment will be installed in the low energy area (i.e. before the RFQ accelerator) on a platform above the polarized beam line.

large variety of different species of radioactive ions. The facility will allow for beams with $A \leq 235$ to be delivered to a low energy, $E \leq 60\,keV$, experimental area. Further acceleration of the beam is achieved using a $35.4\,MHz$ RFQ linear accelerator which can accelerate beams with $A/q \leq 30$ from an energy of $2\,keV/u$ to $153\,keV/u$ and an addition $106\,MHz$ variable energy Drift Tube Linac (DTL) which can accelerate beams with $3 \leq A/q \leq 6$ to energies of $1.8\,MeV/u$. The device detailed in this work has been designed to be installed in the low energy experimental area.

1.2.3 Motivation for High Precision Mass Measurements on Short-Lived Nuclei

There are various interests in high precision ($\delta m/m \approx 1 \times 10^{-8}$) mass measurements. In the following we explain in some detail three fields in which it is hoped the TITAN experiment will be able to make major contributions:

Weak Interaction Studies

The Standard Model of particle physics has been enormously successful in describing the interactions of fundamental particles with each other. Up until very recently the predictions of the Standard Model have been in agreement with experiment. However, as experimental methods get more and more precise gaps between the predictions and experimental results are starting to appear. One such gap is the suggestion of non-unitarity of the CKM matrix (Cabbibo-Kobayashi-Maskawa) which if confirmed could provide evidence of physics beyond the Standard Model [Tow03].

The matrix links the weak eigenstates of the quarks to their mass eigenstates. In the Standard Model it is possible for a quark in one family to decay into a quark of another family via the weak interaction. Quantum mechanically this process can be described using the following idea: the weak eigenstates that the W and Z bosons see are rotations of the mass eigenstates that photons and gluons see, *i.e.* that the weak interaction has a different basis than that of the electromagnetic and strong interactions. The CKM matrix describes the mixing of weak and the mass eigenstates [Kob73]:

$$\begin{pmatrix} d_w \\ s_w \\ b_w \end{pmatrix} = \begin{pmatrix} V_{ud} & V_{us} & V_{ub} \\ V_{cd} & V_{cs} & V_{cb} \\ V_{td} & V_{ts} & V_{tb} \end{pmatrix} \cdot \begin{pmatrix} d_s \\ s_s \\ b_s \end{pmatrix}, \tag{1.3}$$

where V_{ud} etc are the so called mixing angles between the mass and the weak bases. The Standard Model puts certain constraints on this matrix. One constraint is that the sum of the squares of the elements in any given row should be equal to one. This can easily be understood as the square of each of the mixing angles is the probability that one particle will decay to another via the weak interaction *e.g.* V_{ud}^2 is the probability for an up quark to decay into a down quark. If the Standard Model accounts for all existing quarks we would

expect that the sums of the probabilities for an up quark to decay into some other particle to be equal to one i.e. for $V_{ud}^2 + V_{us}^2 + V_{ub}^2 = 1$.

Current experimental results give the values for the mixing angles as [Eid04]:

$$\begin{pmatrix} 0.9738 \pm 0.0005 & 0.2200 \pm 0.0026 & 0.0037 \pm 0.0005 \\ 0.224 \pm 0.012 & 0.996 \pm 0.013 & 0.0413 \pm 0.0015 \\ 0.0094 \pm 0.0046 & 0.040 \pm 0.003 & 0.9991 \pm 0.0001 \end{pmatrix}, \tag{1.4}$$

which for the first row yields [Tow03]:

$$V_{ud}^2 + V_{us}^2 + V_{ub}^2 = 0.9967 \pm 0.0014, \tag{1.5}$$

which disagrees with unity by more than two standard deviations. The value for V_{ud} is obtained from nuclear beta decay studies, V_{us} from Kaon decays and V_{ub} from B meson decays. Although the error in V_{ud} is around five times smaller than that in V_{us}, V_{ud} itself is approximately five times larger than V_{us}. This means that the error in the values of V_{ud}^2 and V_{us}^2 are of the same order of magnitude. Hence, the uncertainty that exists in the value for V_{ud} could potentially account for the deviation from unity. In order to test this result to better statistical accuracy it is felt that an improvement in the value for V_{ud} is needed.

In the Fermi theory of beta decay the relative strength of a decay is described using the statistical weight function or *ft*-value, where f is the energy dependant Fermi integral (or phase space factor) and t is the half-life of the decay. In practice f is determined by measuring the Q-value for the decay (i.e. the masses of the parent and daughter nuclei). This *ft*-value is solely dependent on the nuclear matrix element M_{fi} [Kra88]:

$$ft = \frac{K}{g^2 |M_{fi}|^2}, \tag{1.6}$$

where g is the weak coupling constant and K is a numerical constant. M_{fi} is dependant on the overlap of the initial and final nuclear wavefunctions.

In the superallowed $J^\pi = 0^+ \rightarrow 0^+$ beta decay process the spin-parity, J^π, and isospin, I, of the mother and daughter nuclei are the same ($\Delta I = \Delta J = 0$). This means that the total spin of the emitted electron and neutrino must be equal to zero, *i.e.* their spins are aligned anti-parallel. Fermi's original theory of beta decay (1934) only considered the possibility of a vector perturbation to the nuclear hamiltonian, this lead to the selection rule that the total change in spin, ΔJ, must equal zero [Fer34]. In 1936 Gamow and Teller modified Fermi's theory to include the effects of nuclear spin such that $\Delta J = 0, 1$ could be considered where $J = 0 \rightarrow 0$ transitions are not allowed [Gam36]. This is now understood as the perturbing potential in nuclear beta decay having both a vector and an axial-vector component where the vector component is responsible for the Fermi type transitions ($\Delta J = 0$) and the axial-vector component is responsible for Gamow-Teller type transitions ($\Delta J = 0, 1$ and $J = 0 \nrightarrow 0$). The $0^+ \rightarrow 0^+$ superallowed beta decay is therefore a pure Fermi transition and can

be described by considering only the vector component of the weak interaction.

$$ft = \frac{K}{G_V^2 |M_{fi}|^2}. \tag{1.7}$$

The value of V_{ud} can then be extracted by comparing the relative strength, G_V, of the beta decay with the Fermi coupling constant, G_F, obtained through studies of muon decays [Wil03]:

$$G_V = |V_{ud}| G_F. \tag{1.8}$$

In a superallowed decay the initial and final wavefunctions have the same quantum numbers. Thus, the initial and final nuclear states are completely superimposed. If we assume that the nuclear matrix elements are independent of the nuclear composition then the *ft*-values for all these decays should be the same. This is known as the Conserved Vector Current (CVC) hypothesis. It assumes that there is no coupling between the vector component of the weak interaction and the strong interaction. Thus it is possible to determine V_{ud} by measuring *ft*-values for a number of superallowed beta emitters.

This theory, however, is not correct in that it assumes that the nuclear matrix elements are completely nucleus independent, which they are not. It is necessary to apply corrections to measured *ft*-values in order to obtain G_V such that [Tow03]:

$$\mathscr{F}t = ft(1 + \delta_R)(1 - \delta_C) = \frac{K}{G_V^2 (1 + \Delta_R^V) |M_{fi}|^2}, \tag{1.9}$$

where δ_R and Δ_R^V are nucleus-dependent and nucleus-independent radiative corrections respectively and δ_C is a charge dependant correction due to isospin symmetry breaking.

$\mathscr{F}t$ values for nine $J^\pi = 0^+ \rightarrow 0^+$ transitions have been measured to high accuracy (≈ 0.1 % precision). The results of which are summarized in Figure 1.10 and give the result [Tow03]:

$$\overline{\mathscr{F}t} = 3072.3 \pm 2.0, \tag{1.10}$$

leading to the value of V_{ud} previously given. These results appear to be in good agreement with each other and provide verification of the CVC hypothesis at the 3×10^{-4} level.

Now we come back to the problem of the non-unitarity of the CKM matrix. The majority of the error in the value for V_{ud} isn't in fact due to experimental error. It instead comes from uncertainties in the calculations of Δ_R^V and δ_C. Although the value of Δ_R^V can only be improved by better understanding of theory, the value of δ_C can be improved with the aid of experiment. In order to obtain better statistical uncertainty in δ_C it will be necessary to measure the masses of a number of extra superallowed beta emitters to high precession ($\delta m/m = 1 \times 10^{-8}$). Although this precision in mass measurement is now standard for longer lived nuclei it is currently impossible for some of the short-lived ($t_{1/2} \approx 50\, ms$) radioactive isotopes required.

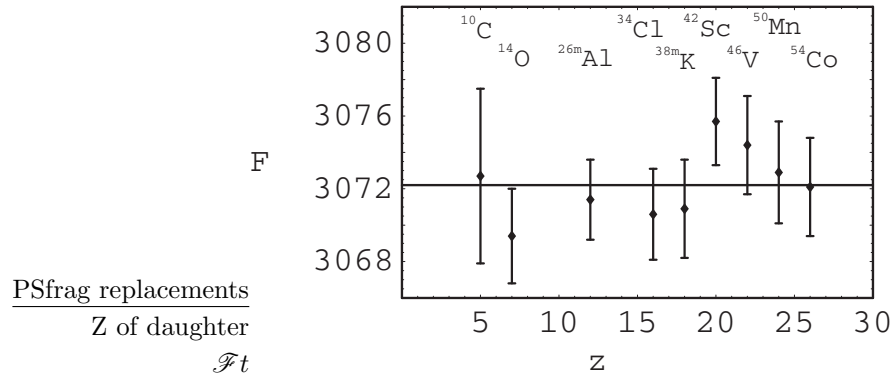

Figure 1.10: $\mathscr{F}t$ values for nine superallowed beta emitters, the solid line is a fit based on a least squares optimization using one parameter. Values taken from [Tow03].

Nuclear and Atomic Mass Models and Formulae

A number of models for the prediction of nuclear and atomic masses exist (for a very detailed summary see [Lun03]). Such models are needed when experimental results can't be obtained, either because the element under consideration can't be produced in large quantities or because the element has such a short lifetime it is impossible to carry out any kind of precise measurement on it. All of these models give good agreement when applied to nuclei with known masses. However, when using each model to predict the experimentally unknown masses of nuclei close to the proton or neutron drip lines, results are obtained which seem to diverge (see figure 1.11). Extending the range of known masses close to the drip lines, *i.e.* for nuclei with extreme isospin which are usually short-lived, will help to constrain these models and hence improve their accuracy.

Stellar Processes and Element Nucleosynthesis

Production of all the heavy elements (A $\geq$ 7) take place via nuclear reactions in the stars. In order to understand the complex chains of nuclear reactions that can take place inside a star, *e.g.* the s-, p-, r- and the rp- processes (see figure 1.12 and for an overview of these processes see [Lan04] or [Rol88]), it is necessary to know the masses of the nuclei involved or the Q-value for each reaction. Such chains involve a large number of short-lived nuclei which lie close to the proton and neutron drip lines.

1.2.4 Motivation for the RFQ

The TITAN project will use an EBIT (Electron Beam Ion Trap) in order to charge state breed the ions produced at the ISAC facility. Due to the hot envi-

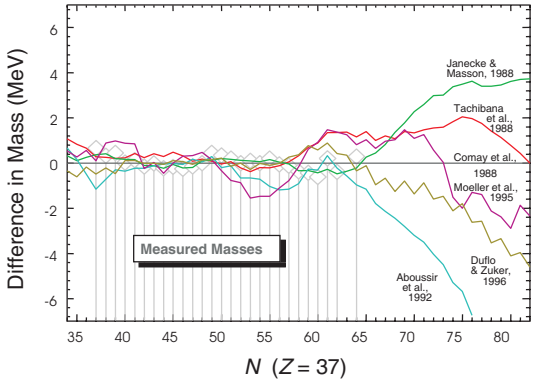

Figure 1.11: Difference in the mass predicted by different theoretical models for the mass of some isotopes of Rubidium. For N $\leq$ 64 experimental masses are known and the agreement between models is good, for N $>$ 64 the models diverge. Courtesy of D. Lunney.

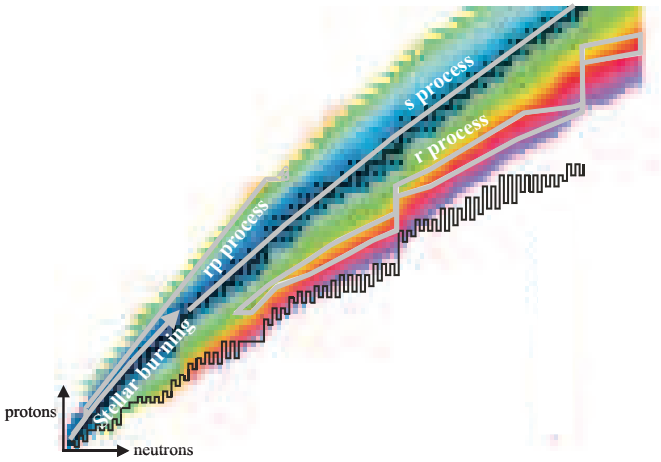

Figure 1.12: Chart of the nuclei with some of the major pathways for stellar nuclear synthesis shown. Taken from [Lan04].

ronment where the ions are produced (the target is heated by the high intensity, high energy proton beam from the TRIUMF cyclotron to around 2000 °C) the ISAC beam can have large transverse emittances ($\varepsilon_{99\%} = 50\,\pi\,mm\,mrad$). Also, the ion production method is continuous and as such so is the ISAC beam. As we will see these beam properties do not overlap well with the acceptance of the EBIT. The electrode geometry for an EBIT is similar to that of a cylindri-

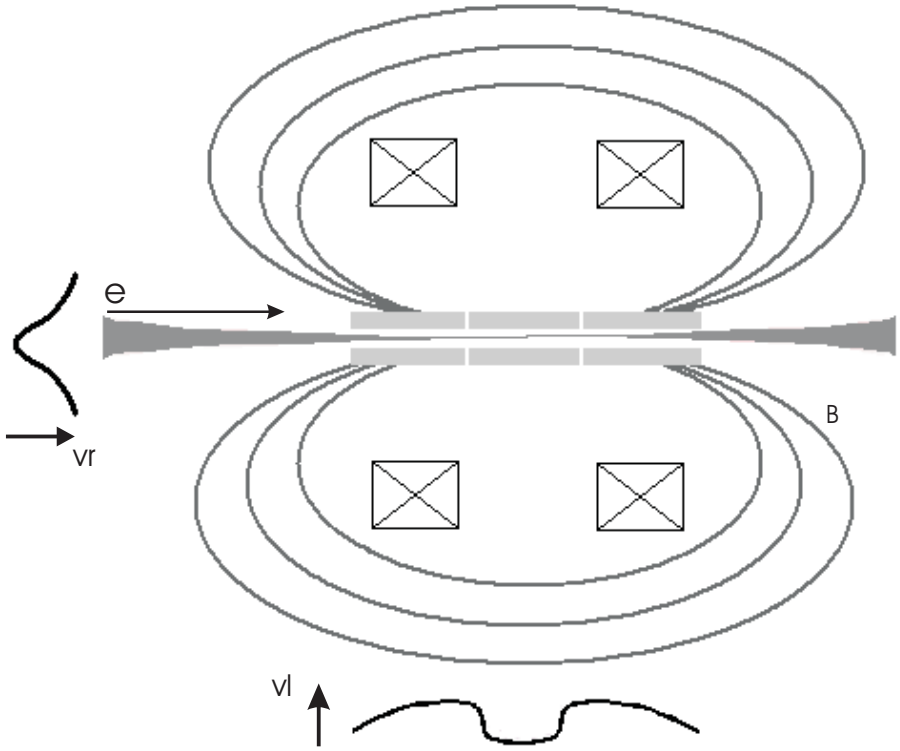

PSfrag replacements
V_r
V_l
electron beam
$\vec{B}$

Figure 1.13: Schematic of an EBIT. The radial trapping potential, V_R, is provided both by the magnetic field and the space charge potential of the electron beam. The longitudinal potential, V_L, is provided by electrostatic elements. The electron beam is sufficiently energetic, $E \approx 60\,keV$, that the small longitudinal potential, $E \approx 100\,eV$, has little effect on it.

cal Penning trap (see figure 1.13). The magnetic field confines a high current, $I \approx 5\,A$, electron beam that runs down the traps center. Radial trapping of positive ions is provided by a combination of the applied magnetic field and the Coulomb force due to the electron beam. Once the ions are in the trap they are stripped of electrons via successive impacts with the electron beam. This happens as long as the kinetic energy of the electron beam is higher than the

atomic binding energy of the electrons.

A simple loading scheme for such an EBIT is shown in figure 1.14. The system has an acceptance in energy-time phase space which does not overlap with the properties of the continuous ISAC beam. If a continuous ion beam is incident on the trapping region the second barrier will act so as to stop the beam thus making no use of the remaining ions. Also, in an EBIT the highly charged ions are extracted along the same path which they used to enter the trap, i.e. along the same path used by the incoming beam. Thus to make efficient use of the ISAC beam it is clear that it needs to be converted from a continuous beam into a bunched beam.

Ions are injected into the EBIT along the axis of the electron beam, this means that they must traverse the magnets fringe field. The homogeneity of the magnetic field worsens as a function of the radial displacement from the center of the trap and as such it is desirable to inject the ion bunch with a width that is as small as possible. Although the beam can be focused down into a narrow region of space, conservation of emittance tells us that this will make the beam divergent. It is not possible to inject a highly divergent beam into the EBIT as it will be reflected by the magnetic fringe field. Hence, the beam entering the EBIT must have a small emittance such that it can have both a small width and a small divergence. Thus, in order to achieve efficient transfer of the ISAC beam into the EBIT it is necessary for the beam to be both bunched and have a reduced emittance, or in other words to be cooled.

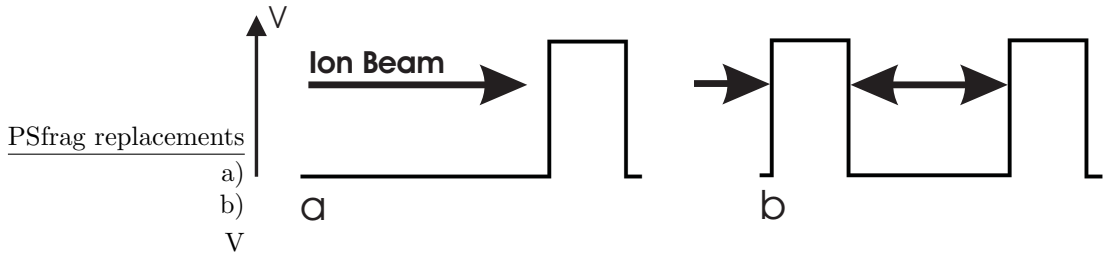

Figure 1.14: a) An ion beam enters the trapping region and is reflected off of an electrostatic barrier. b) A second barrier is then raised before the reflected ions can leave the trap, a small bunch of ions is thereby contained in the trapping region.

The emittance of an ion beam is conserved under the application of conservative forces (see appendix B.1). However, it is possible to reduce the emittance of an ion beam via the application of non-conservative forces, e.g. by collisions with a buffer gas. Consider an ion beam impinging on an infinitely long chamber filled with a dense gas. The ion beam will lose energy via collisions with the gas, eventually cooling to the ambient temperature of the gas. This process will eventually lead to the loss of the ion beam as the scattering will act so

as to thermalize the ions in all three dimensions (ignoring other possible loss processes such as charge exchange). The loss of velocity of the beam in the common direction of motion can be countered via the application of an accelerating electric field. However, this in itself does not necessarily lead to a reduction of the emittance of the ion beam. Although the velocity of the ions perpendicular to the common direction of motion will be reduced via buffer gas damping, seemingly leading to a reduction in emittance, scattering of the ions forward momentum into the transverse direction acts to counter this effect causing the ion beam to expand radially. This can lead to a net increase of the beam's emittance or worse to the loss of the ion beam. Therefore, in order to reduce an ion beam's emittance via buffer gas cooling it is necessary to provide a force that counteracts the radial expansion. An RFQ can be used to provide such a force making the buffer gas cooling of ion beams possible.

1.2.5 The RFQ Test System

In order to test the operation of the RFQ it has been setup on an off-line test stand with its own stable ion source (see figure 1.15). The purpose of the test stand is to provide a stable beam with properties similar to those of the ISAC beam in order to test the injection, cooling and extraction of ions from the RFQ.

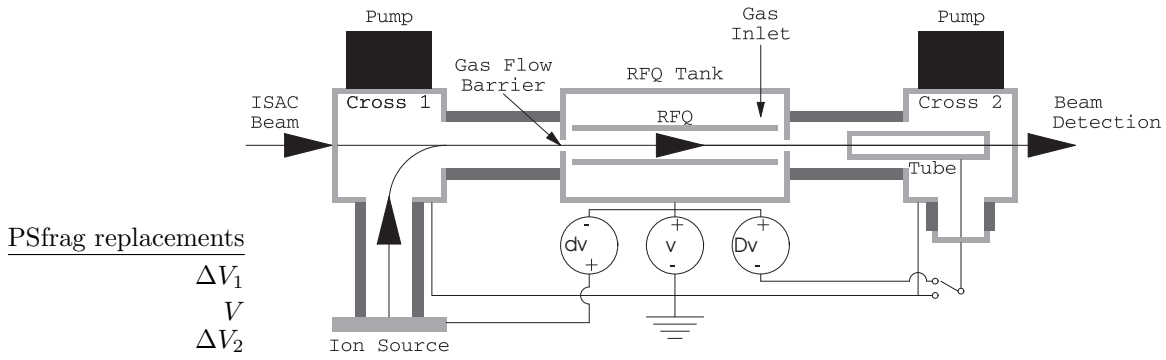

Figure 1.15: The TITAN RFQ test setup.

The low energy ISAC beam can be extracted with energies in the range of 30 to 60 keV. A typical gas filled trap can cool beams with incoming energies in the range of 30 to 100 eV. This means that the ISAC beam must be decelerated before it enters the beam cooling system. This will be achieved by floating the RFQ at a potential close to that of the initial kinetic energy of the beam. Thus, the RFQ must sit in a vacuum tank that is electrically isolated from the incoming beam line. Two commercially available alumina-silicate beam pipes are used to provide this isolation for the test system. Vaccum pumping is achieved by the mounting of a 1000 l/s pump at either end of the system on two custom made crosses. One cross allows for the mounting of a small cesium ion source at 90°

to the RFQ which is used to test the cooling system. The source is isolated from the main beam line using an alumina-silicate beam pipe, and is floated at a potential slightly higher than the RFQ tank. This allows for the beam to be accelerated toward the cross, which sits at ground potential, before being bent through 90° and decelerated as it heads towards the RFQ. On the extraction end the ion bunch is accelerated toward a long tube at a potential equal to the required extracted beam energy below the RFQ box (typically on the order of $2\,\text{to}\,3\,kV$). Once the bunch is inside the tube its potential can be switched to ground and thus the bunch leaves the tube at ground potential with the same kinetic energy with which it entered the tube.

1.3 Contributions of this Thesis

The work done for this thesis has made four major contributions to the TITAN project:

1. Properties of TITAN's RFQ from Theoretical Considerations. The theory of ion motion in a square-wave-driven trap has been previously developed in order to analyze the operation of square-wave-driven quadrupole mass filters(see for example [Ric73] or [Kon02]). This theory was used to derive some useful properties of TITAN's RFQ including the traps acceptance and space charge limit. Combined with well know results from statistical physics the theory was also used to give a definition of temperature in the ion trap.

2. Simulations of the Cooling Process in a Square-Wave-Driven RFQ. Numerous studies, both simulated and experimental, of the cooling process in sinusoidally-driven systems have been carried out (*e.g.* see [Her01], [Kim97] or [Par95]). However, no such studies on square-wave-driven systems have previously been done. There are two predominate methods for modelling ion beam cooling in an RFQ trap. The first uses a simple damping force to simulate the effects of the gas. This method reveals nothing about the final properties of the cooled ions as each ion is treated identically, however it can be useful when determining the ranges and cooling times of ions in the gas and is used in chapter two. The second method uses Monte Carlo techniques to model the collisions of the ion with the gas atoms either using hard-sphere or known ion-atom interaction potentials. As this method treats each ion individually it can be used to predict the final properties, *e.g.* the temperature, of a cooled ion cloud in a trap.

   The motion of ions in a Paul trap can be considered to be that of a simple harmonic macromotion perturbed by a higher frequency coherent micromotion, the latter is the result of the ions coupling to the applied RF field. Although instantaneously an ion in the trap has energy due to the micromotion, in the absence of interactions with other particles no net energy is gained over one period of the RF. However, if the ion does interact with other particles in the trap, *e.g.* a buffer gas, then

scattering can lead to the ions gaining energy from the micromotion. This effect is known as RF heating. There is no simple model for predicting the amount of RF heating in a gas-filled trap however the Monte Carlo method using realistic ion-atom interaction potentials has previously been used successfully to predict the final temperature of ions in a sinusoidally driven trap to within 17% of obtained experimental results [Kim97]. These simulations showed that with the proper choice of buffer-gas and buffer-gas pressure it was possible to cool an ion cloud in a sinusoidal trap to within a factor of two of the ambient temperature of the gas.

A Monte Carlo algorithm was developed as part of this thesis in order to study the effect of RF heating in a square-wave-driven trap. As no data, simulated or experimental, exists for buffer-gas cooling in a square-wave-driven RFQ these simulations were vital in determining the effects of RF heating in such traps. These simulations were important as the benefits of broadband operation associated with square-wave traps would be nullified if beam cooling comparable to that in sinusoidal-traps could not be achieved.

3. Development of Injection and Extraction Optics. The ISAC beam must be electrostatically decelerated from a typical transport energy of $40\,keV$ down to an energy in the range of 30 to $150\,eV$ before injection into the RFQ. At the same time the beam must be focused through a small aperture designed to allow for differential pumping between the RFQ and the rest of the ISAC beam line. The emittance of the decelerated beam must also match the acceptance of the RFQ. The $40\,keV$ ISAC beam has typical 99% transverse emittances on the order of $50\,\pi\,mm\,mrad$ and an energy spread of $5\,eV$. A system of deceleration optics that could accept a beam with this emittance was developed.

   Ion optics were also required in order to focus the cooled ions on extraction from the RFQ. A design for these optics was also developed and the extraction of ions from the trap in the presence of buffer gas was simulated.

4. Simulations of the Coupling of the RFQ to the Test Ion Source. The ion optics for a test ion source had previously been designed. Simulations were carried out of the ion source beam line in order to find the best match between the test ion beam and the deceleration optics for the RFQ. The simulations were also used to diagnose experimentally observed losses in the test ion system and to suggest improvements to the system such that a good approximation to the ISAC beam could be obtained.

Chapter 2

Square-Wave-Driven RFQ with Damping

In this chapter first we develop a mathematical description of the motion of ions in the square-wave-driven trap. A definition of the temperature of an ensemble of ions in the square-wave-driven trap is then presented. A simple viscous drag model is used to study the motion of ions in a gas-filled trap and prove the cooling concept. Finally the acceptance of the trap is calculated, the results from which are then used to calculate the space charge limits of the trap.

2.1 Ion Motion in a Square-Wave-Driven RFQ

An ion trap works by applying a net force on the ions that pushes them towards the center of the trap. The simplest such force is one that varies linearly with distance from the center of the trap. If we define the center of the trap as $(x, y) = (0, 0)$ with trapping provided in the xy- plane then such a force can be represented as:

$$\vec{F}(x, y) = ax\hat{\boldsymbol{x}} + by\hat{\boldsymbol{y}}, \tag{2.1}$$

where a and b are constants of proportionality. Such a force can be exerted on the ions via the application of an electric field:

$$\vec{E}(x, y) = E_0(\lambda x\hat{\boldsymbol{x}} + \sigma y\hat{\boldsymbol{y}}), \tag{2.2}$$

where E_0, λ and σ are constants governing the strength of the field. Now Gauss' law dictates that:

$$\vec{\nabla} \cdot \vec{E} = 0, \tag{2.3}$$

giving the only non-trivial ($\lambda = \sigma \neq 0$) physically possible solution:

$$\lambda = -\sigma, \tag{2.4}$$

and as such:

$$\vec{E} = E_0\lambda(x\hat{\boldsymbol{x}} - y\hat{\boldsymbol{y}}). \tag{2.5}$$

This electric field has the corresponding potential:

$$\phi = -\frac{1}{2}E_0\lambda(x^2 - y^2). \tag{2.6}$$

This potential can be generated by a set of four hyperbolic electrodes placed

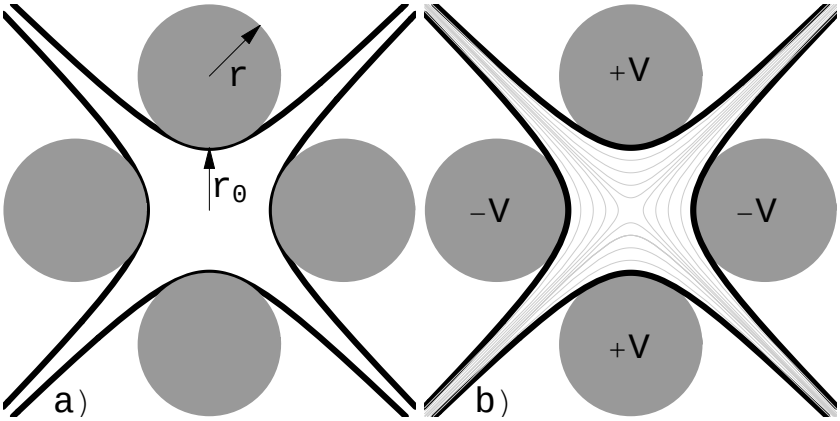

Figure 2.1: a) The ideal hyperbolic structure (black) needed to create the potential given by equation 2.22 can be closely approximated by circular electrodes (gray) where $r = 1.148\, r_0$. b) The equipotential lines generated by such a geometry where $V = \frac{\phi_0}{2}$.

with four-fold symmetry in the xy- plane (see figure 2.1). If a positive bias is applied to one of the opposing pairs of electrodes and a bias equal in magnitude but opposite in polarity is applied to the other pair of opposing electrodes the potential is then:

$$\phi = \frac{\phi_0(x^2 - y^2)}{2r_0^2}, \tag{2.7}$$

where ϕ_0 is the magnitude of the potential difference between adjacent electrodes and r_0 is half the minimum distance between the opposing pairs of electrodes.

Although the potential given by equation 2.7 has the desired effect of focusing linearly in one dimension it also has the undesirable effect of providing a linear defocusing force in the perpendicular direction. However, it has long been known that by placing a series of quadrupolar devices together, such that the focusing direction of each subsequent section is perpendicular to the previous section, a net focusing force can be obtained [Cou58]. Alteratively, a net focusing force can be provided by applying a time dependent potential to the quadrupolar structure thus forming a linear Paul trap.

Consider the quadrupolar structure driven by an ideal square wave, $S_\delta V$, with angular frequency ω, time period T and duty cycle $\delta = 0.5$ where:

$$S_{0.5} = 1 \qquad 0 < t \leq \frac{T}{2}, \tag{2.8}$$

$$S_{0.5} = -1 \qquad \frac{T}{2} \leq t \leq T, \tag{2.9}$$

and V is the amplitude of the square-wave such that:

$$\phi_0 = 2V. \tag{2.10}$$

The time dependant potential inside the trap is thus:

$$\phi(t) = \frac{S_{0.5}V(x^2 - y^2)}{r_0^2}, \tag{2.11}$$

and the corresponding electric field is:

$$E(t) = -\frac{2S_{0.5}V}{r_0^2}(x\hat{\boldsymbol{x}} - y\hat{\boldsymbol{y}}), \tag{2.12}$$

This gives the equations of motion for an ion in the trap as:

$$m\frac{d^2x}{dt^2} = -Ze\frac{2S_{0.5}V}{r_0^2}x, \tag{2.13}$$

$$m\frac{d^2y}{dt^2} = Ze\frac{2S_{0.5}V}{r_0^2}y, \tag{2.14}$$

$$m\frac{d^2z}{dt^2} = 0. \tag{2.15}$$

Where m is the mass of the ion and Ze is its electric charge. In order to understand the nature of the ions motion inside the RFQ cooler and buncher let us now consider the ions motion with respect to just one of the radial axes. If we let:

$$q = \frac{4ZeV}{m\omega^2 r_0^2}, \tag{2.16}$$

$$h = \sqrt{2q}, \tag{2.17}$$

and:

$$\zeta = \frac{\omega t}{2}, \tag{2.18}$$

then the ion motion inside the trap can be described by:

$$\frac{d^2u}{d\zeta^2} + h^2u = 0 \qquad 0 < \zeta \leq \frac{\pi}{2}, \tag{2.19}$$

$$\frac{d^2u}{d\zeta^2} - h^2u = 0 \qquad \frac{\pi}{2} \leq \zeta \leq \pi. \tag{2.20}$$

The definition of the parameter q includes all physical dimensions and fields and it is standard practice to describe the ions motion in a sinusoidally-driven trap in terms of this parameter. Its use in the description of ion motion in a square-wave-driven trap avoids a redefinition of the commonly accepted stability parameter. These equations are known as the Meissner equations after E. Meissner who first used them to study the vibrations of the driving rods in locomotives [Mei18]. They have exact solutions which can most simply be expressed in terms of the transfer matrices:

$$\boldsymbol{M}_+ = \begin{pmatrix} \cos(h\frac{\pi}{2}) & h^{-1}\sin(h\frac{\pi}{2}) \\ -h\sin(h\frac{\pi}{2}) & \cos(h\frac{\pi}{2}) \end{pmatrix}, \tag{2.21}$$

for the period $0 < \zeta \leq \frac{\pi}{2}$ and:

$$\boldsymbol{M_-} = \begin{pmatrix} \cosh(h\frac{\pi}{2}) & h^{-1}\sinh(h\frac{\pi}{2}) \\ h\sinh(h\frac{\pi}{2}) & \cosh(h\frac{\pi}{2}) \end{pmatrix}, \tag{2.22}$$

for the period $\frac{\pi}{2} \leq \zeta \leq \pi$. So over the period $0 < \zeta \leq \pi$ the transfer matrix is:

$$\boldsymbol{M_\pm} = \boldsymbol{M_-} \cdot \boldsymbol{M_+}, \tag{2.23}$$

where:

$$\begin{pmatrix} u \\ v_u \end{pmatrix}_{\zeta=\pi} = \boldsymbol{M_\pm} \cdot \begin{pmatrix} u \\ v_u \end{pmatrix}_{\zeta=0} \tag{2.24}$$

Meissner's equations are specific versions of a more general set of equations known as the Hill equations:

$$\frac{d^2u}{d\zeta^2} + \left(\theta_0 + \sum_{r=1}^{\infty} 2\theta_r \cos(2r\zeta)\right) = 0. \tag{2.25}$$

Where in the case of the Meisnner equation $\theta_r = 0$ for $r > 0$. The properties of Hill equations were studied in the 1800's by G. Floquet and it was found that such equations have both stable and unstable solutions [Flo83]. In this case the stable solutions correspond to a net focusing force and the unstable solutions correspond to a net defocusing force on the ion. The stability criterion:

$$|\boldsymbol{Tr}(\boldsymbol{M_\pm})| < 2, \tag{2.26}$$

can be used to determine if the ions motion is bound or unbound [Pip53]. This gives the condition that for a ideal square wave with 50% duty cycle the value of q must be less than 0.712 if an ions motion is to be stable in the trap. Solutions to the ion's equations of motion for a number of values of q are shown in figure 2.2.

It is a general feature that the stable solutions of a Hill type equation will be of the form:

$$u(t) = \Re\left[A \sum_{n=-\infty}^{\infty} C_n \exp\left[i(n\omega + \omega_s)t\right]\right], \tag{2.27}$$

Where A is a constant depending on the equation's initial conditions. The solution is a Fourier series corresponding to a superposition of an infinite set of frequencies where:

$$\omega_n = |n\omega + \omega_s| \qquad n = 0, \pm1, \pm2..... \tag{2.28}$$

The relative amplitudes, C_n, of which depend on the exact form of the Hill equation, i.e. on the form of the applied potential, but are independent of the equations initial conditions. The slowest oscillation frequency, ω_s, is known as the secular frequency and is also dependant on the form of the applied potential

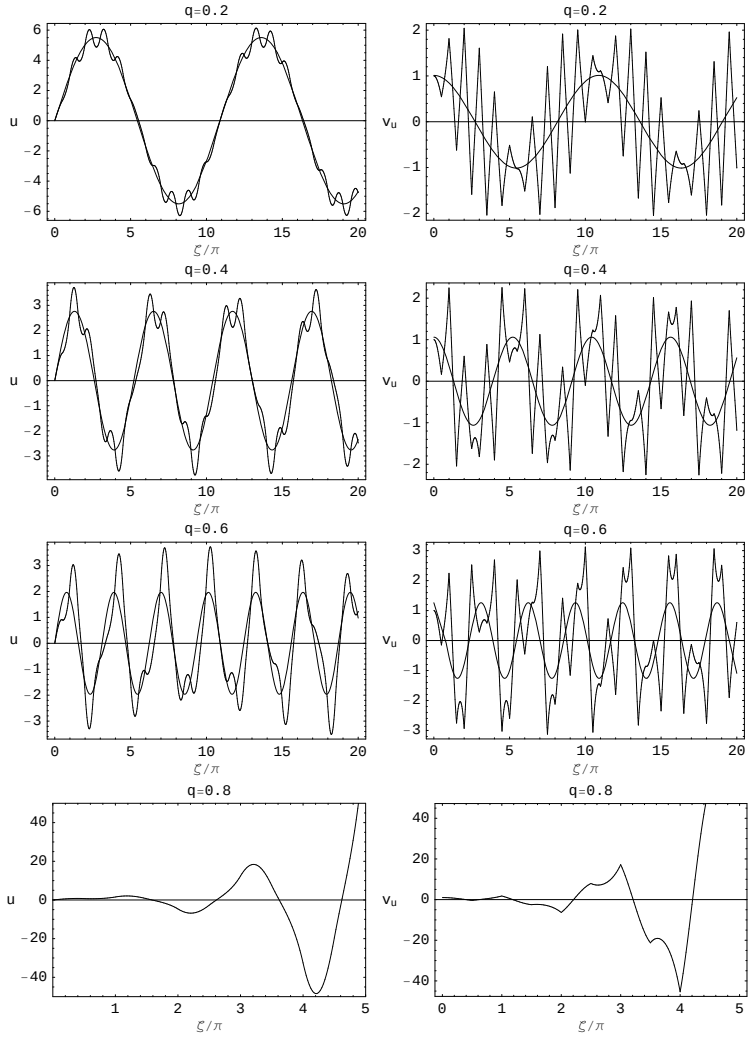

Figure 2.2: Solutions to the Hill equation, with initial conditions $u = 0$ and $v_u = 1$, for given values of q with the pure harmonic macromotion overlayed for comparison. For $q = 0.8$ the motion is unbounded (note the larger scale of the motion) and hence no macromotion solution exists. As the value of q increases so too does the difference between the macromotion and the exact solutions.

and independent of the initial conditions. The value of the secular frequency can be calculated as [Sud02]:

$$\beta = \frac{1}{\pi} \arccos\left(\frac{\boldsymbol{Tr(M_{\pm})}}{2}\right) = \frac{1}{\pi} \arccos[\cos(\pi\sqrt{q/2})\cosh(\pi\sqrt{q/2})] \quad (2.29)$$

$$\omega_s = \frac{\beta\omega}{2}. \quad (2.30)$$

By observation of the solutions to the Meissner equation we see that the motion described to be a slow harmonic motion, known as the macromotion, perturbed by smaller amplitude, higher frequency oscillations, known as the micromotion. If we assume that the ion is moving in a harmonic potential at the secular frequency we can describe the oscillations as:

$$u(\zeta) = A_m \cos(\beta\,\zeta + \alpha), \quad (2.31)$$

where A_m is the amplitude of the secular motion and α describes the phase of the motion both of which can be derived from the ions initial conditions. Figure 2.6 shows a comparison between the purely secular oscillation and actual solutions to the Meissner equation. It can be seen that at lower q values the motion is very close to that of a particle trapped in a simple harmonic potential well. However, as the value of q rises the amplitudes of the higher frequency oscillations increase perturbing the motion from the ideal harmonic case until, at the critical value of $q = 0.712$, the particle motion becomes unbounded.

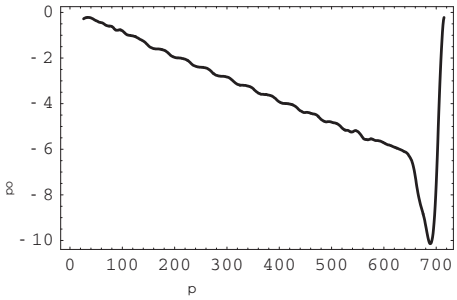

PSfrag replacements
Position (mm)
Potential (V)

Figure 2.3: Longitudinal potential applied to the RFQ rods extracted from a simulation of the device. The ions drift through the gas under the influence of a weak electric field ($\approx 0.1\,V/cm$) before being captured in a deep potential well.

Thus, we see that by using a quadrupolar structure driven by a square-wave it is possible to provide a net centering force on the ions that is close to that created by the ideal harmonic potential. Further, by segmenting the rod structure it is also possible to apply DC offsets so as to create a longitudinal potential. If such a device is filled with a buffer gas it can be used to cool an ion beam. Bunching of the beam can be achieved by applying a longitudinal

potential of the form shown in figure 2.3. The cooled ions will collect in the longitudinal potential minimum and are thus trapped three dimensionally. A cooled bunch of ions can be obtained by raising an electrostatic barrier inside the RFQ, *e.g.* at the longitudinal position $z = 600\,mm$, to stop further incoming ions before they reach the trapping region. The accumulated sample can then be extracted as a bunch by reducing the potential at the end of the RFQ.

2.2 Definition of Temperature in an RFQ

When describing the cooling of ions in an RFQ it is useful to have a definition of the temperature of the ions. This topic has been dealt with in great detail by T. Kim [Kim97] in application to the temperature of ions in a sinusoidally-driven trap. The same ideas are used here to define temperature in the square-wave-driven trap.

Boltzmann defined temperature statistically in terms of the energy distribution of a group of particles:

$$\frac{dN}{dE} = \frac{N_0}{kT}\,\exp\left(-\frac{E}{kT}\right). \tag{2.32}$$

However, as we will see, this definition has to be carefully applied. We take as an example a one dimensional cloud of ions trapped in a harmonic potential. The energy of a given ion in this potential is:

$$E = \frac{p^2}{2m} + \frac{1}{2}m(\omega u)^2, \tag{2.33}$$

where p is the momentum and u is the ion's displacement from the center of the potential. Thus, if the spatial distribution of the ion cloud is known its temperature can be defined. Now imagine that we adiabatically accelerate the potential and the particles up to a velocity, V. The energy of the particles is now:

$$E = \frac{p^2}{2m} + \frac{1}{2}m(\omega u)^2 + \frac{1}{2}mV^2. \tag{2.34}$$

If we include this extra term in the definition of the temperature of the system it would seem that by accelerating the particles we have somehow heated them even though we considered the process of acceleration to be adiabatic. However, we can of course realize that defining temperature in this way is incorrect as we shouldn't consider the coherent motion of the particles as adding to the temperature.

According to Gibbs the temperature of a system of particles can also be defined in terms of the volume, S, that the particles occupy in position momentum phase space:

$$\frac{\partial N}{\partial S} \propto \exp\left(-\frac{E}{kT}\right). \tag{2.35}$$

In a system where the motions in all three directional dimensions are independent this then reduces to:

$$\frac{\partial^2 N(u,p_u)}{\partial p_u \partial u} \propto \exp\left(-\frac{E}{kT}\right), \tag{2.36}$$

and temperature can be defined in terms of the area the cloud occupies in phase space. Going back to our original example of a cloud of ions in a one dimensional harmonic potential we can see more clearly how coherent motions do not add to the temperature of the system. Initially, the cloud occupies a given area in phase space which defines its temperature. Accelerating the ions shifts the position of the cloud in the phase space but it doesn't change its overall area and hence its temperature remains constant.

As we have already seen the motion of ions in an RFQ can be considered as two separate parts, the macromotion and the micromotion. The macromotion of a cloud of ions in the trap is of course the same as that of the cloud of ions described above in the simple harmonic potential. However, the micromotion of the cloud is a coherent motion dependent on the phase of the RF and thus doesn't contribute to the temperature of the ion cloud.

The temperature of a cloud of ions in a harmonic potential can be obtained by substitution of equation 2.33 into 2.36:

$$\frac{\partial^2 N(u,p_u)}{\partial p_u \partial u} \propto exp\left(-\frac{p^2}{2mkT} + \frac{m(\omega u)^2}{2kT}\right), \tag{2.37}$$

integration over all space with respect to position gives:

$$\frac{\partial N(u,p_u)}{\partial p_u} \propto \omega\sqrt{\frac{2\pi kT}{m}}\ \exp\left(-\frac{p^2}{2mkT}\right), \tag{2.38}$$

and integration over all space with respect to momentum gives:

$$\frac{\partial N(u,p_u)}{\partial u} \propto \sqrt{2\pi mkT}\ \exp\left(-\frac{m(\omega u)^2}{2kT}\right). \tag{2.39}$$

Thus the ions have Gaussian distributions in both position and momentum space. The standard deviations of which define the cloud's temperature:

$$\sigma_u = \frac{1}{\omega}\sqrt{\frac{kT}{m}}, \tag{2.40}$$

$$\sigma_{p_u} = \sqrt{mkT}. \tag{2.41}$$

The temperature of a cloud of ions in an ion trap can thus be found by measurement of the standard deviation of either the position or the momentum of the macromotion. Unfortunately, the micromotion acts so as to perturb the cloud such that this doesn't correspond to a measurement of the standard deviation of the position or the momentum of the ion cloud. A cloud of ions

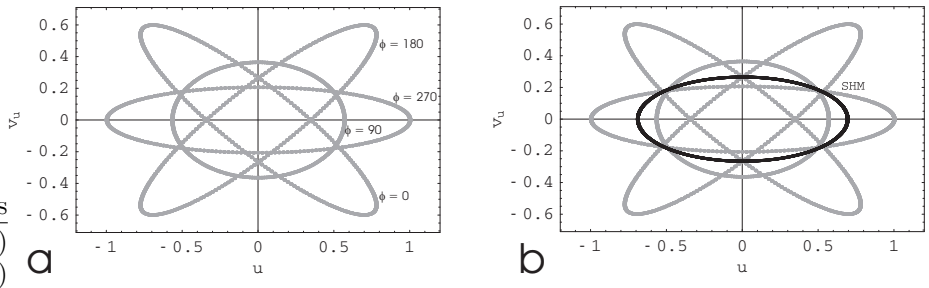

Figure 2.4: a) Distorted harmonic ellipses for different phases of the applied RF-field. A value of 0.4 was taken for q and the ellipses have been scaled such that the maximum positional deviation = 1. b) The ellipse due to pure simple harmonic motion overlayed on the distorted ellipses.

undergoing harmonic macromotion can be represented in position-momentum phase space by an ellipse with the semimajor and semiminor axes fixed as the standard deviations of the position and the momentum of the cloud. The effect of the micromotion is to distort this ellipse whilst conserving it's area (if the area isn't conserved then the claim that the micromotion is coherent is invalid). By solving the equation of motion for an ion with arbitrary initial conditions and observing its path in position-momentum phase space this distortion can easily be seen. Figure 2.4 shows a plot of a particles path through this phase space with a point drawn every time the particle is $0, 90, 180$ and 270 degrees out of phase with the RF as well as the ellipse due to simple harmonic motion. The amplitudes, σ_u and σ_{p_u}, of the corresponding harmonic ellipse are found using:

$$A = \pi \sigma_u \sigma_{p_u}, \tag{2.42}$$

$$\sigma_{p_u} = \sigma_u \omega_s, \tag{2.43}$$

where A is the area of the harmonic ellipse, which is equal to that of any of the perturbed ellipses, and ω_s is the oscillation frequency in the harmonic potential calculated using equation 2.30. The micromotion rotates and stretches/squeezes the harmonic ellipse by an amount that is dependent on the phase of the RF. Using these ellipses the ratio between the maximum displacement of the macromotion and the total motion can be calculated for a given value of q. This information can then be used to relate the actual standard deviations in position and momentum to those due to the macromotion and hence the temperature of an ion cloud can be found. Results of such calculations are shown in figure 2.5.

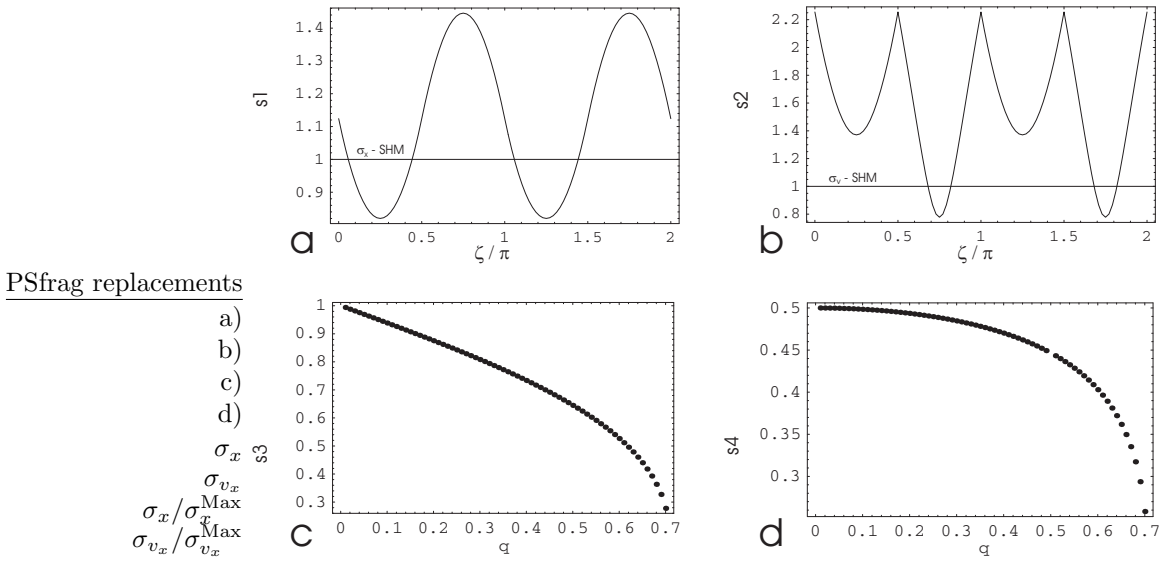

Figure 2.5: Relative difference between the maximal spatial, a), and velocity, b), displacements for the perturbed harmonic motion and the macromotion for $q = 0.4$ as a function of the phase of the RF. c) The ratio of the amplitude of the macromotion to the maximum perturbed amplitude in position space as a function of q. d) The ratio of the amplitude of the macromotion to the maximum perturbed amplitude in momentum space as a function of q.

2.3 Viscous Drag Model for Ion Motion in a Buffer Gas

The simulations detailed in this thesis use a Monte Carlo routine to model the interaction of the ions in an RFQ cooler and buncher with the cooling buffer gas. However, it was initially important to carry out a feasibility study in order to determine some general properties of the device. Numerical simulations based on a simple viscous drag model were found to be better suited for this purpose, before going into the more evolved Monte Carlo simulations.

Consider a cloud of ions with thermal energy sitting in a chamber filled with an inert buffer gas. Left unperturbed the cloud expands as a function of time via the process of diffusion. If a uniform electric field is applied over the length of the chamber the ion cloud will start to move through the gas. The energy gained from the electric field will be countered by energy lost through collisions with the gas. After some time the average energy gained and the average energy lost will reach an equilibrium and the result will be an ion cloud moving through the gas at a fixed average velocity known as the drift velocity, V_d. If the drift velocity is less than the average velocity due to thermal motion of the ions then the diffusion process will remain relatively unaffected by scattering of the ions net forward momentum into the transverse direction. In this regime the electric field strength is proportional to the drift velocity where the constant of proportionality is known as the mobility, k [McD73]:

$$V_d = kE. \tag{2.44}$$

If the drift velocity of the ions is significantly higher than the average thermal velocity of the atoms, then scattering of the ions forward momentum into the radial plane becomes significant. In this regime the ions mobility is no longer constant but is instead dependent on the ratio of the electric field strength to the number density of the gas, E/N. The drift velocities of ions in a gas can be measured experimentally as a function of E/N and hence the mobility can be found.

As the drift velocity of the ions is a constant the acceleration due to the electric field:

$$a_E = \frac{eE}{m}, \tag{2.45}$$

can be thought of as being countered by a deceleration due to the viscous drag caused by the gas:

$$a_d = -\frac{eE}{m} = -\frac{e}{m}\frac{V_d}{k}. \tag{2.46}$$

From the measured values of the drift velocity it is possible to construct a plot of drift velocity versus mobility and a polynomial fit to this data gives an expression for the mobility in terms of the drift velocity. When modelling the motion of an ion through the buffer gas we can assume that its instantaneous velocity is equal to the net drift velocity of an ion cloud and hence we can calculate the drag force on the particle using equation 2.46.

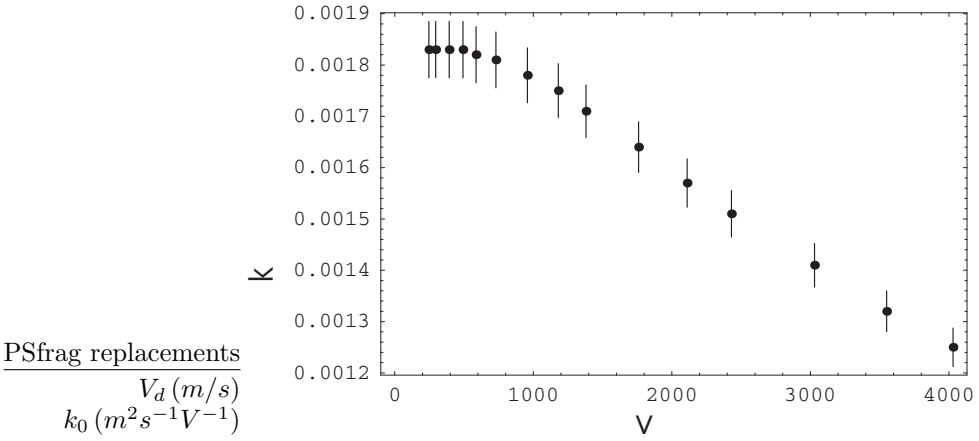

Figure 2.6: Experimental data for the mobility of Cs^+ ions in He [Ell78]. Data exists for drift velocities up to $4030\,m/s$ corresponding to a kinetic energy of around $10\,eV$.

Including the drag force, the equations of motion for particles in a gas filled cooler and buncher become:

$$m\ddot{x} = -Ze\frac{S_\delta V}{r_0^2}x - e\frac{\dot{x}}{k(\dot{x})}, \tag{2.47}$$

$$m\ddot{y} = Ze\frac{S_\delta V}{r_0^2}y - e\frac{\dot{y}}{k(\dot{y})}, \tag{2.48}$$

$$m\ddot{z} = ZeE_z - e\frac{\dot{z}}{k(\dot{z})}, \tag{2.49}$$

where the damping term should only be applied until the ions reach thermal energies. These equations are not exactly solvable but they can be integrated using numerical techniques. Figure 2.6 shows the experimentally determined ion mobility as a function of the drift velocity for cesium ions in a helium buffer gas. The data is given in terms of the reduced mobility, k_0, this is the mobility of the ions at standard temperature, $T_0 = 297\,K$, and pressure, $P_0 = 1\,bar$. This can be related to the mobility at any given temperature and pressure as:

$$k = k_0\,\frac{T}{T_0}\frac{P_0}{P}. \tag{2.50}$$

As is common with such experimental results no data exists for ions with energies greater than around $10\,eV$. RFQ coolers typically accept ions with around 30 to $100\,eV$ energies and as such data outside the experimental range are needed. One way to obtain such data is via the Monte Carlo method outlined in the next chapter and the results for cesium ions in helium are shown in figure 2.7.

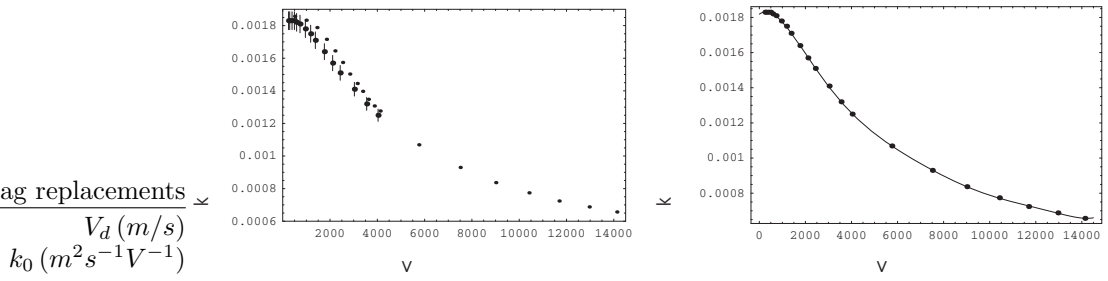

Figure 2.7: a) Comparison of the experimental data for the mobility of Cs^+ ions in he with the values obtained from Monte Carlo simulations. The simulations show some deviations from the experimental results (to be discussed in the following chapter) but reproduce the general trend of the experimental data well. b) A polynomial fit to a combination of the experimental data, at low energies, and the simulated data, at high energies ($V_d > 4030\,m/s$), gives an expression for the mobility of Cs^+ in He in the energy range 0 to $150\,eV$.

A typical calculation of an ions trajectory is shown in figure 2.8. Radially the amplitude of the ion's motion is damped by the buffer gas whilst its oscillation frequency remains the same. If the effect of the longitudinal potential is ignored then the average range, R_z of an ion entering the RFQ with velocity v_{int} in the z- direction can be calculated in the gas as:

$$R_z = \frac{m}{e}\int_0^{v_{int}} k(v_z)dv_z, \tag{2.51}$$

and the average cooling time can also be calculated from:

$$t_{\rm cool} = \frac{m}{e}\int_{v_{\rm therm}}^{v_{\rm int}} \frac{k(v_z)}{v_z}dv_z, \tag{2.52}$$

where $v_{\rm therm}$ is the thermal velocity of the cooled ions. Typical results of these calculations are also shown in figure 2.8. Such calculations reveal little about the final properties of a cloud of ions in the gas as they apply the same average damping force to each ion. This means that eventually all the ions end up with the same final energy which is clearly not representative of a physical system.

From the simple considerations above we see that the range of $30\,eV$ cesium ions in $2.5\times10^{-2}\,mbar$ of helium, a typical gas pressure achieved in other RFQs currently in operation (see for example [Her01] or [Nie01]), is around $500\,mm$ and that it takes around $300\,\mu s$ for the ions to reach thermal temperatures. Although, the cooling time and stopping range will vary with the ions mass consideration of the variance in experimental ionic mobilities tells us that the cesium numbers should be around the right order of magnitude for most ions. In fact most of the proposed measurements with the TITAN system are for ions

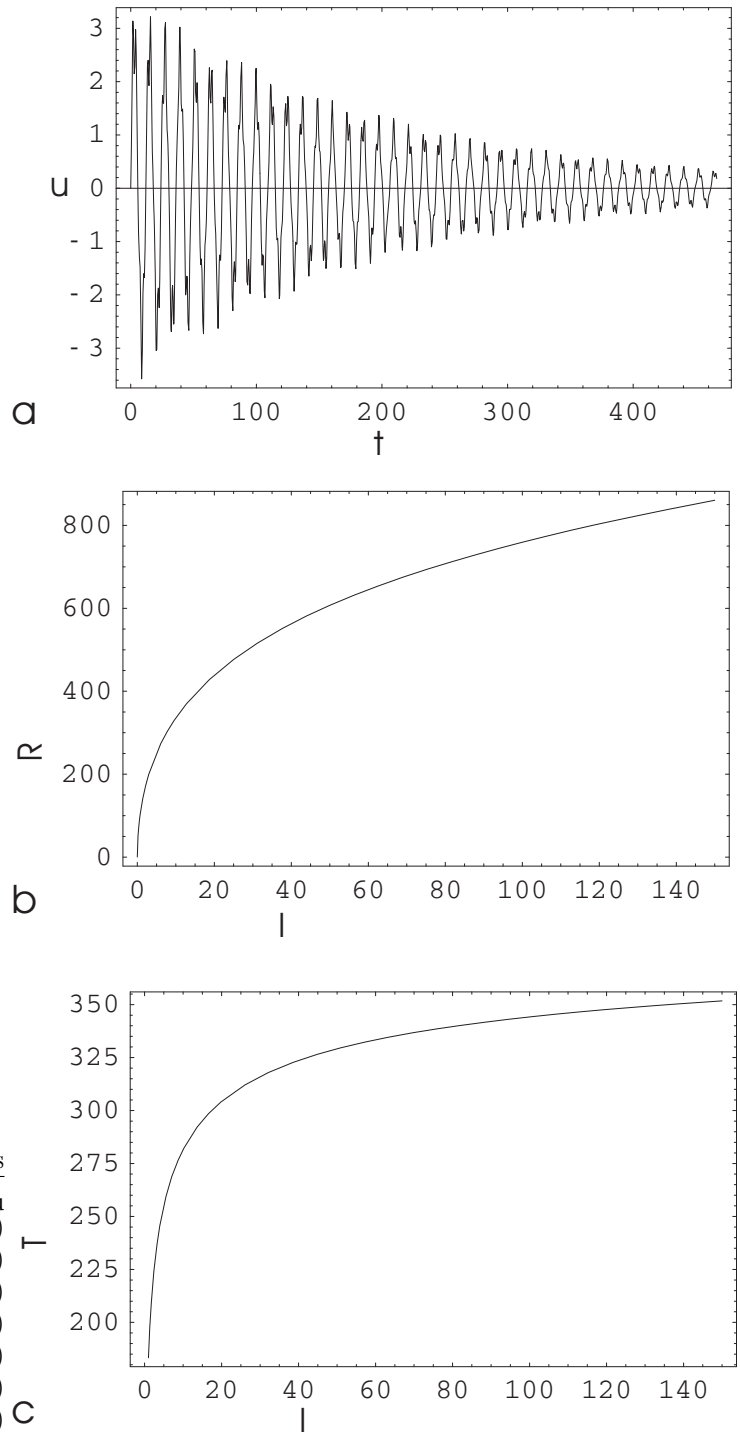

PSfrag replacements

u
Initial Energy (eV)
Time (μs)
Range (mm)
Time (μs)
a)
b)
c)

Figure 2.8: a) An ion's motion becomes damped as a result of its interaction with a buffer gas. b) The calculated range of Cs^+ ions in He at a gas pressure of $2.5 \times 10^{-2}\, mbar$. c) Calculated time for Cs^+ ions in He to cool to thermal energy at a gas pressure of $2.5 \times 10^{-2}\, mbar$.

with masses less than cesium and as such shorter stopping ranges and cooling times can be expected. The TITAN system will be used to make measurements on ions with half-lives in the tens of milliseconds or longer and as such cooling times of around $1\,ms$ are acceptable. The maximum length of the cooler was predetermined by spatial constraints to be $700\,mm$ which fits with the $500\,mm$ stoping range for cesium.

2.4 Acceptance and the Space Charge Limit

When designing the injection optics for the RFQ it is important to know its acceptance. In this section the acceptance of the RFQ is found for the ideal system, i.e. using the ideal equations of motion. With the acceptance known simple estimates of the space charge limit of the trap can be made giving limits on the maximum beam current the trap can accept.

2.4.1 Acceptance of the RFQ

As was shown in section 2.1 the motion of the ions inside an RFQ can be described by a superposition of a simple harmonic macromotion and a higher order micromotion. A particle undergoing harmonic motion traces out an ellipse in position-momentum phase space. The acceptance of the purely harmonic system can be defined by the ellipse corresponding to a motion with maximum amplitude $r_{\max} = r_0$. The effect of the micromotion is to distort this ellipse as a function of phase. The acceptance of the RFQ is defined by the harmonic ellipse whose maximum distorted amplitude $r'_{\max} = r_0$, and is given by:

$$\text{Acceptance} = \omega_s r_{\max}^2 = \frac{\beta\omega}{2} r_{\max}^2, \tag{2.53}$$

where ω is the angular frequency of the applied RF and β can be found using equation 2.29. The amplitude $r_{\max}$ of the harmonic ellipse can be found using the methods outlined in section 2.2. By rearranging equation 2.16 we can obtain an expression for ω as:

$$\omega = \sqrt{\frac{4ZeV}{mqr_0^2}}, \tag{2.54}$$

hence:

$$\text{Acceptance} = \beta\sqrt{\frac{ZeV}{mqr_0^2}}\, r_{\max}^2. \tag{2.55}$$

The acceptance of TITAN's RFQ is shown in figure 2.9 as a function of q. The results assume an applied peak-to-peak voltage of $400\,V$ and a value for $r_0 = 10\,mm$. As shown in equation 2.55 increasing the value of the applied voltage by a factor of two increases the acceptance by a factor of root two. The maximum acceptance was found to occur at $q \approx 0.32$.

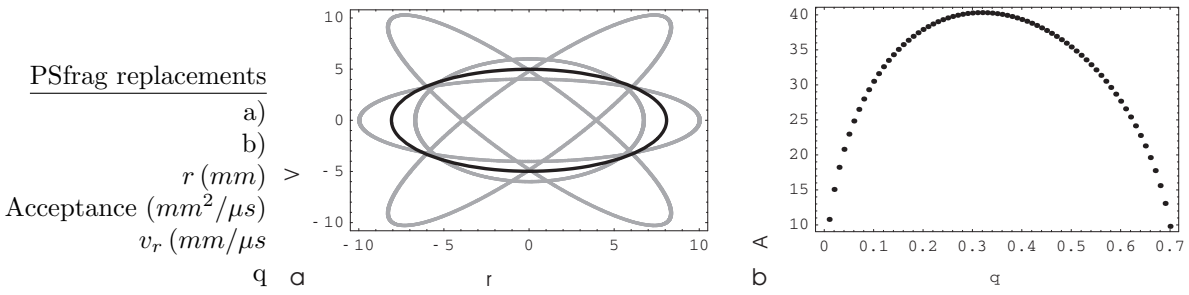

Figure 2.9: a) Distorted harmonic ellipses (gray) and the corresponding purely harmonic ellipse (black) for an ion in TITAN's RFQ operating with $q = 0.3$. The ellipses are scaled such that maximum deviation of the ion from the center of the trap $r'_{\max} = r_0$. b) The acceptance of the trap as a function of q.

2.4.2 Space Charge Limit in Continuous Mode

An estimate to the maximum beam current that can be accepted by the system when operating in continuous mode can be obtained using data from the acceptance ellipses. In this mode the ions are not trapped longitudinally but instead allowed to pass straight through the trap resulting in a cooled continuous beam. If we consider the motion of the ions to be purely harmonic then we can obtain the depth of the harmonic pseudo-potential as:

$$V_{\text{mac}} = \frac{1}{2}\frac{m}{Ze}(\omega_s r_{\max})^2, \tag{2.56}$$

with corresponding electric field:

$$E_{\text{mac}} = -\frac{m}{Ze}\omega_s^2 r_{\max}, \tag{2.57}$$

where $r_{\max}$ is the maximum radial amplitude of the harmonic ellipse and ω_s is the frequency of the harmonic oscillation. If we assume that the ions in the trap form a solid beam of radius r and uniform linear charge density $\lambda(x)$ then the electric field at the edge of the beam is given by:

$$E_{sc} = \frac{\lambda(x)}{2\pi\epsilon_0 r}. \tag{2.58}$$

The beam is slowed by the gas until it reaches its drift velocity. The charge density at this point is then:

$$\lambda = \frac{I}{V_d}, \tag{2.59}$$

where I is the beam current at the entrance to the RFQ. We take this as the charge density in equation 2.59 as this represents an upper limit on the charge

density inside the RFQ. At the space charge limit the electric field due to the ions themselves is exactly balanced by the trapping field. This gives an expression for the maximum allowable current impinging on the trap as:

$$I_{\max} = 2\pi\epsilon_0 \frac{m}{Ze}\,\omega_s^2 r_{\max}^2 V_d = 2\pi\epsilon_0\,\frac{V}{q}\left(\frac{\beta\, r_{\max}}{r_0}\right)^2 V_d. \tag{2.60}$$

We take as an example a typical drift velocity $V_d = 1000\,m/s$ corresponding approximately to an longitudinal electric field of $0.1\,V/cm^{-1}$ at a gas pressure of $2.5\times\ 10^{-2}\,mbar$. The calculated maximum currents as a function of q are shown in figure 2.10. The maximum current allowed was found to occur around

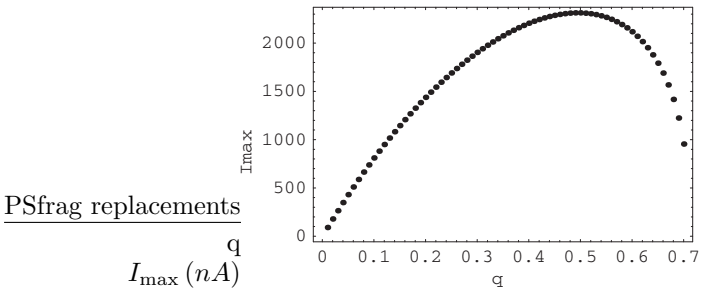

Figure 2.10: The maximum acceptable beam current for the RFQ as a function of q value with the system operated in continuous mode.

$q = 0.49$. The current is of the order of $2.3\,\mu A$ for the TITAN RFQ with $r_0 = 10\,mm$ and an applied peak-to-peak voltage of $400\,V$. Isotopically pure beams are produced at the ISAC facility with currents typically in the nanoampere range which will not overload the system at any q value. However, this will also allow one to test the system for other applications with higher currents, e.g. as a mass separator for the unfiltered ISAC beam.

2.4.3 Space Charge Limit in Bunched Mode

From the viscous drag model we can get an estimate of the cooling time for ions in the trap. With the cooling time known an estimate for the maximum acceptable beam current in bunched mode can be made.

At the end of the RFQ the ions are trapped radially in the potential given by equation 2.56. As we will see in section 3.2.2 the longitudinal potential is set such that it has approximately the same depth as the effective radial potential. This means that we can consider the ions to be in a spherically symmetric potential well. We take the ion bunch to be a solid sphere with radius R and charge Q uniformly distributed throughout its volume. The corresponding electric field is given by:

$$E_{\rm sc} = \frac{Q}{4\pi\epsilon_0 R^2}. \tag{2.61}$$

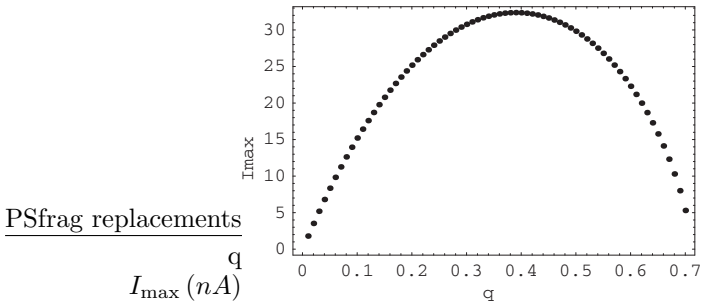

Figure 2.11: The maximum acceptable beam current for the RFQ as a function of q value with the system operated in bunched mode.

This gives the maximum amount of charge it is possible to store in the trap as:

$$Q_{\max} = 4\pi\epsilon_0 \frac{m}{Ze}\omega_s^2 r_{\max}^3 = 4\pi\epsilon_0 \frac{V}{q}\left(\frac{\beta}{r_0}\right)^2 r_{\max}^3. \tag{2.62}$$

Taking an upper estimate for the cooling time of $1000\,\mu s$ we can then calculate the maximum acceptable current as a function of q. The results are shown in figure 2.11.

In bunched mode the system operates in a regime much closer to the space charge limit. The maximum current allowed was found to occur for a q value of 0.39, corresponding to a maximum current of $32\,nA$ and a space charge limit of $Q = 3.2\,pC$.

Chapter 3

TITAN's RFQ Cooler and Buncher

In this chapter the simulations of the RFQ cooler and buncher are presented. In the first section an overview of the simulation methods used is given. This includes a detailed description of the Monte Carlo algorithm used to simulate the ions interaction with the buffer gas. The second section describes simulations of the cooler itself including results from the simulation of the cooling of cesium ions in helium. Details of the required ion optics needed to inject/extract an ion beam into/out of the system are given including the simulated properties of the extracted beam. In the final section of this chapter the RFQ design is presented along with some details of the construction and testing of the device.

3.1 Simulation Methods and the Monte Carlo Algorithm

The ion optics package SIMION [Dah00] was used in order to simulate all the ion optics, both electrostatic and electrodynamic elements, for the RFQ. The program uses the over-relaxation method to find the electric potential generated by any user defined electrode geometry. Numerical calculations of the trajectories of ions through the electric potential can then be carried out. The results of the simulations can be analyzed visually using the programs Graphical User Interface or output to a file for further analysis. The program also allows ion trajectories to be modified by user defined programs. Simulation of electrodynamic fields is achieved by allowing a user program to change the potential on any given electrode as a function of time. Buffer-gas cooling can also be simulated either by the addition of a drag force or by using a Monte Carlo routine.

Monte Carlo simulations of the cooling of ions in a buffer gas have previously been carried out by T. Kim [Kim97] and by S. Schwarz [Sch98]. The code developed here is based on the same principles as their work although it deals with the calculation of collision probabilities in a more thorough manner. Unless otherwise stated any theory used in this section can be found in [McD73].

The code uses known ion-atom interaction potentials to calculate the scattering angle between an ion-atom pair in the center of mass frame. These in turn can be related to the energy lost/gained by the particles in a collision in the

lab frame. Theoretically calculated ion-atom interaction potentials are available for a number of different pairs of species. However, the accuracy of these potentials does vary. The simulations in this work detail the cooling of cesium ions in a helium buffer gas. However, the ion-atom interaction potential for this pair is known with relatively poor accuracy. Different experimental methods for measuring the potential have produced conflicting results and currently ab-initio calculations of the ion-atom interaction potential are impossible due to the large numbers of electrons involved. For this reason the code was tested by simulating the interaction of lithium ions in helium. For this ion-atom pair an ab-initio calculation of the interaction potential is possible. This potential has been previously used to calculate the theoretical mobility of lithium in helium and produces results that are in agreement with experimental data [Elf99]. The interaction potential for cesium in helium was taken to be [McD73]:

$$V_{\mathrm{Cs}^+}(r) = 0.0109\left(\frac{0.000346}{r^8} - \frac{0.00242}{r^6} - \frac{0.0222}{r^4}\right) \tag{3.1}$$

and the interaction potential for lithium in helium was taken as:

$$V_{\mathrm{Li}^+}(r) = 27.2\left(23.2\ e^{-43.8r} + \frac{8.74\times10^{-9}e^{-32.9r}}{r^6} - \frac{5.98\times10^{-6}e^{-0.116r}}{r^4} + \frac{0.0529(23.0\ e^{-62.5r} - 6.44\ e^{-32.0r})}{r} - 29.3\ e^{-59.5r}\right), \tag{3.2}$$

which was obtained from a fit to the calculated values from [Elf99]. In both cases the potential will be given in electron volts if the radius is in nanometers.

Classical considerations of the elastic scattering of two bodies interacting via a central potential, $V(r)$, in the center of mass (cm) frame leads to the result:

$$\theta_{\mathrm{cm}}(b, E_{\mathrm{cm}}) = \pi - 2b\int_{r_m}^{\infty}\left(1 - \frac{b^2}{r^2} - \frac{V(r)}{E_{\mathrm{cm}}}\right)^{-\frac{1}{2}}\frac{dr}{r^2}, \tag{3.3}$$

where E_{cm} is the total kinetic energy of the collision in the center of mass frame, θ_{cm} is the scattering angle in the center of mass frame, b is the impact parameter of the collision, and r_m is the distance of closest approach of the two bodies. Where r_m is the largest of the real roots of the equation:

$$1 - \frac{b^2}{r_m^2} - \frac{V(r_m)}{E_{\mathrm{cm}}} = 0. \tag{3.4}$$

For the interaction potentials given in equations 3.1 and 3.2 equation 3.3 can be integrated numerically. Hence, for a given center of mass energy and impact parameter the scattering angle in the center of mass frame, θ_{cm}, can be calculated. A plot of the scattering angle versus the impact parameter for lithium in helium at a center of mass energy of $0.06\,eV$ is shown in figure 3.2 alongside a plot of the interaction potential. The strength of the interaction potential falls off sharply as a function of the separation of the ion and the atom and as such

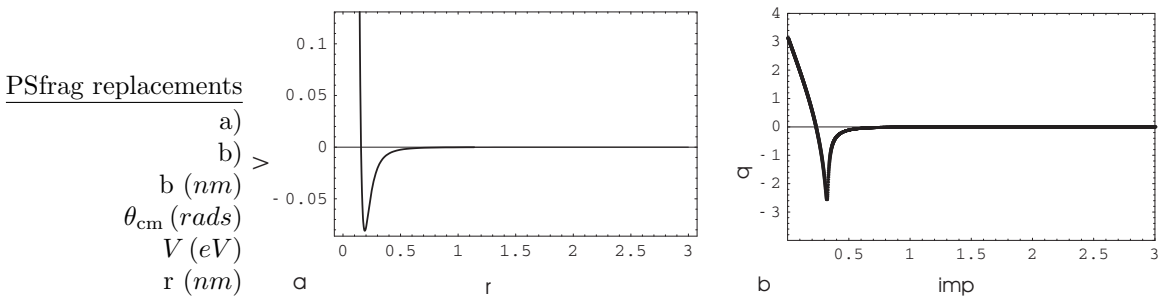

Figure 3.1: a) The Ion-Atom interaction potential for lithium ions in helium, b) The center of mass scattering angle for lithium in helium as a function of impact parameter for a center of mass energy of $0.06\,eV$.

so does the scattering angle. By defining a maximum impact parameter below which the effect of the ion-atom interaction potential can be neglected, b_{max}, the scattering cross section can be defined as:

$$\sigma = \pi b_{\max}^2. \tag{3.5}$$

This maximum impact parameter can then be considered to correspond to a minimum scattering angle, $\theta_{\min}$, where $b_{\max}$ is the largest impact parameter at which the minimum scattering angle occurs. The scattering angle in the center of mass frame can be used to relate the ions kinetic energy before the collision in the laboratory frame, $E_{\rm lab}$, to the ion's kinetic energy after the collision, $E^s_{\rm lab}$, by:

$$\frac{E^s_{\rm lab}}{E_{\rm lab}} = \left(\frac{m_i^2 + m_g^2}{(m_i + m_g)^2} + \frac{2 m_i m_g}{(m_i + m_g)^2} \cos(\theta_{\rm cm}) \right), \tag{3.6}$$

where m_i is the mass of the ion and m_g is the mass of the gas atom. For $\theta_{\rm cm} = 1\,mrad$ this ratio is very close to one for both lithium and cesium scattering on hydrogen. Thus, $1\,mrad$ is a suitable value for $\theta_{\min}$. As shown in figure 3.2 an expression for the cross section as a function of center of mass energy, $\sigma(E_{\rm cm})$, can be found from a fit to calculated values of $b_{\max}$ at various energy values.

3.1.1 The Monte Carlo Algorithm

The Monte Carlo algorithm can be broken up into three major parts:

- Determine if a collision occurs.

If a collision does occur then:

- Select the properties of the collision partner.
- Calculate the ion's new velocity after the collision.

we now look at each section in detail.

PSfrag replacements
a)
b)
$E_{\rm cm}\,(eV)$
$b_{\rm max}\,(nm)$
$b_{\rm max}(E_{\rm cm}) = \frac{0.868}{E_{\rm cm}^{0.222}} - 0.089$
$b_{\rm max}(E_{\rm cm}) = \frac{0.899}{E_{\rm cm}^{0.243}} - 0.011$
$\sigma_{E_{\rm cm}} = \pi b_{\rm max}$

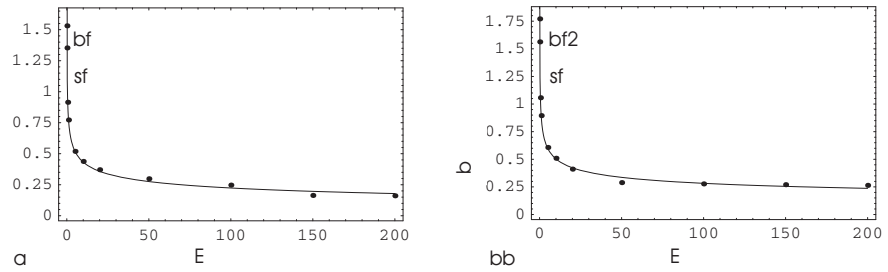

Figure 3.2: A fit to calculated values of $b_{\rm max}$ at given center of mass energies gives an expression for the cross section as a function of center of mass energy for a) lithium ions scattering on atomic hydrogen and b) cesium ions scattering on atomic hydrogen.

Determine if a Collision Occurs

The first step in the Monte Carlo code is to determine if a collision has taken place. The probability of a collision occurring in time Δt is related to the collision rate, R, by:

$$P(\Delta t) = 1 - \exp\left(R\Delta t\right) \approx R\Delta t, \tag{3.7}$$

the approximation holds if the value of $R\Delta t$ is small that is if the probability of collision itself is small ($\ll 1$). This also means that the probability of the ion colliding with two or more atoms at the same time is so small that such processes can be neglected. The kinetic theory of gases gives the collision rate for an ion moving through a gas with velocity $\vec{v}_i$ as [Wan66]:

$$R(v_i) = n \int |\vec{v}_i - \vec{v}_g|\, \sigma(|\vec{v}_i - \vec{v}_g|)\, f(\vec{v}_g)\, d\vec{v}_g, \tag{3.8}$$

where n is the number density of the gas atoms and $f(\vec{v_g})$ is the Maxwell-Boltzmann velocity distribution of the gaseous atoms:

$$f(\vec{v}_g) = \left(\frac{m_g}{2\pi kT}\right)^{\frac{3}{2}} \exp\left(-\frac{m_g \vec{v}_g^{\,2}}{2kT}\right). \tag{3.9}$$

Using the obtained expression for the cross section numerical integration methods can be used to find the collision rate as part of the Monte Carlo code. However, this adds considerably to the run time and so it is desirable to find a way to avoid integrating inside the code. One method to overcome this is to calculate the collision rate at different values of ion velocity and use a polynomial fit to find an expression for the collision rate. Alternatively an extension to the method outlined by Robertson and Sternovsky [Rob03] can be used. Equation 3.8 can be rewritten in terms of the relative velocity, $\vec{v}_{\rm rel}$, between the ion and

the atom where:

$$\vec{v}_{\rm rel} = \vec{v}_i - \vec{v}_g, \tag{3.10}$$

$$E_{\rm cm} = \frac{1}{2}\mu v_{\rm rel}^2. \tag{3.11}$$

Where μ is the reduced mass of the ion-atom pair. Hence:

$$R(v_i) = n \int |\vec{v}_{\rm rel}|\ \sigma(\vec{v}_{\rm rel})\ f(\vec{v}_g)\ d\vec{v}_g. \tag{3.12}$$

If the relative velocity between the ion and the atom is assumed constant then this reduces to the well know expression:

$$R(v_i) = n\, v_i\, \sigma(v_i), \tag{3.13}$$

if a mean relative velocity $\bar{w}$ can be found then the collision rate is given by:

$$R(\bar{w}) = n\, \bar{w}\, \sigma(\bar{w}), \tag{3.14}$$

in analogy to equation 3.13. The mean relative velocity can be given as [Rob03]:

$$\bar{w}(v_i) \cong \left[\left(\frac{4v_{\rm th}^2}{\pi} \right)^{2.14} + v_i^{2.14} \right]^{\frac{1}{2.14}}, \tag{3.15}$$

where:

$$v_{\rm th} = \sqrt{\left(\frac{2kT}{m_g} \right)}, \tag{3.16}$$

is the most probable thermal speed of the gas atoms.

Once the collision probability has been calculated a decision as to whether or not a collision occurs in time Δt is made by comparison of $P(\Delta t)$ with a random number, ran_1 (the notation ran_n will be used to denote a uniformly generated random number in the range $0 \leq ran_n \leq 1$ throughout the text). If $ran_1 \leq P(\Delta t)$ then a collision is said to have occurred. If a collision is taken not to have occurred the ion is allowed to propagate through the applied electric field for time Δt. If a collision is taken to have occurred then a random value for the time at which it occurs, δt with $0 \leq \delta t \leq \Delta t$, is selected. The probability of the collision occurring increases linearly as a function of time:

$$\frac{dP(\delta t)}{d\,\delta t} \propto t, \tag{3.17}$$

this distribution can be generated using the analytical inversion method [Law00] where:

$$\delta t = \sqrt{ran_2}\ \Delta t. \tag{3.18}$$

The ion is then propagated through the applied electric field for time δt before the effect of the scattering process is taken into account.

Select the Properties of the Collision Partner

In order to simulate the scattering process first the velocity of the gas atom has to be selected. Equation 3.8 gives the total collision rate for an ion with velocity $\vec{v}_i$ moving through an atomic gas with a Maxwell-Boltzmann velocity distribution $f(\vec{v}_g)$. The term inside the integral is thus the collision rate $r(\vec{v}_i, \vec{v}_g)$ between the ion and an atom moving at velocity $\vec{v}_g$ which is proportional to the probability of the collision occurring. The ion sees the gas as having a shifted Maxwell-Boltzmann distribution $g(\vec{v}_i, \vec{v}_g)$, where:

$$g(\vec{v}_i, \vec{v}_g) = |\vec{v}_i - \vec{v}_g|\ \sigma(|\vec{v}_i - \vec{v}_g|)\ f(\vec{v}_g). \tag{3.19}$$

The velocity of the atom must be selected from this distribution. This can be done via the rejection-acceptance method [Law00]. Random values for the three cartesian components of the velocity of the gas are first chosen from a uniform distribution between $\pm 3v_{\mathrm{th}}$ corresponding to three standard deviations of the normally distributed gas velocity in the laboratory frame:

$$v_g^x = (2\,ran_3 - 1)3v_{\mathrm{th}}, \tag{3.20}$$
$$v_g^y = (2\,ran_4 - 1)3v_{\mathrm{th}}, \tag{3.21}$$
$$v_g^z = (2\,ran_5 - 1)3v_{\mathrm{th}}. \tag{3.22}$$

As the ion velocity is known a value for $g(\vec{v}_i, \vec{v}_g)$ can be calculated. This value is then compared to a uniformly generated random number between 0 and $g_{\max}$:

$$RAN = ran_6\, g_{\max}, \tag{3.23}$$

where $g_{\max}$ is the maximum value of the distribution $g(\vec{v}_i, \vec{v}_g)$. If $g(\vec{v}_i, \vec{v}_g) \geq RAN$ then the values for the velocities are accepted. If not, they are rejected and three new random velocities are generated. The procedure loops until a set of velocities are generated that are accepted. With these values the center of mass velocity is then calculated:

$$\vec{v}_{\mathrm{cm}} = \left(\frac{v_g^x m_g + v_i^x m_i}{m_i + m_g}, \frac{v_g^y m_g + v_i^y m_i}{m_i + m_g}, \frac{v_g^z m_g + v_i^z m_i}{m_i + m_g} \right). \tag{3.24}$$

The velocities of the ion and the atom in the center of mass frame are thus:

$$\vec{v}_{i_{\mathrm{cm}}} = \vec{v}_i - \vec{v}_{\mathrm{cm}}, \tag{3.25}$$
$$\vec{v}_{g_{\mathrm{cm}}} = \vec{v}_g - \vec{v}_{\mathrm{cm}}, \tag{3.26}$$

with the center of mass energy given by:

$$E_{\mathrm{cm}} = \frac{1}{2} m_i {v_{i_{\mathrm{cm}}}}^2 + \frac{1}{2} m_g {v_{g_{\mathrm{cm}}}}^2. \tag{3.27}$$

With the center of mass energy known the scattering cross section can be calculated and from it the maximum value of the impact parameter. The probability

of the collision occurring with a given impact parameter increases linearly with the value of the impact parameter:

$$\frac{dP(b)}{db} \propto b. \tag{3.28}$$

Using the analytical inversion method a value for the impact parameter can be obtained from:

$$b = \sqrt{ran_7}\, b_{\max}. \tag{3.29}$$

With values for the impact parameter and center of mass energy the center of mass scattering angle can be calculated using equations 3.3 and 3.4.

Calculate the Ion's New Velocity After the Collision

The collision kinematics are done via rotations in the center of mass frame using the rotation matrices:

$$\boldsymbol{R_n} = \begin{pmatrix} \cos(\theta_n)\cos(\varphi_n) & \cos(\theta_n)\sin(\varphi_n) & -\sin(\theta_n) \\ -\sin(\varphi_n) & \cos(\varphi_n) & 0 \\ \sin(\theta_n)\cos(\varphi_n) & \sin(\theta_n)\sin(\varphi_n) & \cos(\theta_n) \end{pmatrix}, \tag{3.30}$$

$$\boldsymbol{U_n} = \begin{pmatrix} \cos(\theta_n)\cos(\varphi_n) & -\sin(\varphi_n) & \sin(\theta_n)\cos(\varphi_n) \\ \cos(\theta_n)\sin(\varphi_n) & \cos(\varphi_n) & \sin(\theta_n)\sin(\varphi_n) \\ -\sin(\theta_n) & 0 & \cos(\theta_n) \end{pmatrix}. \tag{3.31}$$

$\boldsymbol{R_n}$ corresponds first to a clockwise rotation about the z- axis through angle φ_n followed by a clockwise rotation about the y- axis through angle θ_n and $\boldsymbol{U_n}$ is its inverse. First the ion's center of mass velocity is rotated into a frame where its velocity points purely along the positive z- axis:

$$\boldsymbol{v}'_i = \boldsymbol{R_1} \cdot \boldsymbol{v}_{i_{\mathrm{cm}}} = (0, 0, v_{i_{\mathrm{cm}}}), \tag{3.32}$$

$$\theta_1 = \arctan\left(\frac{v^y_{i_{\mathrm{cm}}}}{v^x_{i_{\mathrm{cm}}}}\right), \tag{3.33}$$

$$\varphi_1 = \arccos\left(\frac{v^z_{i_{\mathrm{cm}}}}{v_{i_{\mathrm{cm}}}}\right). \tag{3.34}$$

In this frame the scattering process can be described by a rotation of the ions velocity about the y- axis by the scattering angle followed by a rotation by a random angle about the z- axis (see figure 3.3):

$$\boldsymbol{v}''_i = \boldsymbol{U_2} \cdot \boldsymbol{v}'_i \tag{3.35}$$

$$\theta_2 = \theta_{\mathrm{cm}}, \tag{3.36}$$

$$\varphi_2 = 2\pi\, ran_8. \tag{3.37}$$

Rotation back to the original center of mass frame gives the new velocity of the ion as:

$$\boldsymbol{v}^s_{i_{\mathrm{cm}}} = \boldsymbol{U_1} \cdot \boldsymbol{v}''_i. \tag{3.38}$$

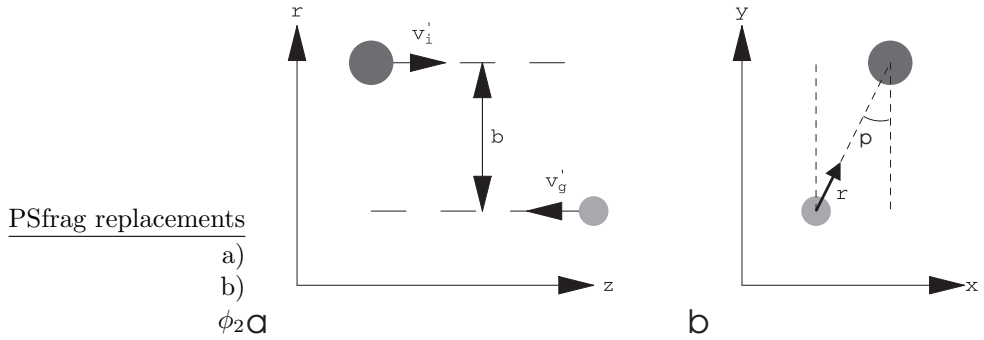

Figure 3.3: a) An ion and an atom move toward each other in a center of mass frame rotated such that their velocities are aligned with the z- axis. The pair are separated by impact parameter, b, in the r-z plane. b) The orientation of r in the x-y plane. The angle between the ion and the atom, φ_2, can take any value from 0 to 2π with every value equally probable.

In the center of mass frame the ions and the atom have equal but opposite momenta. This means that in this frame an elastic scattering process is described purely by a rotation with neither particle losing or gaining energy. Shifting the scattered center of mass velocity of the ion back into the original laboratory frame results in the ions energy changing by the amount given by equation 3.6. Therefore the velocity of the ion in the lab frame after the collision is simply:

$$\vec{v}_i^s = \vec{v}_{i_{\rm cm}}^s + \vec{v}_{\rm cm}. \tag{3.39}$$

A flow chart for the Monte Carlo algorithm is shown in figures 3.4 and 3.5. Two versions of the code were written the first in C and the second in the SIMION SL programming language. The version in C runs approximately ten times faster than the version in SL. However, the C code doesn't run simultaneously with the SIMION program. Instead, the effects of electric fields can either be included via analytic solutions or from electrostatic potentials extracted from SIMION.

The algorithm was tested via the simulation of the motion of lithium and cesium ions in helium under the application of a uniform electric field. The ions mobility was extracted from the simulations at different values of the ratio of the electric field to the number density of the gas, E/N. A comparison between the simulated results and the experimental data is shown in figure 3.6. Two main assumptions are made in the simulation, first that the scattering can be described by only considering elastic processes and second that the ion-atom interaction potential used accurately describes these processes. In the energy range considered ($\approx 0\,\text{to}\,8\,eV$ for lithium and $\approx 0\,\text{to}\,10\,eV$ for cesium) both of these assumptions seem to hold true for lithium as the simulations appear to be in good agreement with the experimental data. For cesium there are some departures between the simulated and experimental data. However, this

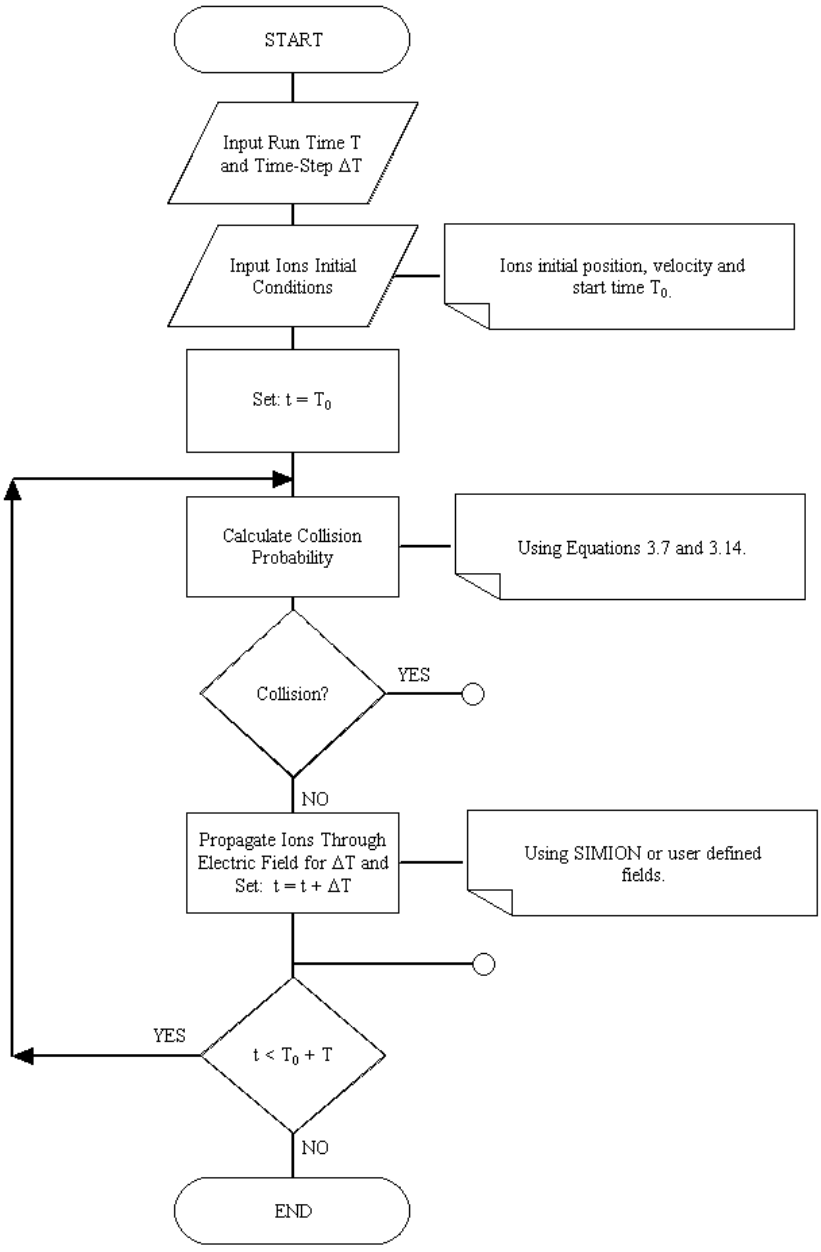

Figure 3.4: Flow chart for the Monte Carlo algorithm (continued in figure 3.5).

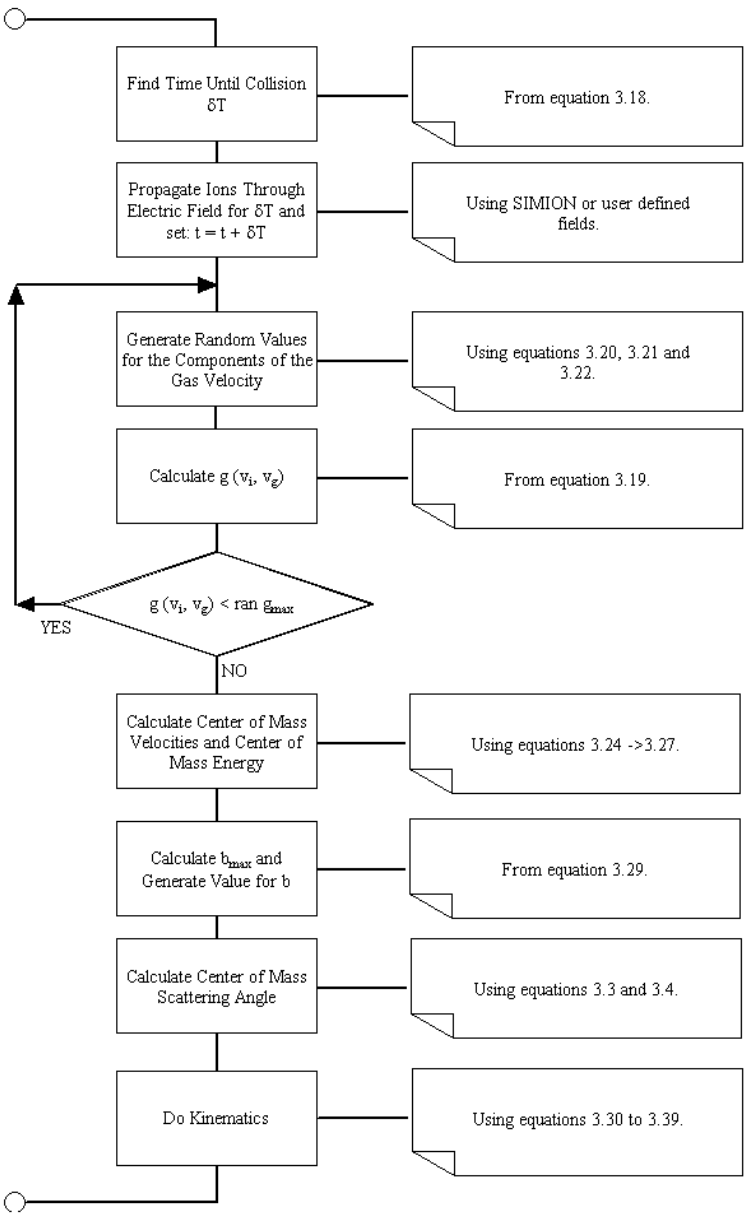

Figure 3.5: Flow chart for the Monte Carlo algorithm (continued from figure 3.4).

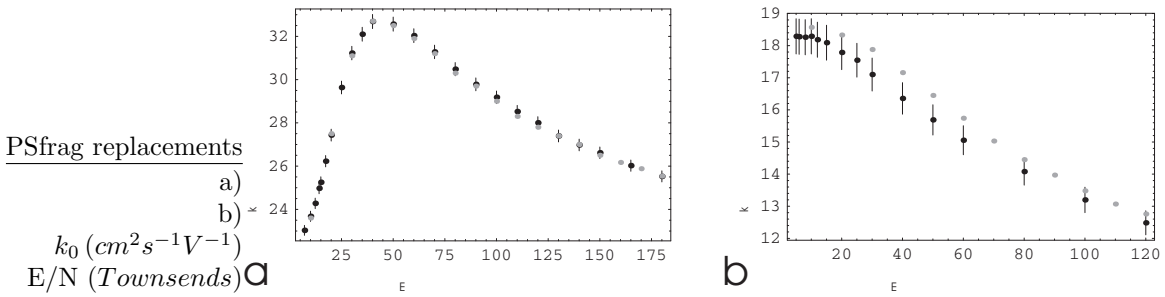

Figure 3.6: Comparison between experimental results (in black) with simulated results (in gray) for the mobility of a) lithium in helium b) cesium in helium. The ratio E/N is given in units of $Townsends = 1 \times 10^{-17}\,Vcm^2$.

shouldn't be surprising as the exact form of the interaction potential is not known due to the complex structure of the atom. In the preceding chapter simulated values for the mobility of cesium in helium were shown up to higher energies ($E \lesssim 150\,eV$). In these energy regimes inelastic processes will certainly occur, however it is known that these effects only moderately influence the ions mobility.

3.2 Simulation of TITAN's RFQ

3.2.1 Deceleration and Injection

Before injection into the RFQ the ISAC beam must be first electrostatically decelerated down to an energy in the range of $30\,\text{to}\,150\,eV$. Two barriers are used to keep the buffer gas in the RFQ box, these barriers have small, $5\,mm$ diameter, holes in them for the injection of the ion beam. The hole is kept small so as to reduce the amount of gas leaking from the system. This means that the beam must also be brought to a focus as it enters the RFQ box. The ISAC beam has typical 99% transverse emittances of $50\,\pi\,mm\,mrad$ at $40\,keV$ and a typical longitudinal energy spread on the order of a $5\,eV$. The transport optics for the ISAC beam to the TITAN experiment had not been finalized when the injection optics for the RFQ were designed. Hence, the exact form of the beam entering into the RFQ was not known. The simplest way to focus a decelerating beam is to use an aperture lens (see figure 3.7). The lens is formed by placing an electrode with a circular aperture between a region of low electric potential and a region of high electric potential. If the electric field on one side of the electrode is stronger than the electric field on the other side of the electrode then the field obtains a radial component in the vicinity of the aperture. This radial component acts so as to focus an ion beam if the beam moves from a high to a low field region and to defocus the beam if it moves from a low to a

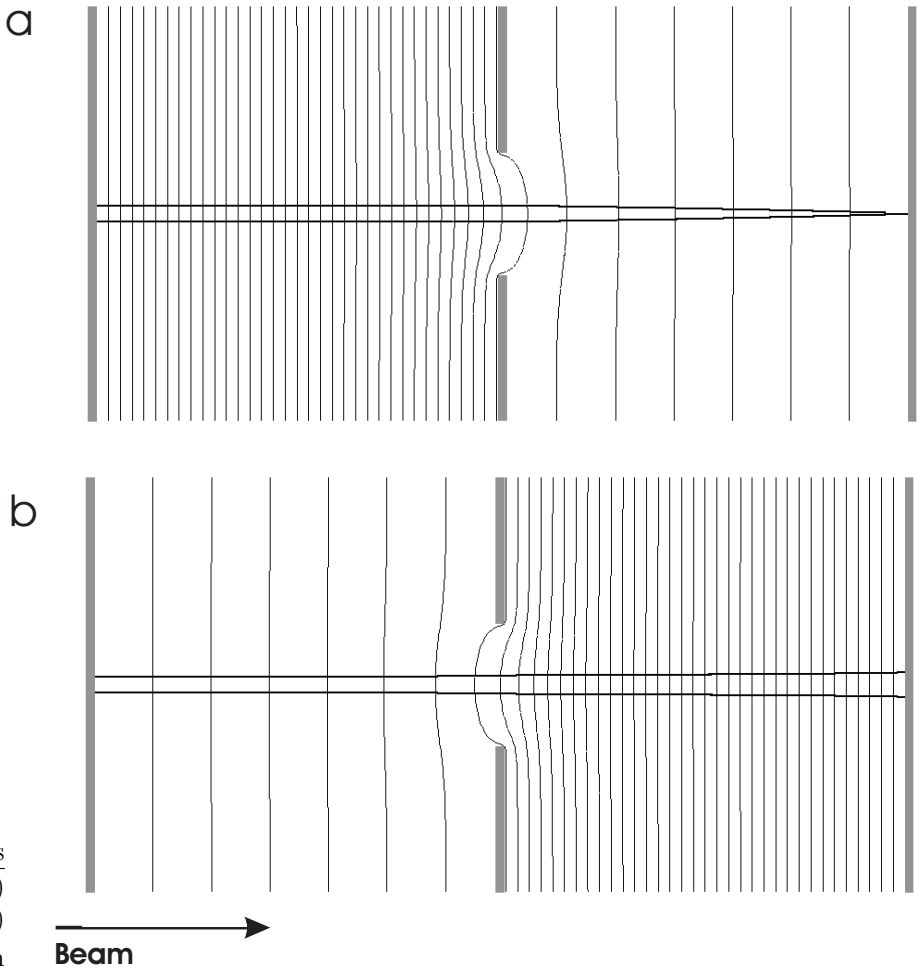

PSfrag replacements
a)
b)
Beam Direction

Figure 3.7: Equipotential lines for the aperture lens and example trajectories for a beam moving from left to right. a) Ions move from a strong electric field (left) in to a weak electric field (right) the radial component of the field caused by the aperture acts so as to focus the ions. b) Ions move from a weak electric (left) to a strong electric field (right) the radial component of the field caused by the aperture acts so as to defocus the ions.

high field region. The aperture lens is non-linear and as such the focal length is somewhat dependant on the ions initial conditions. The non-linearity can also add to the emittance of the ion beam. However, as the beam enters into a cooling device such effects are not of concern as long as the emittance of the beam overlaps with the acceptance of the RFQ.

The deceleration optics for the RFQ were designed to use a number of such lenses (see figure 3.8). The ions enter the deceleration region through a grounded drift tube. The field created by the first deceleration electrode penetrates into the opening of the tube. The result is that the ions initially move from a region of relatively low electric field strength to one of high electric field strength. Therefore, the beam diverges as it exits the ground tube. The electric field between the first and the second deceleration electrodes is much weaker than that between the ground tube and the first deceleration electrode. Thus, the beam starts to converge as it passes through the first deceleration electrode. The potential between the second deceleration plate and the front of the RFQ is weaker than that between the first and the second deceleration plate and again the ion beam is focused as it travels toward the RFQ.

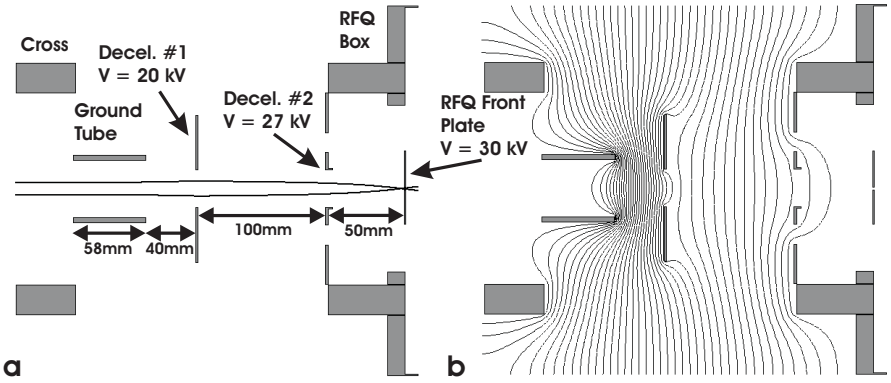

PSfrag replacements
a)
b)

Figure 3.8: a) The geometry of the deceleration optics and example ion trajectories. The ground tube and the deceleration plates have $30\,mm$ diameters. The RFQ front plate has a $5\,mm$ aperture. b) Equipotential lines for the deceleration geometry.

The acceptance of the deceleration system was found in SIMION (see figure 3.9) and is of the order of $100\,\pi\,mm\,mrad$ at $40\,keV$. We can define the useful acceptance of the deceleration system as being that which produces a decelerated beam whose emittance overlaps with the acceptance of the RFQ. This was found in SIMION by comparing the emittance of the beam after the RFQ front plate to the maximum acceptance of the RFQ. The useful acceptance was found to be on the order of $77\,\pi\,mm\,mrad$ at $40\,keV$. This is sufficiently large that efficient matching between the emittance of the ISAC beam and the deceleration system

will be achievable.

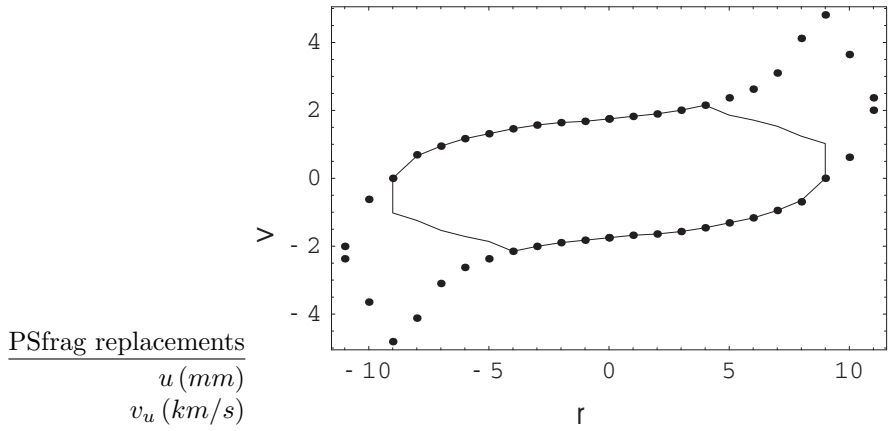

Figure 3.9: The acceptance of the deceleration optics (dots) with the useful acceptance shown (solid line).

3.2.2 Ion Cooling

The Monte Carlo cooling simulations were carried out in SIMION. Initially only the RFQ's geometry and the deceleration electrodes were defined. The RFQ was taken to be $700\,mm$ long with $r_0 = 10\,mm$ and $V_{pp} = 400\,V$. In order to apply the longitudinal potential the structure was segmented into twenty four pieces (see figure 3.17). The segments in the injection and trapping regions were made shorter than those in the center of the trap in order to give more control over the electric field in these regions. As the ions enter the RFQ they pass through seven $20\,mm$ segments. The center of the trap is segmented into eleven $40\,mm$ pieces. The exit region is segmented into five $20\,mm$ pieces with the final electrode only $9\,mm$ long. The segments are all separated by a $0.5\,mm$ gap. However, a $1\,mm$ gap was assumed for the purpose of simulation as this was the best resolution to which it was possible to define the electrode geometry. The cesium ions were initialized at the entrance to the ground tube of the deceleration optics with an energy of $60\,keV$. They were given a transverse emittance defined by the acceptance of the deceleration system and a longitudinal emittance that ensured that the ions would arrive at different times over one phase of the applied RF- field. For simulation purposes the RFQ was operated at $300\,K$, with $q = 0.4$ and gas pressure $2.5 \times 10^{-2}\,mbar$. The gas pressure was assumed to be uniform throughout the RFQ with negligible leakage of the gas through the entrance and exit apertures. It was found that cesium ions decelerated to an energy of $70\,eV$ when they entered the RFQ could be successfully trapped and cooled. A longitudinal electric field equal to $0.1\,V/cm$ was applied over the first twenty one segments of the system and a deeper potential well formed

on the final three electrodes with an applied electric field equal to $1.2\,V/cm$ (shown in figure 2.3). The trajectories of one thousand ions were simulated and a typical trajectory is shown in figure 3.10. The beam was trapped with 98% efficiency. The small loss of beam was caused by the cesium ions scattering into the RFQ's electrodes and by a slight mismatch between the acceptance of the system and the beams initial emittance. The simulations show that the ions reach equilibrium in approximately 600 μs, a factor of two slower than predicted by the drag model, with differences appearing for $E < 5\,eV$.

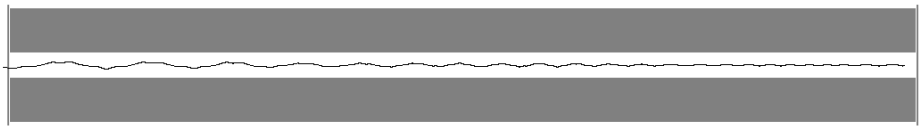

Figure 3.10: A typical ion trajectory, for an ion entering the buffer gas-filled RFQ (total length = $700\,mm$) from the left, calculated using the Monte Carlo code. The motion is effectively damped in the radial plane.

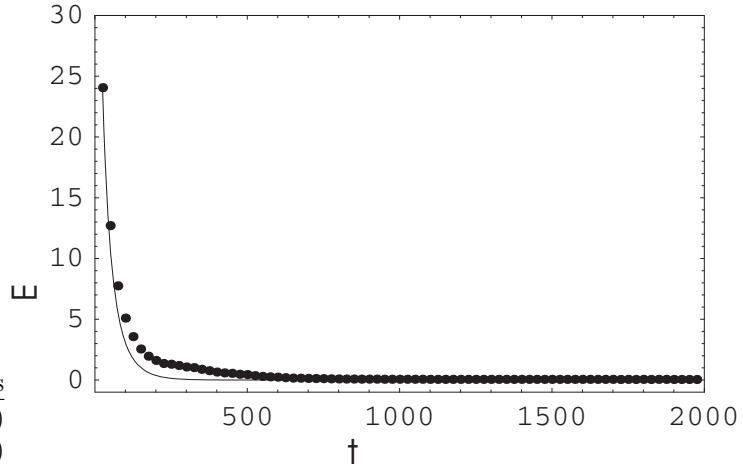

PSfrag replacements
$t\,(\mu s)$
Energy (eV)

Figure 3.11: Average energy of the ions in the RFQ as a function of time. The data points from the Monte Carlo simulation are overlayed on the predicted curve from the viscous drag model.

The final temperature of an ion cloud in the trap was studied as a function of operating parameter q. A cloud of ions was initialized in the final region of the trap with a random energy spread corresponding to a temperature of $800\,K$ and then allowed to cool for $500\,\mu s$. The position and velocity of each ion was then recorded at $0.02\,\mu s$ intervals over several periods of the applied RF.

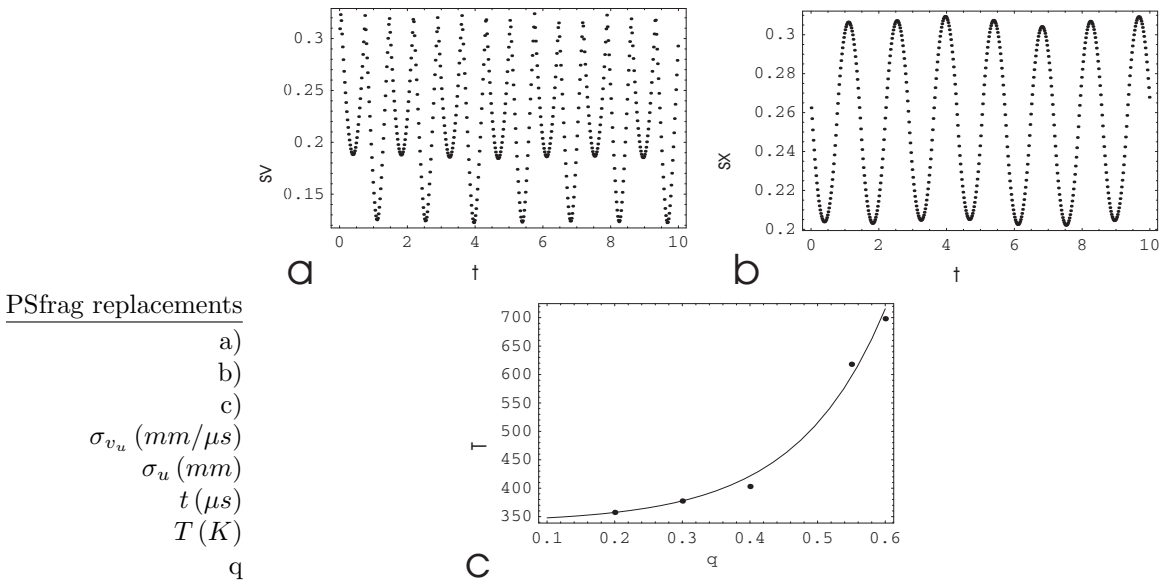

Figure 3.12: a) The standard deviation in velocity of a cloud of cesium ions cooled in helium as a function of time at $q = 0.3$. b) The standard deviation in position for the same cloud. c) The final temperature of a cesium cloud initially at $800\,K$, cooled for $500\,\mu s$ in helium as a function of q.

The standard deviation in position and momentum space of the ions was found for the ion cloud at each time step. This data was used to find the maximum standard deviation in position and momentum space over one period of RF and hence to define the final temperature of the ions in the trap. The results are shown in figure 3.12. The final temperature of the ion cloud in the trap was found to rise exponentially as a function of q. This is due to the effect known as RF heating. The ions micromotion is coherent and as such doesn't directly contribute to the temperature of the ion cloud but at any given time ions in a trap have energy due to the micromotion. The average of this energy over one complete cycle of the RF is zero, however if the ions are allowed to interact with a buffer gas energy from the micromotion can be randomly scattered. This random energy is no longer coherent and contributes to the temperature of the ions in the trap. Figure 2.6 shows that the amplitude of the micromotion rises as a function of q. This means that RF heating also rises as a function of q. The fact that RF heating is a process through which the ions can gain energy which is not included in the viscous drag model also explains the differences between the cooling times predicted by this model and the Monte Carlo simulation.

The simulation of the cooling of ions in the trap ignores the effects of ion-ion interactions. For low numbers of ions in the trap this assumption will hold. However as the space charge limit is approached these interactions are of course no longer negligible. This means that the model will underestimate the final temperature of ions in the trap.

3.2.3 Beam Extraction

The extraction optics along with the corresponding equipotential lines generated with SIMION are shown in figure 3.13. The optics consist of a set of steering electrodes before the ions are accelerated towards a plate at the extraction potential. The plate also serves as the first plate of an Einzel lens. Such a lens can be formed using the electrode geometry shown in figure 3.14. If the central electrode is placed at a potential that is higher than the two end plates the system will focus a positive incoming beam with the focal length dependant on the potential difference between the central electrode and the outer electrodes. After the lens the beam enters a drift tube that sits at the extraction potential.

Simulations of the extraction of ions were carried out in SIMION. Initial conditions for the ions in the trap were taken from the simulation of the cooling of the ions with $q = 0.3$. Two modes of extraction were studied. In the first mode only the potential on the last electrode (#24) was lowered and the ions drifted out of the trap. In the second mode the potential on the last electrode (#24) was lowered at the same time as the the potential on the third from last electrode (#22) was raised, thus kicking the ions out of the trap. For the purposes of the simulation the voltage pulses were assumed to have $10\,\mu s$ rise times and the effects of the buffer gas were assumed to stop as soon as the ions left the RFQ. The voltage on the second to last electrode (#23) sat at a potential 11 V below that of the last electrode (#24). The ions were extracted and accelerated to an energy of 2.5 kV and their properties analyzed at the

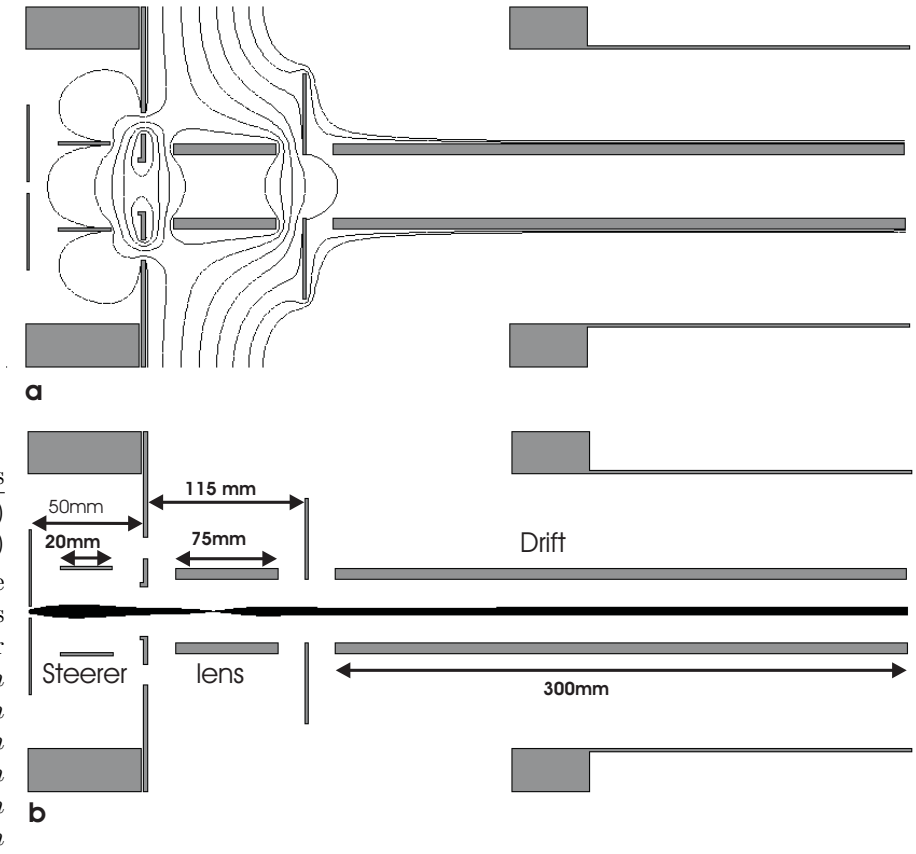

Figure 3.13: The extraction optics. The steerers are held at the same voltage as the DC offset applied to the last RFQ electrode upon extraction. The plates of the lens and the ground cone are held at the voltage on the steerers less the required extraction energy. The voltage on the central cylinder of the lens is held at approximately the same voltage as the steerer although this value has to be adjusted slightly so as to obtain a parallel beam. The exact amount of the adjustment is dependent on the magnitude of the pulse applied to the RFQ electrodes and the extraction energy.

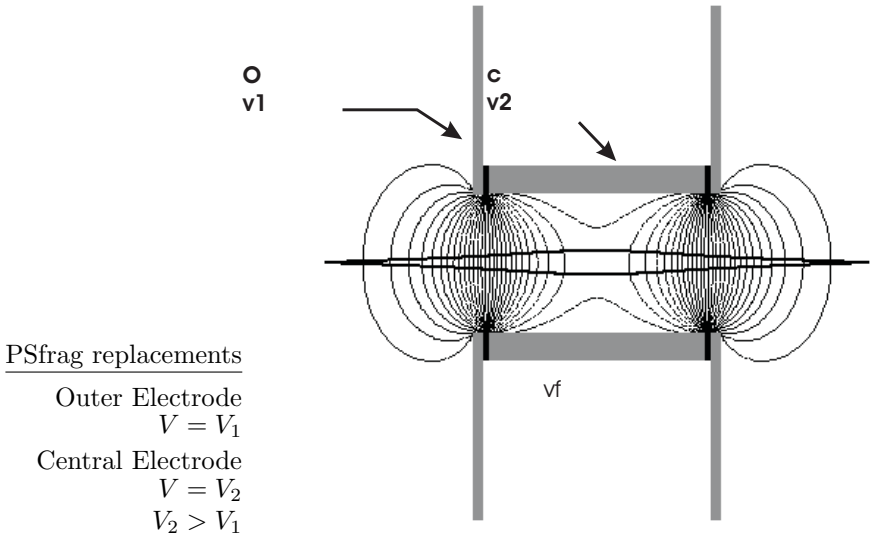

Figure 3.14: A simple ion lens can be formed using a cylindrical tube placed between two plates. The focal length of the system is dependant on voltage difference between the plates and the tube.

end of the drift tube. Typical emittance plots are shown in figure 3.15 and a summary of the results in table 3.1.

$\Delta V_{22}\,(V)$	$\Delta V_{24}\,(V)$	$\varepsilon_{t_{rms}}$ $(\pi\, mm\, mrad)$	$\varepsilon_{l_{rms}}$ $(eV\mu s)$	$\sigma_{ti}\,(\mu s)$	$\sigma_{en}\,(eV)$
0	-30	3.3±0.3	4.7±0.2	1.13	1.04
0	-60	4.2±0.1	7.4±0.3	0.78	2.42
30	-30	3.8±0.2	1.3±0.1	0.28	1.31
60	-60	3.6±0.1	1.4±0.1	0.15	2.48
500	-500	4.8±0.2	1.8±0.1	0.06	10.20

Table 3.1: Simulated properties of the extracted ion beam for different extraction pulses.

In the absence of buffer gas we would expect the emittances of all the extracted beams to be equal. Gently lowering the trapping barrier would result in the ions slowly drifting out of the trap. The time of flight distribution of the bunch would be wide whereas the energy spread would be small. Conversely if the ions were kicked hard out of the trap the energy spread would be large and the time of flight distribution narrow. For a bunch extracted in the presence of a buffer gas we see that the emittances of the beams are not equal. This is due

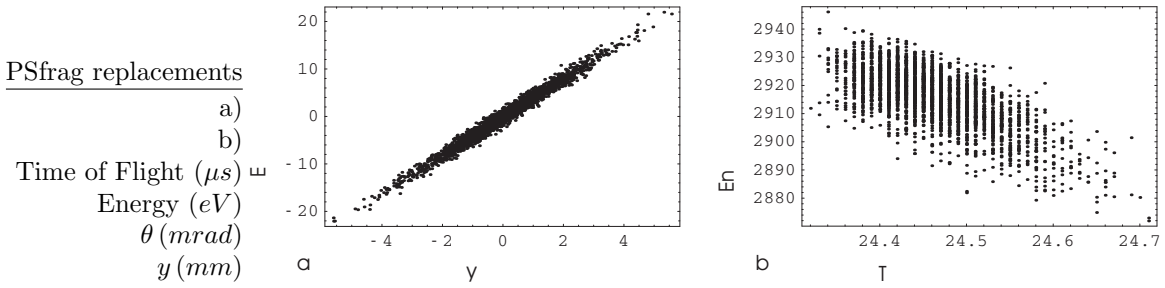

Figure 3.15: The transverse (a) and longitudinal (b) emittances of the cooled ion beam after extraction with a $\pm 500\,V$ pulse.

to the effects of buffer gas reheating. As the ions are pulled from the trap they are accelerated through the gas. Some of the energy gained from the extraction process is scattered into the transverse plane causing the ion cloud to expand. The ion clouds temperature when it leaves the trap is therefore higher than the final equilibrium temperature reached in the cooling process. However, we do see that the width of the time of flight distribution does fall as the magnitude of the extraction pulse is increased. We also see the width of the energy spread increase as the magnitude of the extraction pulse is increased.

With the simulations presented in this chapter it has been demonstrated that cooling and bunching of the ISAC beam with TITANs RFQ will be possible. The Monte Carlo simulations of the cooling of ions in the trap seem to verify the conclusions drawn from the simple viscous drag model. It was shown that the system can indeed trap and cool ions in an acceptable time frame ($< 1\,ms$) and that bunching of a continuous beam can be achieved. Using the Monte Carlo simulation it was further possible to predict typical transverse and longitudinal rms emittances for the bunches. Beam bunches with longitudinal emittances of better than $2\,eV\mu s$ were demonstrated at $2.5\,keV$. Transverse emittances on the order of $3\,\pi\,mm\,mrad$ were demonstrated at a $2.5\,keV$ extraction energy. This corresponds to an rms emittance of around $0.8\,\pi\,mm\,mrad$ at $30\,keV$. The exact emittance of the ISAC beam varies depending on the element produced. The best beams have average transverse emittances of around 3 to $5\,\pi\,mm\,mrad$ at $30\,keV$, the worst possible beams have rms emittances on the order of $10\,\pi\,mm\,mrad$ at $30\,keV$ (this emittance is defined by the acceptance of the ISAC beam line). In any case the bunches extracted from the RFQ have significantly improved transverse emittance.

3.3 RFQ Design, Experimental Setup and Status

The final design for the RFQ and extraction optics are presented here as well as details of the construction of the actual device. The design of the injection optics is given in the next chapter along with a description of the RFQ test stand.

3.3.1 The RFQ

The design of the RFQ was based on the results of the simulations described in this chapter. Using simulations it was demonstrated that an 700 mm long, square-wave-driven RFQ, segmented into 24 pieces with $r_0 = 10\,mm$ could be used to cool and bunch ion beams.

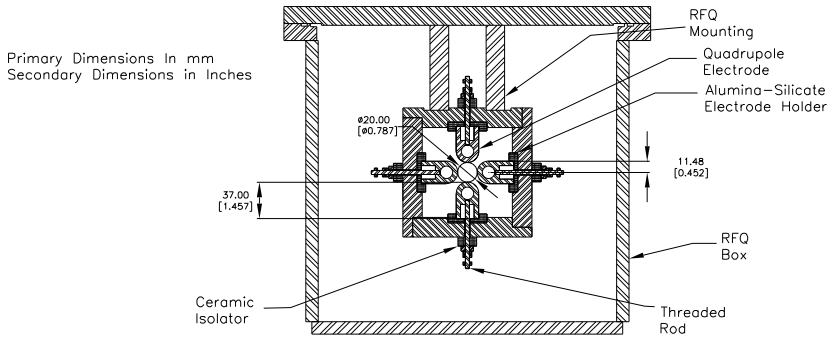

Figure 3.16: Mechanical drawing of the RFQ design (end view).

The structure of the RFQ is shown in figure 3.16. The RFQ electrodes were machined in a 'pillbox' shape. This allowed for the electrodes to be easily mounted in four specially machined alumina-silicate electrical isolators. The isolators were designed to hold the electrode pieces such that they were equally spaced and properly aligned. The isolators were held in place by three metal frames which were mounted on the lid of the RFQ box (see figure 3.17) . This meant that the structure could easily be lifted in and out of the box if maintenance was required. Opposing pairs of electrodes were wired together using stainless steel welding rod. The box lid had fifteen $2\frac{3}{4}''$ ConFlat flanges welded to it to allow for the mounting of electrical feedthroughs and for the attachment of a gas feeding system. A photo of the complete RFQ is shown in figure 3.18.

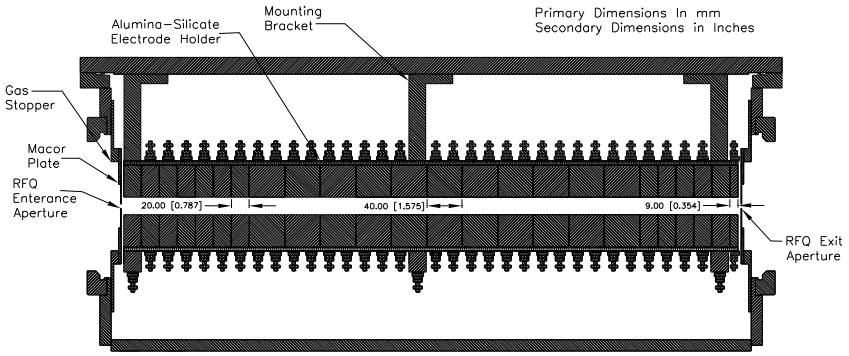

Figure 3.17: Mechanical drawing of the RFQ design (side view).

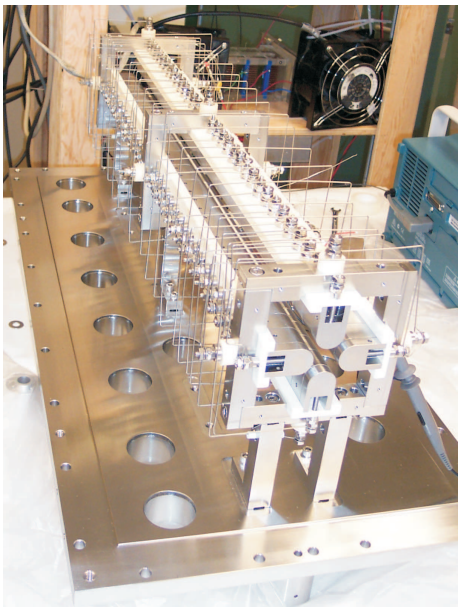

Figure 3.18: Photo of the complete RFQ setup before it was installed on the test stand.

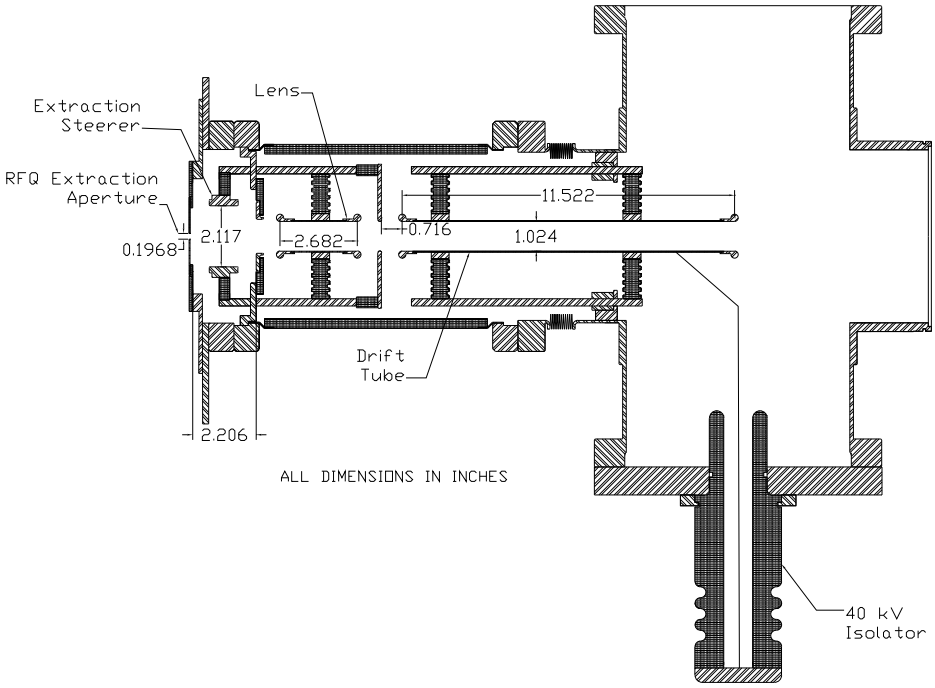

Figure 3.19: Mechanical drawing of the setup of the extraction optics.

3.3.2 Extraction Optics

The mechanical setup of the extraction optics is shown in figure 3.19 and photos in figure 3.20. The steerer plates were mounted on a ring via ceramic stands which was then attached to two rails. The first plate for the lens was mounted in exactly the same way as the second deceleration plate. The rails were mounted on the holder for the first plate of the lens with the central lens electrode and the second lens plate mounted on isolators as shown. The drift tube was mounted on two separate rails which were mounted on a stainless steel ring. The ring was attached to a second mounting ring which was welded to the inside of the second cross. The potential to the pulsed drift tube was supplied via a specially machined $60\,kV$ feedthrough. A hollow Macor isolator was attached to the base of the second cross via a $10''$ ConFlat flange. A stainless steel disk was attached to the base of the isolator with a vacuum seal provided via a Viton O-ring. Inside vacuum the the disk was attached to the drift tube using stainless steel welding rod. It is planned to provide the pulsing voltage on the tube using a Belhke HTS-651 fast switch. With an unmatched load the switch is able to switch up to $65\,kV$ in $22\,ns$.

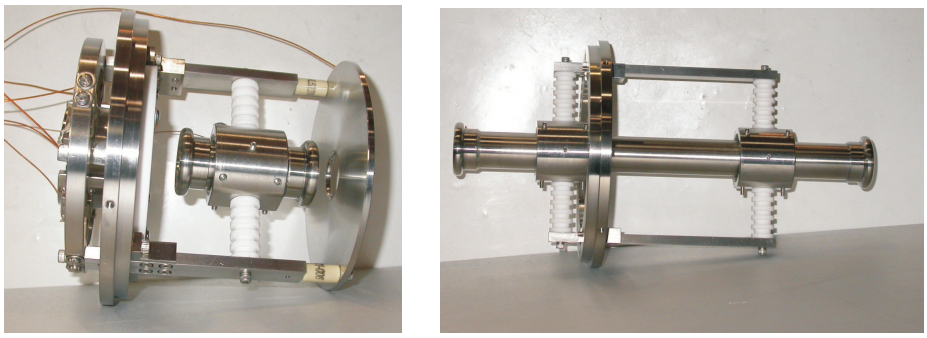

Figure 3.20: Photo of the extraction steerer and lens (left) and of the drift tube (right).

Chapter 4

Ion Optics for the Test Stand

An overview of the RFQ test stand was given in section 1.2.5. A system of ion optics for the test stand had previously been designed and built. However, in the engineering process a number of changes to the optics were made. The simulations presented here were carried out in order to try and understand the effects of these changes and to try and optimize beam transport through the system. The simulations were carried out in parallel with the experimental setup and testing of the system. In this chapter first a description of the experimental setup is given followed by details of the original simulations of the system, as per the final design. This is followed by a description of the first tests of the optics system and the obtained results. Finally these results are interpreted with the use of further simulations and improvements to the test setup in order to reduce observed beam losses are suggested.

4.1 Experimental Setup and Status

In this section an overview of the experimental setup is presented, some general features of the system are given here: All the metal parts to be placed in vacuum were machined out of stainless steel, i.e. the electrodes and the necessary support structure for them, with the electrode surfaces electropolished in order to minimize field irregularities and enhance out-gassing properties. Unless otherwise stated commercially available ceramic insulators were used to electrically isolate the electrodes. Various different types of power supply were needed, table 4.1 gives a list of the supplies and their uses. Wiring in vacuum was done using either Kapton coated cable or bare stainless steel welding rod with $1\,mm$ diameter, the rod was used as it was easy to shape but still rigid once bent into shape. Standard commercial high vacuum electrical feedthroughs were used to pass voltage from the power supplies to the electrodes in vacuum.

4.1.1 The Test Stand

In order to commission the RFQ before installation on the ISAC beam line the system was setup on a test stand (see figure 4.1). A large Faraday cage was built to house the parts of the system that would be held at high voltage and also a standard $19''$ electronics rack. The rack was isolated from the floor

Figure 4.1: Photo of the RFQ test ion stand. The ion source is mounted on cross #1. The Faraday cage is 2.5 m tall and the RFQ box is 800 mm long.

Use	Power Supply	V_{max} (V)	I_{max} (A)
High Voltage Bias	Spellman RHSR 30PN60	30×10^3	2×10^{-3}
Ion Source Power	Xantrax HPD 30-10	30	10000
Ion Source Bias	VME DC Module	100	?
Extractor	Spellman RHSR 05PN10	5×10^3	2×10^{-3}
1^{st} Quadrupole +VE	Glassman MJ10P1500	5×10^3	1.5×10^{-3}
1^{st} Quadrupole -VE	Glassman MJ10N1500	5×10^3	1.5×10^{-3}
2^{nd} Quadrupole +VE	Glassman MK40P1500	40×10^3	1.5×10^{-3}
2^{nd} Quadrupole -VE	Glassman MK40N1500	40×10^3	1.5×10^{-3}
1^{st} Steerer +VE	Spellman EPM3PX1672	3×10^3	10×10^{-3}
1^{st} Steerer -VE	Spellman EPM3NX1672	3×10^3	10×10^{-3}
Four-Way Switch +VE	Glassman MK40P1.8	40×10^3	1.8×10^{-3}
Four-Way Switch -VE	Glassman MK40N1.8	40×10^3	1.8×10^{-3}
4^{th} Quadrupole +VE	Glassman MJ10P1500	5×10^3	1.5×10^{-3}
4^{th} Quadrupole -VE	Glassman MJ10N1500	5×10^3	1.5×10^{-3}
5^{th} Quadrupole +VE	Glassman MK40P1500	40×10^3	1.5×10^{-3}
5^{th} Quadrupole -VE	Glassman MK40N1500	40×10^3	1.5×10^{-3}
2^{nd} Steerer +VE	Spellman EPM3PX1672	3×10^3	10×10^{-3}
2^{nd} Steerer -VE	Spellman EPM3NX1672	3×10^3	10×10^{-3}
1^{st} Decel.	FuG HCL 14-20000	20×10^3	1.5×10^{-3}
2^{nd} Decel.	FuG HCL 14-20000	20×10^3	1.5×10^{-3}
RFQ Square Wave	Xantrax XFR 6002	600	2
RFQ DC Offsets	VME DC Module	40	?
RFQ Extraction	VME DC Module	500	?
3^{rd} Steerer	VME DC Module	2×10^3	?
Einzel Lens Plates	FuG HCN 14-3500	3.5×10^3	4×10^{-3}
Einzel Lens Tube	FuG HCN 14-12500	12.5×10^3	1×10^{-3}
Drift Tube	Glassman MX60P0.8	60×10^3	8×10^{-4}

Table 4.1: List of power supplies for the RFQ test stand.

using ceramics and floated at high voltage via an isolation transformer. All the electronics, both at ground and high voltage, and the vacuum system were set up so that they could be controlled remotely using the TRIUMF standard EPICS control system. A custom vacuum box and two custom crosses were made from stainless steel. The crosses were placed at either end of the Vacuum box at ground potential. They were electrically isolated from the vacuum box using two hollow alumina-silicate insulators. The box was designed to house the RFQ and hence to sit inside the Faraday cage. It was mounted on a tripod structure which was electrically isolated from the floor using ceramics. Rough vacuum was achieved using a single oil free Varian TriScroll 300 pump. High vacuum pumping was provided using two $1000\,l/s$ Varian Turbo-V 1001 Navigator pumps backed with a single oil free TriScroll 300 pump. The turbo pumps were mounted on the crosses at ground potential. Vacuum measurements were

made using Granville-Phillips 275 Convectron Gauges ($P \geq 1 \times 10^{-4}\, mbar$) and Varian IMG-100 cold cathode gauges ($1 \times 10^{-9} \leq \mathrm{P} \leq 1 \times 10^{-3}\, mbar$).

4.1.2 Ion Detection

For detection of ion currents a simple Faraday cup was used. If an ion beam impinges on a metal plate then the beam current can be read directly by placing an ammeter between the plate and ground. However, the ion beam can also cause secondary electrons to be released from the plates surface. Hence, the net current between the plate and ground can be greater than the beam current. To reduce this effect a cup is used instead of a plate. If the depth of the cup is much greater than its diameter then the probability of electrons leaving the cup is reduced leading to an improved current reading. A long narrow cup can only be used if the divergence of the ion beam is small. Usually this is not the case. A shorter cup can be used with an electrically biased plate at its entrance. By applying a negative voltage to the plate an electric field is created that repels the secondary electrons back into the cup. A standard Faraday cup design was created to be used through out the TITAN project (shown in figure 4.2). The depth of the cup is the same as its diameter however a second repeller ring is included. The maximum diameter of the cup opening is $30\, mm$ but this size can be made smaller by changing the front plate. Current measurements were made

PSfrag replacements
63.5 mm
30 mm
60.3 mm
18 mm
Ion Beam
Repeller Ring
Front Plate
Cup
A
a)
b)

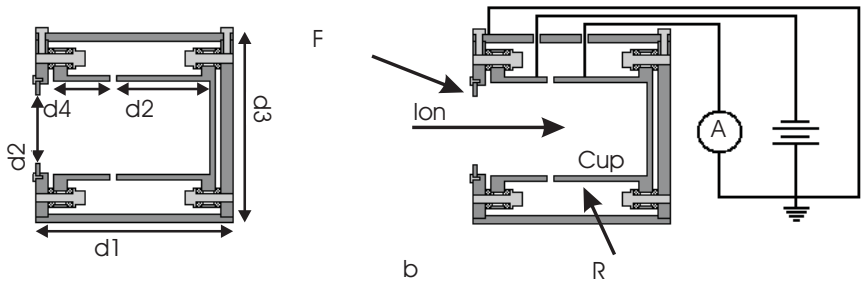

Figure 4.2: a) The Faraday cup design. b) An ion beam enters the cup and the beam current is read using a pico-ammeter. The negative bias is supplied from a battery with $V \approx -150V$.

at ground voltage using a VME module based picoammeter. At high voltage currents were found via measurement of the voltage drop over a $75\, M\Omega$ resistor chain using a Fluke 85-3 DMM.

4.1.3 The Test Ion Source

A commercial cesium surface ion source was purchased (see figure 4.3). The source consists of a rhenium filament potted in an alumina insulator. The alumina is in thermal contact with the emission surface which consists of an

alumino-silicate of cesium fused into a porous tungsten disk. The filament is heated by passing a current through it which in turn heats the alumina and the emission surface. This causes cesium ions to be released through the process of thermionic emission [Ble36]. The source is wrapped in molybdenum and has three molybdenum support legs welded to it which serve as the current return path. The source can typically produce ion currents in the range of nanoamperes to microamperes. The amount of current is set by controlling the temperature of the source. This allows one to simulate typical beam currents expected from the ISAC facility.

Figure 4.3: Schematic view of the cesium ion source.

4.1.4 The Beam Injection System

The beam injection system comprises a stable ion source, four-way switch,deceleration optics, quadrupole triplets and beam steerers. The purpose of each element is described in detail in the next section.

Ion Source and First Quadrupole Triplet

A schematic of the mechanical setup of the test ion source and the first quadrupole triplet is shown in figure 4.4. The test ion source was mounted on an $8''$ conflat flange which was connected to the common rail of the high voltage side of the isolation transformer. A stainless steel pillar was attached to the $8''$ flange in order to mount the ion source. The pillar was hollow with large holes cut into its body. These holes allowed both for efficient vacuum pumping of the pillar and for wires to be fed back to the electrical feedthrough (mounted on the $2\frac{3}{4}''$ flange shown). The source itself was held between two stainless steel plates isolated from the pillar using ceramic stands. The puller plate was mounted on the source holder again isolated using ceramics. The extraction cone was mounted on a $10''$ ConFlat flange. The $10''$ flange was mounted on cross #1 and held at ground potential.

The first quadrupole triplet was mounted on the same $10''$ flange as the extraction cone. Four rails were mounted on the base of the flange and the quadrupoles were mounted on the rails using ceramic insulators. The steerers

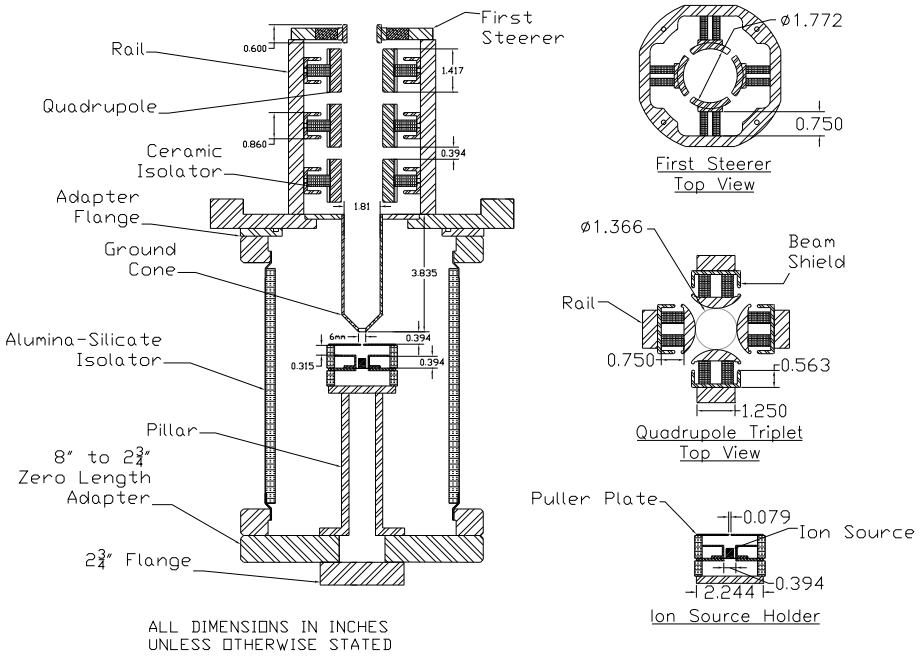

Figure 4.4: Mechanical drawings of the test ion source and first quadrupole.

were mounted on a stainless steel frame using ceramic stands. The frame was then attached to the four rails used to mount the quadrupoles.

Four-Way Switch

The setup of the four-way switch is show in figure 4.5. The four electrodes of the four-way switch were mounted on a stainless steel frame using specially machined Macor insulators. The frame itself was attached to a plate welded into the first cross. The actual four-way switch is shown in figure 4.6.

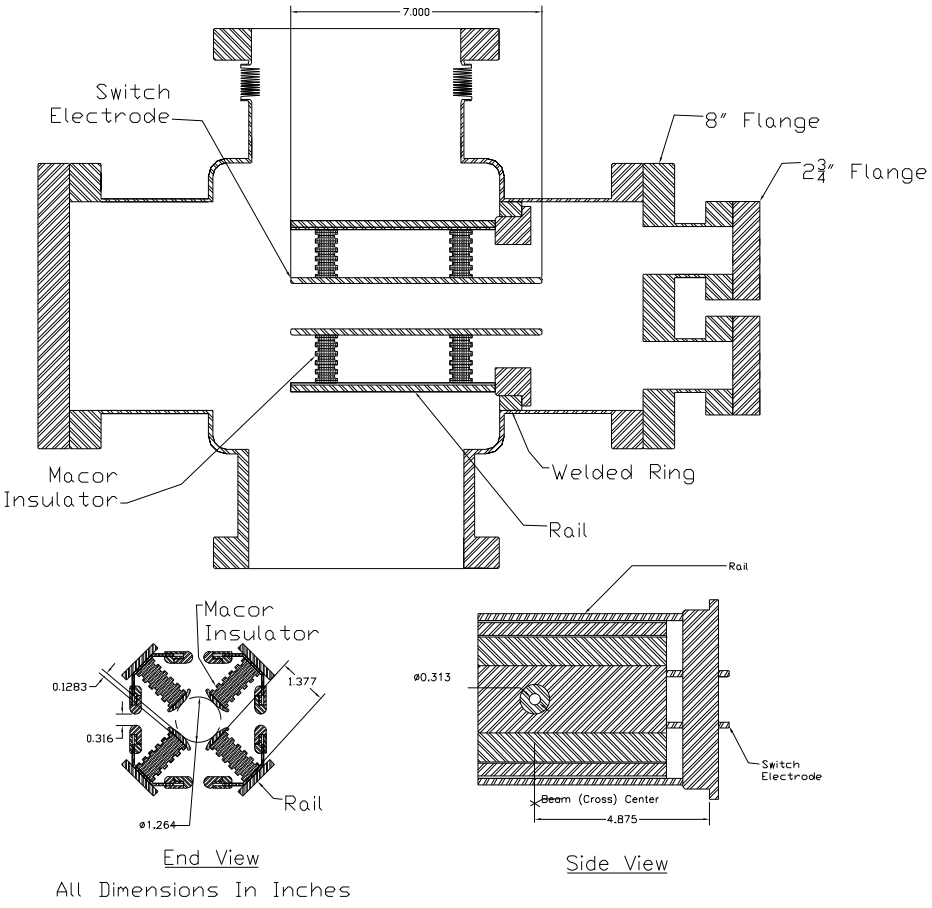

Figure 4.5: Mechanical drawing of the setup of the four-way switch.

Second Quadrupole and Deceleration Optics

The second set of quadrupoles were mounted on four rails in exactly the same manner as the first. These rails were held in place via a stainless steel ring

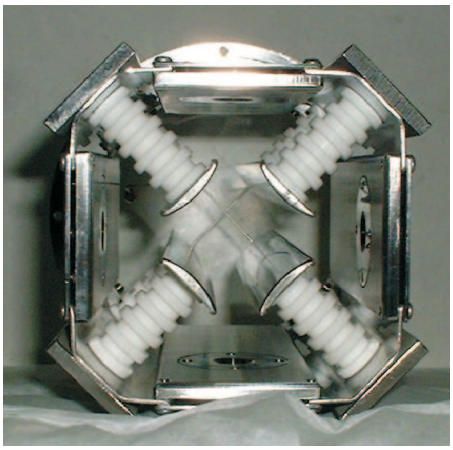

Figure 4.6: The four-way switch. For scale see figure 4.5.

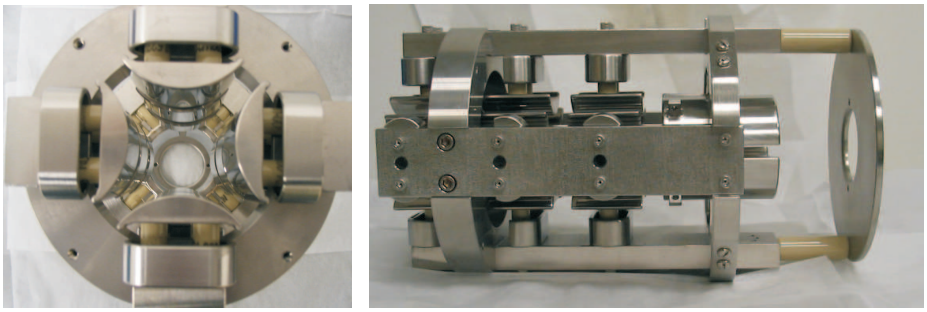

Figure 4.7: Photo of the second quadrupole, second steerer and first deceleration plate.

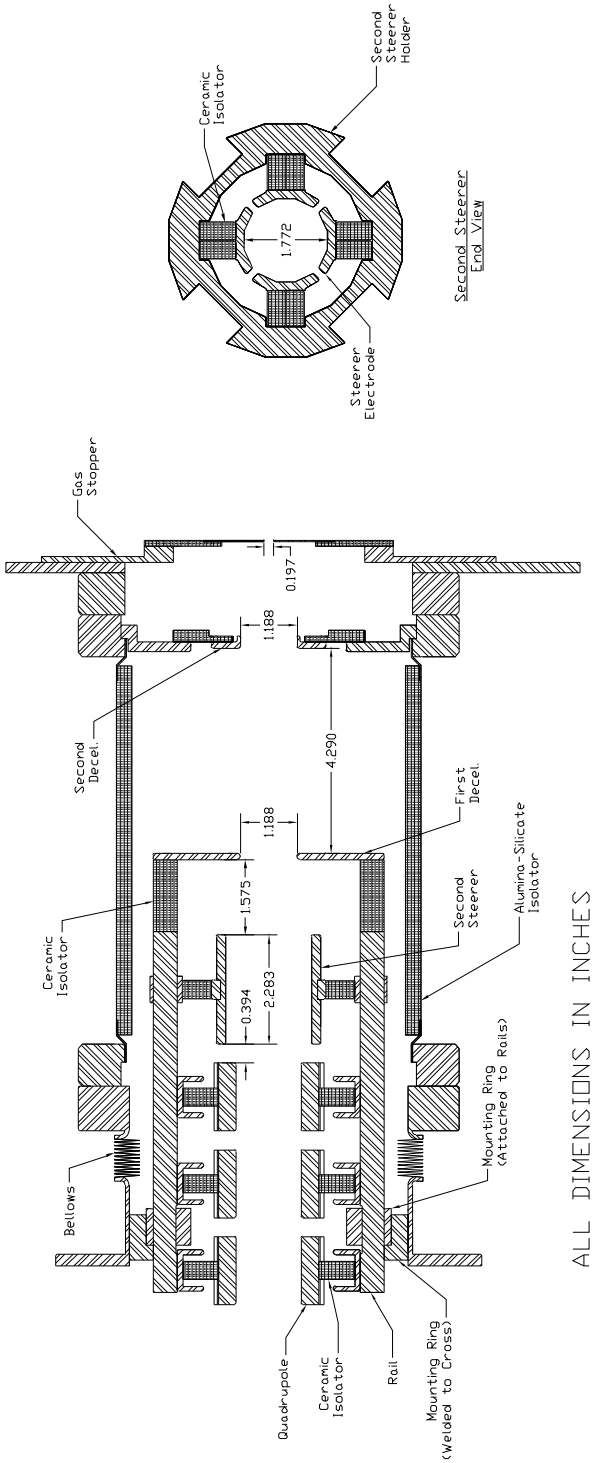

Figure 4.8: Mechanical drawing of the second quadrupole and the deceleration optics.

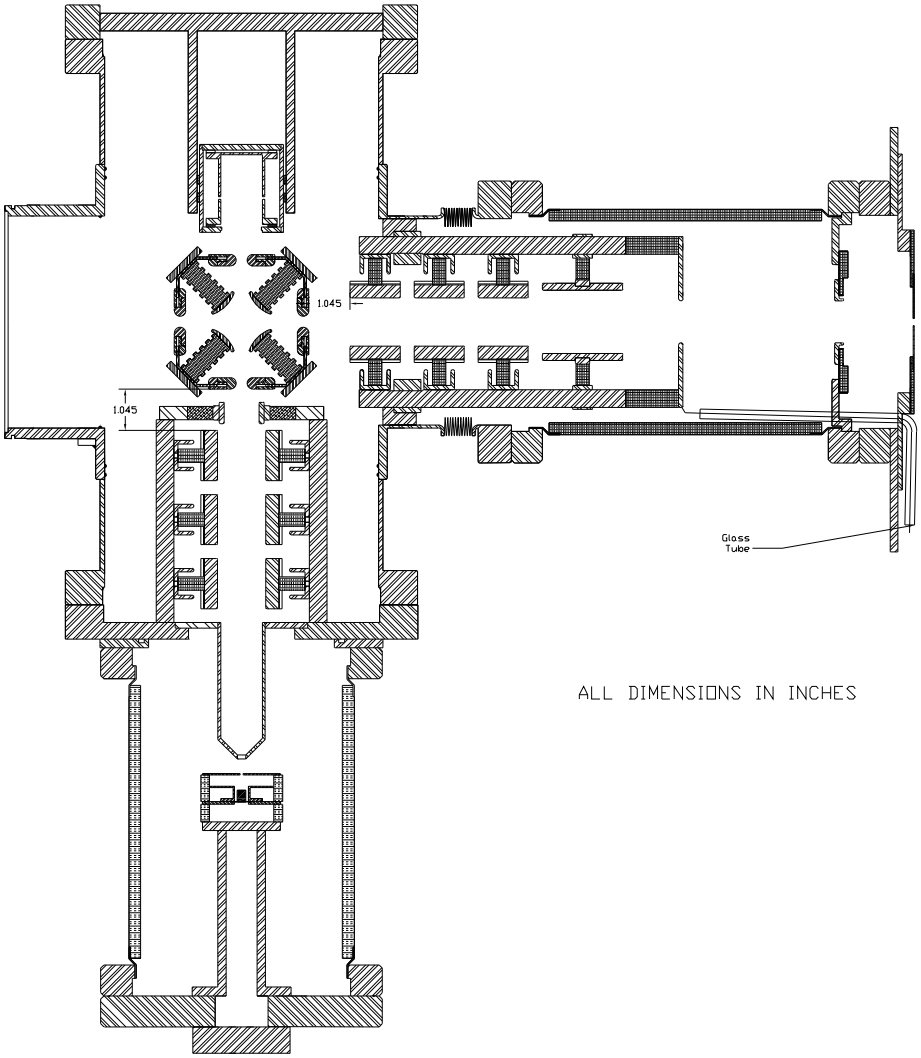

Figure 4.9: Complete mechanical drawing of the injection system.

which attached to a plate welded into the first cross (see figure 4.8 and figure 4.7). The second set of steering electrodes were mounted on a stainless steel frame which, in turn, was mounted on the rails.

The first deceleration plate was mounted on ceramic standoffs which were attached to the mounting rails for the second quadrupole triplet. A special stainless steel mounting ring was made to hold the second deceleration plate at the exit of the second alumina-silicate isolator. The deceleration plate was mounted on the ring via a Macor isolator. The RFQ box had to be sealed so as to contain the buffer gas. This was achieved using a stainless steel plate which was bolted to the inside of the RFQ box. A Macor disk was attached to the plate upon which a stainless steel plate with a $5\,mm$ aperture was mounted. The plate was electronically isolated from the RFQ box such that the current hitting the plate could be measured. This was useful in calibrating the ion optics. The electrical feedthroughs for the deceleration electrodes were mounted on the base of the RFQ box and the wiring was passed through the gas shield via two long glass tubes (see figure 4.9).

4.2 Simulation of the Test Stand Optics

4.2.1 The Test Ion Source

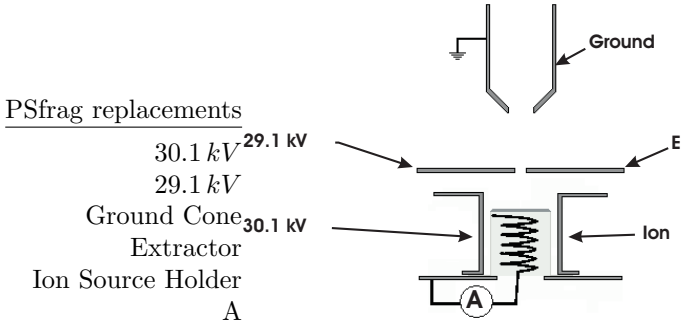

Figure 4.10: The proposed extraction optics for the ion source.

Ion optics were designed in order to extract the cesium ions produced by the ion source. In order to simulate typical ISAC beam currents it was only necessary to extract small ($I \approx 10\,nA$) currents from the source. Such currents are sufficiently low that the effects of space charge were neglected when designing the ion source extraction optics. A schematic of the extraction optics are shown in figure 4.10.

The ion source sits at high voltage (for test purposes around $30\,kV$) and the positive ions are accelerated toward the extractor which sits at a lower potential. The extractor is a plate with a small aperture in it that creates a weak accelerating electric field to pull the ions away from the source. The

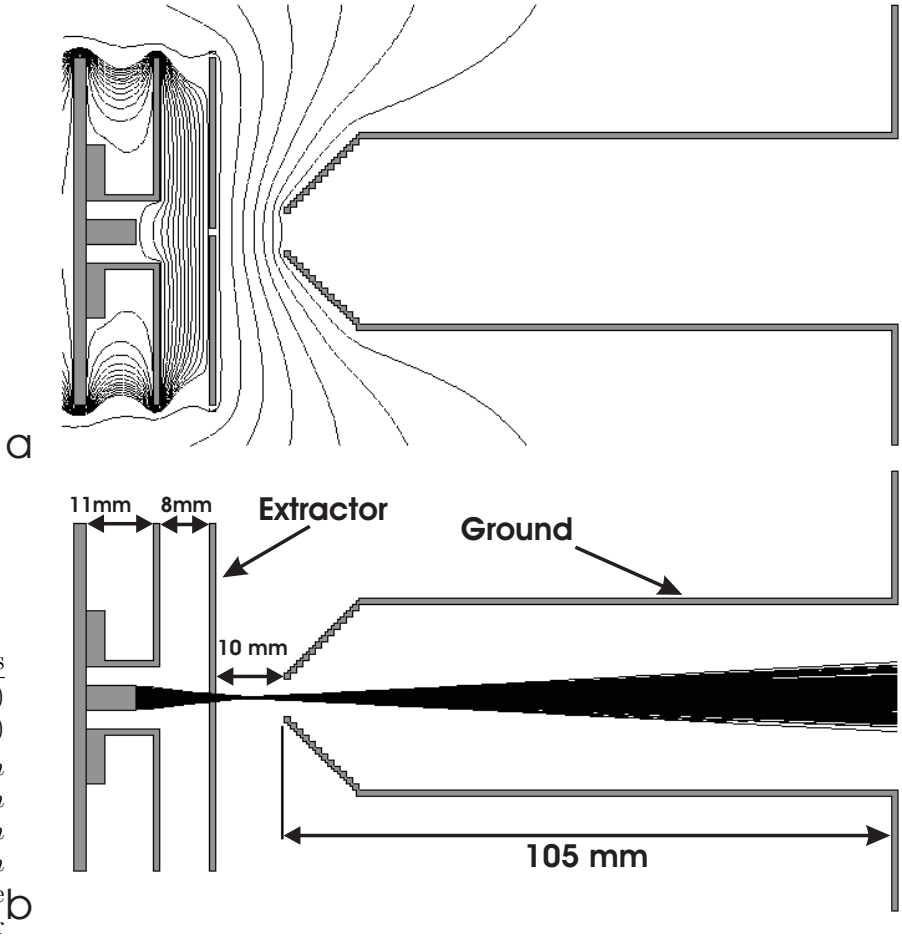

PSfrag replacements
a)
b)
105 *mm*
11 *mm*
8 *mm*
10 *mm*
Ground Cone
Extractor

Figure 4.11: a) Equipotential lines for the ion source extraction optics generated in SIMION. Between the source and the puller the lines correspond to 80 V decreases in electric potential, between the extractor and the cone the lines correspond to 4000 V steps. b) Simulated ion trajectories through the geometry.

emission surface sits further away from the extractor than the top plate of the source holder. This means that the electric field between the emission surface and the extractor is weaker than the field between the source holder and the extractor. This causes a radial component in the field which serves to focus the ions through the aperture in the extractor (see figure 4.11a). Once past the extractor the ions are accelerated through the fairly uniform field between the extractor and the cone.

Simulations of the ion source optics were carried out in SIMION. The source had a diameter of $6\,mm$ and a height of $7\,mm$, the aperture in the extractor had a $2\,mm$ diameter. The opening aperture in the cone had $6\,mm$ diameter increasing to a maximum of $30\,mm$. The source was floated at $30.1\,kV$ with the puller at $29.1\,kV$ the cone had zero potential. The source operates at a maximum temperature of $1200\,K$ [Ave04] so the ions were initialized assuming a Maxwell-Boltzmann energy distribution at this temperature. The ions were assumed to originate on the surface of the source with a Gaussian spread in radial position with the radius of the source corresponding to three standard deviations. The corresponding trajectories for 500 ions are shown in figure 4.11b. Figure 4.12 shows the transverse and longitudinal emittances of the beam extracted from the simulation as the beam exits the extraction cone. A fit to 20000 simulated data points gives the transverse emittance $\varepsilon_{t_{rms-f}} = 4.5 \pm 1\,\pi\,mm\,mrad$ and substitution of the data into equation B.16 gives a value of $\varepsilon_{t_{rms}} = 3.9 \pm 0.4\,\pi\,mm\,mrad$. The rms longitudinal emittance can also be calculated using equation B.16 and yields the result $\varepsilon_{l_{rms}} = 1.09 \pm 0.03\,eV\mu s$.

PSfrag replacements
$x\,(mm)$
$\theta\,(mrad)$
Time of Flight (μs)
Energy (eV)

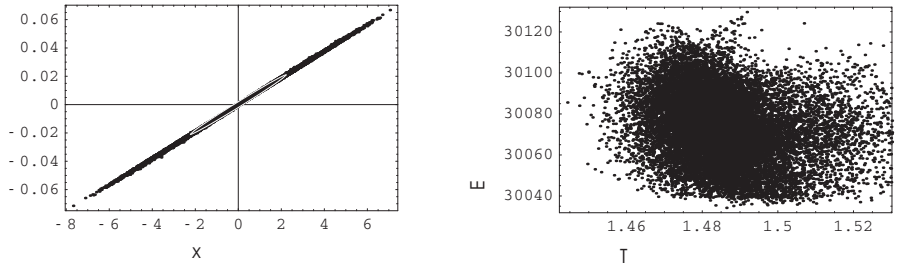

Figure 4.12: The transverse and longitudinal emittances of the simulated beam extracted from the ion source.

4.2.2 Quadrupole Triplet

In order to match the emittance of the beam extracted from the ion source to the acceptance of the four-way switch (see section for a description of the switch) it was decided to use a quadrupole triplet [Wol87]. Such a device uses a series of three electrostatic quadrupoles separated by small drift regions to focus an incoming ion beam.

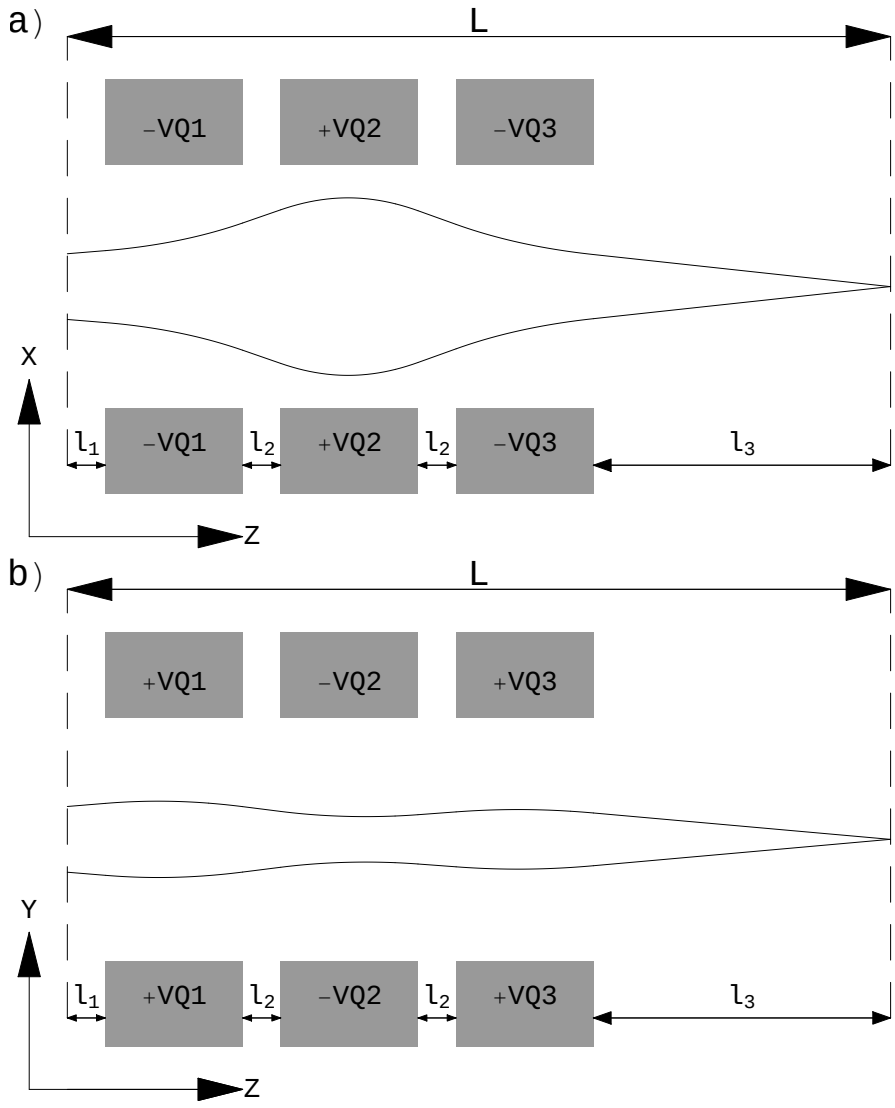

Figure 4.13: a) and b) Three electrostatic quadrupoles in series can be used to focus an ion beam in both transverse directions as shown.

In section 2.1 we saw that the ideal quadrupolar potential is given by:

$$\phi = \frac{V(x^2 - y^2)}{r_0^2}, \tag{4.1}$$

where, V is the amplitude of the voltage applied to the electrodes and r_0 is half the minimum separation between opposing electrodes. From this we get the equations of motion for ions in an electrostatic quadrupole that focuses in the x- direction as:

$$m\frac{d^2x}{dt^2} = -Ze\frac{2V}{r_0^2}x, \tag{4.2}$$

$$m\frac{d^2y}{dt^2} = Ze\frac{2V}{r_0^2}y, \tag{4.3}$$

$$m\frac{d^2z}{dt^2} = 0. \tag{4.4}$$

If we let:

$$g = \sqrt{\frac{2ZeV}{mr_0^2}}, \tag{4.5}$$

then:

$$\frac{d^2x}{dt^2} + g^2x = 0, \tag{4.6}$$

$$\frac{d^2y}{dt^2} - g^2x = 0. \tag{4.7}$$

Which we recognize as being identical to equations 2.19 and 2.20 with the resulting equations of motion:

$$\begin{aligned}\begin{pmatrix} x(t) \\ v_x(t) \end{pmatrix} &= \begin{pmatrix} cos(gt) & g^{-1}\,sin(gt) \\ -g\,sin(gt) & cos(gt) \end{pmatrix}\begin{pmatrix} x(0) \\ v_x(0) \end{pmatrix} \\ &= \boldsymbol{M_f}(g,t)\begin{pmatrix} x(0) \\ v_x(0) \end{pmatrix},\end{aligned} \tag{4.8}$$

$$\begin{aligned}\begin{pmatrix} y(t) \\ v_y(t) \end{pmatrix} &= \begin{pmatrix} cosh(gt) & g^{-1}\,sinh(gt) \\ g\,sinh(gt) & cosh(gt) \end{pmatrix}\begin{pmatrix} y(0) \\ v_y(0) \end{pmatrix} \\ &= \boldsymbol{M_d}(g,t)\begin{pmatrix} x(0) \\ v_x(0) \end{pmatrix}.\end{aligned} \tag{4.9}$$

The transfer matrix for an ion moving through a field free region is simply:

$$\begin{pmatrix} x(t) \\ v_x(t) \end{pmatrix} = \begin{pmatrix} 1 & t \\ 0 & 1 \end{pmatrix}\begin{pmatrix} x(0) \\ v_x(0) \end{pmatrix} = \boldsymbol{M_l}(t)\begin{pmatrix} x(0) \\ v_x(0) \end{pmatrix}. \tag{4.10}$$

Thus, the transfer matrix for the quadrupole triplet can be constructed from combinations of $\boldsymbol{M_f}$, $\boldsymbol{M_d}$ and $\boldsymbol{M_l}$. The amount of time that the ion takes to

traverse a quadrupole or a drift region can be simply related to its velocity in the z- direction and the length, l, of the quadrupole or drift region:

$$t = \frac{l}{v_z} \simeq \frac{l}{v} \tag{4.11}$$

Hence, the total transfer matrix for the quadrupole triplet can be given as:

$$\boldsymbol{M}_X = \boldsymbol{M_l}(l_3)\boldsymbol{M_f}(g_1, l_q)\boldsymbol{M_l}(l_2)\boldsymbol{M_d}(g_2, l_q)\boldsymbol{M_l}(l_2)\boldsymbol{M_f}(g_3, l_q)\boldsymbol{M_l}(l_1) \tag{4.12}$$

$$\boldsymbol{M}_Y = \boldsymbol{M_l}(l_3)\boldsymbol{M_d}(g_1, l_q)\boldsymbol{M_l}(l_2)\boldsymbol{M_f}(g_2, l_q)\boldsymbol{M_l}(l_2)\boldsymbol{M_d}(g_3, l_q)\boldsymbol{M_l}(l_1) \tag{4.13}$$

$$\boldsymbol{M}_Z = \boldsymbol{M_l}(L) \tag{4.14}$$

with the l_1, l_2, l_3, l_q and L defined as shown in figure 4.13. The triplet design had $r_0 = 17\,mm$ (which was the maximum radius spatially viable), $l_q = 36\,mm$ and $l_2 = 10\,mm$. The quadrupoles were mounted with the distance from the extraction cone to the first quadrupole $l_1 = 10\,mm$. To bring the beam to a focus in the center of the four-way switch $l_3 = 78\,mm$. The voltages on the first and third quadrupoles were set equal (i.e $g_1 = g_3$). With these constrains the final position and velocity of the ion are only dependant on two variables g_1 and g_2:

$$\begin{pmatrix} x(L) \\ v_x(L) \end{pmatrix} = \boldsymbol{M}_X(g_1, g_2) \begin{pmatrix} x(0) \\ v_x(0) \end{pmatrix} \tag{4.15}$$

$$\begin{pmatrix} y(L) \\ v_y(L) \end{pmatrix} = \boldsymbol{M}_Y(g_1, g_2) \begin{pmatrix} y(0) \\ v_y(0) \end{pmatrix} \tag{4.16}$$

For a stigmatically focused beam we require both $x(L) = 0$ and $y(L) = 0$ this gives:

$$m_{x_{11}}(g_1, g_2)\, x(0) + m_{x_{12}}(g_1, g_2)\, v_x(0) = 0, \tag{4.17}$$

$$m_{y_{11}}(g_1, g_2)\, x(0) + m_{y_{12}}(g_1, g_2)\, v_y(0) = 0, \tag{4.18}$$

Values for $x(0)$, $y(0)$, $v_x(0)$ and $v_y(0)$ were taken from the simulated ion beam extracted from the ion source. The equations were then solved numerically to get values for g_1 and g_2 and hence the required voltages on the quadrupole electrodes. The calculated voltages are $V_{Q1} = \pm 5212\,V$ and $V_{Q2} = \pm 7683\,V$ and the ideal trajectories of the ions are shown in figure 4.13.

In a pure quadrupolar field ions feel a force that is linearly proportional to their distance from the center of the quadrupole. In a real device the electrodes used are only approximations to the infinite hyperbola needed to create a purely quadrupolar field, this introduces non-linear forces on the ions as they pass through the triplet. Non-linear forces also occur due to the finite length of the electrodes and fringe fields between the quadrupoles. The effect of such non-linear forces is well known and causes the beam to undergo a process known as filamentation [Law77]. Filamentation causes the transverse emittance of the beam to increase and is hence undesirable. In order to study this effect in the quadrupole triplet between the ion source and the four-way switch the ion

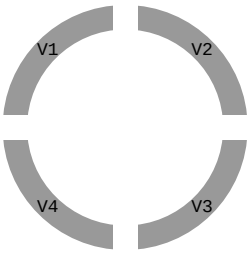

Figure 4.14: A simple beam steerer uses a ring electrode segmented into four pieces. The beam can be deflected by putting a potential difference between opposing plates.

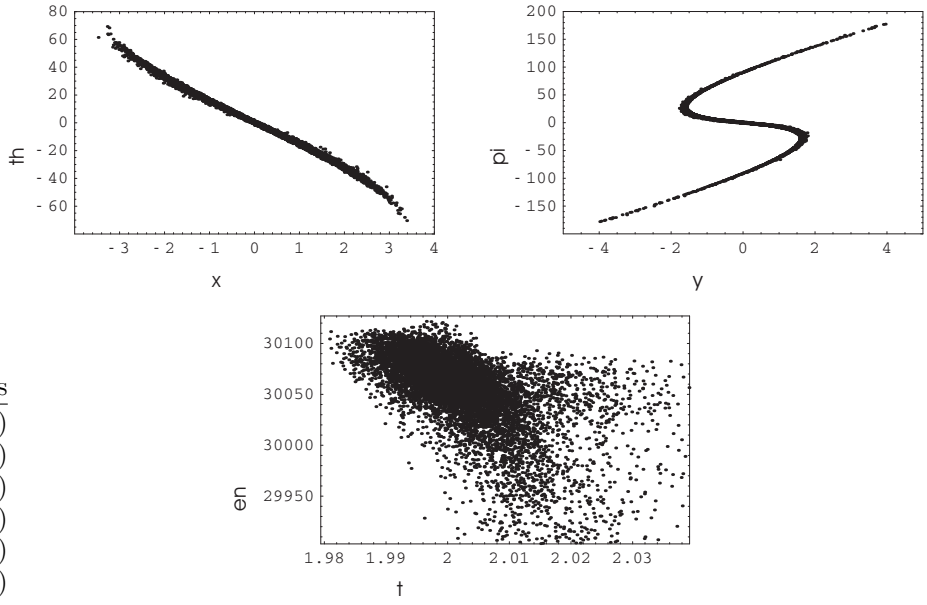

PSfrag replacements
$x\,(mm)$
$y\,(mm)$
Energy (eV)
Time of Flight (μs)
$\phi\,(mrad)$
$\theta\,(mrad)$

Figure 4.15: Emittances of the simulated ion beam after the first quadrupole triplet. The first quadrupole's focusing action was in the xz- plane. The observed 'tails' on the emittance plots are characteristic of filamentation.

trajectories were calculated using SIMION. Also included in the simulation was a simple beam steerer which could be used to correct for any misalignment in the experimental system (see figure 4.14). In the simulations the ions were taken to be travelling along the z- axis with the first quadrupole's focusing action in the zx- plane, the results are shown in figure 4.15. The emittance of the beam were found, using formula B.16, to be $\varepsilon_{x_{rms}} = 6.59 \pm 0.2\,\pi\,mm\,mrad$, $\varepsilon_{y_{rms}} = 130 \pm 0.5\,\pi\,mm\,mrad$ and $\varepsilon_{z_{rms}} = 3.35 \pm 0.1\,eV\mu s$ with the beam transported through the triplet with 99.5% efficiency.

The effects of filamentation in the F-D-F (Focus-Defocus-Focus) plane of the quadrupole were seen to be minor with a small increase in emittance however in the D-F-D plane the effects of filamentation were much worse. In SIMION the electrode geometry is defined on a grid, the resolution of the grid effects the accuracy to which the electrode surfaces can be defined and hence the accuracy of the calculated potential. However, when defining large scale structures it is not practical to define an electrode geometry on a fine grid. This is because the resulting potential array is loaded into the computers memory when the ions trajectories are calculated and large arrays use large amounts of memory. In the simulations of the ion source and quadrupole system a relatively coarse, $\Delta u_{min} = 1\,mm$, resolution was used. Hence, the effects of non-linearity due to the shape of the electrode faces were expected to be worse in the simulation than in reality. In order to check the magnitude of this effect simulations of a quadrupole triplet were carried for a range of different resolutions, $\Delta u_{min} =$ 0.2, 0.33, 0.5 and $1\,mm$, it was found that the resulting beams had emittances that were consistent to within 10%. This result also shows that the effect of non-linearity due to the imperfect shape of the electrode surfaces should be relatively small. Hence, we conclude that the main heating effect comes from the finite length of the quadrupoles and the fringe fields between them. The strength of the fringe field increases as a function of the distance from the center of the quadrupoles, due to the fact that the quadrupolar field is weakest at the center of the quadrupole. This explains the apparent asymmetry in the heating effect. In the F-D-F plane the beam always stays relatively close to the center of the quadrupole triplet whereas in the D-F-D plane the beam is much wider (see figure 4.13). Hence, the emittance growth is worse in the D-F-D plane than the F-D-F plane. This effect can only be reduced by increasing the length of the quadrupoles, this reduces the strength of the potential that needs to be applied to each electrode and hence the strength of the fringe field.

4.2.3 Four-Way Switch

The four-way switch uses a quadrupolar field to bend the path of an ion beam. The principle setup is shown in figure 4.16. A positive ion beam enters the field and feels an attractive radial force perpendicular to its velocity and directed towards the negative electrode. If the field strength is properly chosen the ion beam is bent through 90°. If the potential is too strong the ions will move too far toward the negative electrode as it passes through the field either resulting in the beam being bent through more than 90° or in it hitting the electrode.

Conversely, if the field is too weak the ions are bent through less then 90°. If the polarity of the electrodes are reversed the ions are bent in the opposite direction. If the electrode potentials are all set the same the path of the beam is unaffected.

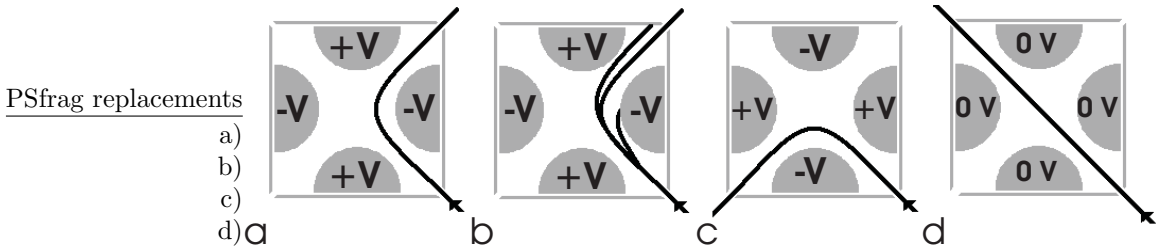

Figure 4.16: Four-way switching is achieved using semi-circular electrodes in a quadrupolar geometry. The field behind the electrodes is truncated by a ground plane. In each case the beam enters from the bottom right. a) If the correct potential is applied to the electrodes the ion beam is deflected through 90°. b) If the potential is too weak/strong the beam is deflected through less/more than 90°. c) If the polarity of the electrodes is reversed the beam steerers in the opposite direction. d) If no potential is applied then the beam is not deflected.

Ion trajectories in the ideal quadrupolar structure can be calculated using equations 4.8 and 4.9. Consider ions entering the electrode geometry shown in figure 4.17a. We define the R- axis as the axis at 45° to both the x- and the y-axis. Due to the symmetric nature of the electrode geometry ions will ideally enter the quadrupole along the R- axis i.e with $x(0) = y(0)$ and $v_x(0) = v_y(0)$. If the ions are then bent through 90° they will exit the trap at time T later with $x(T) = -x(0)$, $y(T) = y(0)$, $v_x(T) = v_x(0)$ and $v_y(T) = -v_y(0)$. The steerer was designed to steer the test ion beam with an energy of approximately $30\,keV$ so we consider a cesium ion with this energy entering the field along the R- axis. Equations 4.8 and 4.9 can be solved simultaneously to get the value of g and T corresponding to the ion path satisfying both the required initial and final conditions. Results of the calculated trajectories are shown, in figure 4.17b, for ions entering the field at different points along the R- axis. Changing the point along the R- axis at which the ions enter the field physically corresponds to changing the distance from the electrode face, h, at which the electrodes are truncated. From the shown trajectories it is clear that there is a maximum value for h above which the ions that enter the quadrupole hit the electrodes, where $h_{max} \approx 0.4\,r_0$. Recall that the form of the potential inside the quadrupolar structure is given as:

$$\phi = V\left(\frac{x^2 - y^2}{r_0^2}\right), \tag{4.19}$$

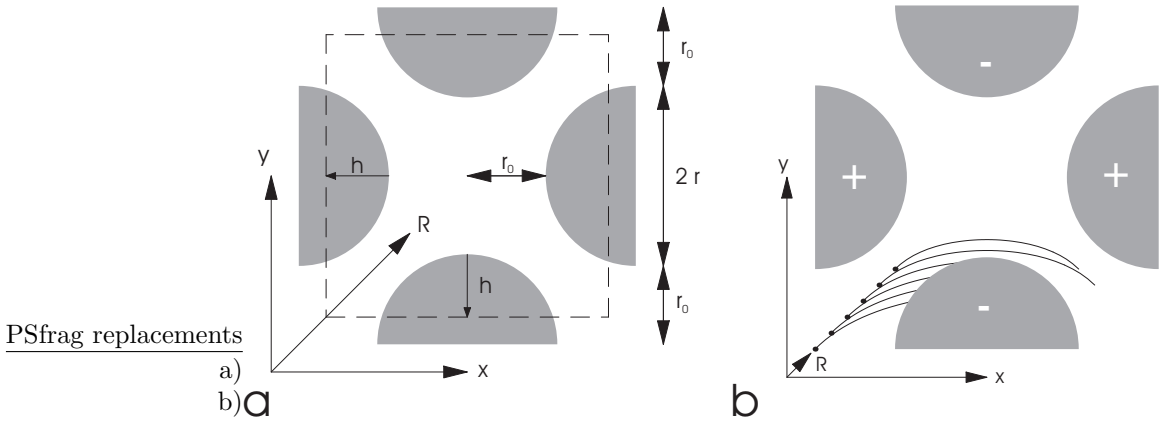

Figure 4.17: a) The geometry of the quadrupolar deflector. b) Calculated ion trajectories for ions starting at different points along the R- axis.

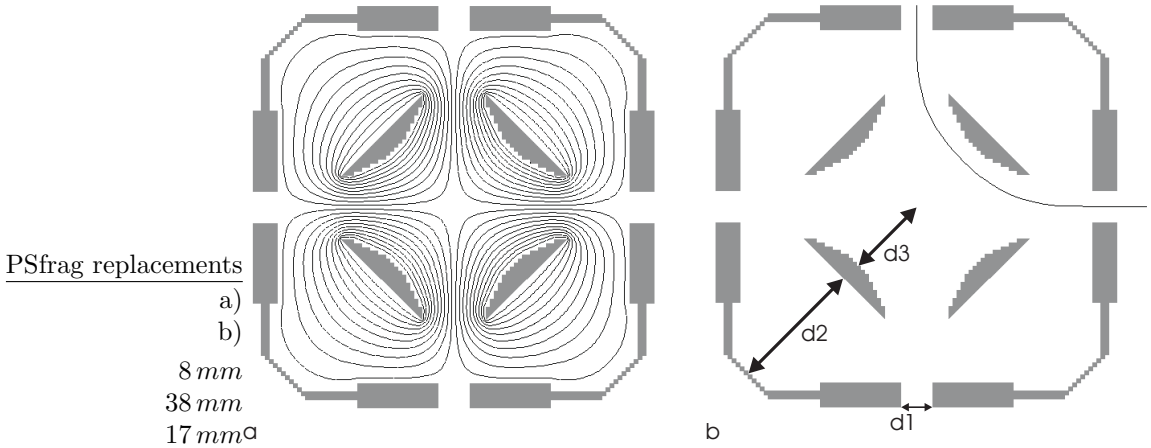

Figure 4.18: a) The potential generated by the four-way switch. b) A simulated ion trajectory where the ion is bent through 90°.

where V is the amplitude of the voltage applied to the electrodes. We consider two systems both have the same applied potential but $r_{0_1} = 2\,r_{0_2}$. An ion enters the first system along the R- axis and is bent through 90°. If an ion of the same energy enters the second system along the R- axis it will also be bent through 90° as its x- and y- co-ordinates will be double those of the original ion. The ions effectively see the same potential even though the two systems are different sizes. The potential to be applied to the electrodes is independent of the value chosen for r_0 and hence:

$$gr_0 = \sqrt{\frac{2zeV}{m}}, \tag{4.20}$$

is a constant for a given value of h and initial ion energy.

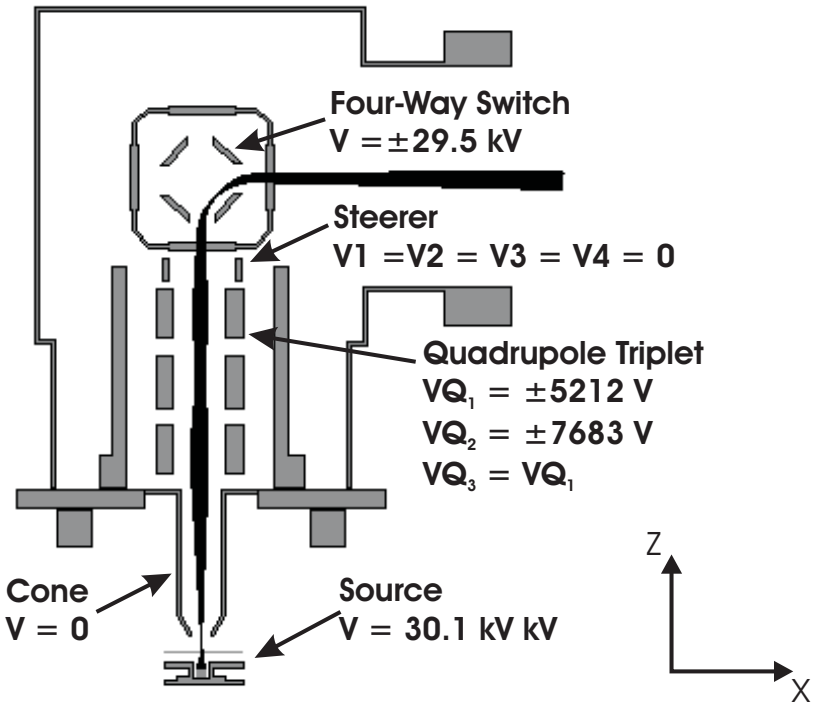

Figure 4.19: Simulated trajectories of the ions extracted from the test ion source being passed through a quadrupole triplet and steering elements before passing through the four-way switch.

It was decided to take a value for $h = 0.2\,r_0$. The value of g satisfying the required initial and final conditions for this steerer at a value of $r_0 = 1\,m$ was then found. This yields a value for $V = 20\,kV$. The shortest distance between a positive and negative electrode in the system is approximately equal to r_0.

Hence, we can estimate the maximum strength of the electric field between electrodes as:

$$E_{max} \approx \frac{2V}{r_0} = \frac{40000}{r_0}, \tag{4.21}$$

Taking a conservative estimate of the maximum possible field it is possible to hold between electrodes in high vacuum as 3 kV/mm, in the expected pressure range (1×10^{-8} to $1 \times 10^{-6}\, mbar$), yields a minimum allowable value for $r_0 = 14\, mm$. A conservative value for r_0 was chosen as $17\, mm$. The diameter of the apertures in the ground casing surrounding the four-way switch were chosen to be $8\, mm$. SIMION simulations of the four-way switch are shown in figure 4.18. The electrodes are mounted on the ground casing using ceramic insulators. The separation between the electrodes and the casing has to be sufficiently large such that the electrode potential does not discharge to ground along the surface of the ceramic. Experimental tests were carried out on specially machined Macor insulators and it was found that $38\, mm$ long insulators could hold the required voltages [Kan03]. The mean energy of the ions extracted from the simulated ion source floating at $30.1\, kV$ was found to be $30097.6 \pm 0.1\, eV$. In order to steer an ion with this energy through 90° the simulations show that voltages of $\pm 29550\, V$ must be applied to the positive/negative switch electrodes. The discrepancy between this and the calculated value arise due to the fact that the ions have to traverse quite considerable fringe fields before entering the four-way switch and that due to the resolution of the electrode geometry in SIMION it wasn't possible to set h exactly equal to $0.2\, r_0$.

SIMION simulations were then carried out of the ion source, the first quadrupole triplet and the four-way switch (see figure 4.19). Due to the asymmetric nature of the filamentation in the first quadrupole the beam trajectory was simulated first with the first quadrupoles focusing action in the xz- plane and then with it in the yz- plane. With the focusing action in the xz- plane the beam was transported through the steerer with 93% efficiency. The emittances (see figure 4.20) of the beam as it exits the four-way switch were then found, using equation B.16, to be $\varepsilon_{x_{rms}} = 1.33 \pm 0.1\, eV\mu s$, $\varepsilon_{y_{rms}} = 45.9 \pm 0.4\, \pi\, mm\, mrad$ and $\varepsilon_{z_{rms}} = 7.16 \pm 0.2\, \pi\, mm\, mrad$ where the common direction of the ions motion is along the x- axis as it exits the four-way switch. The apparent reduction in transverse emittance was due to the beam being collimated by the entrance and exit apertures of the four-switch. With the focusing action in the yz- plane the beam was transmitted through the steerer with 97% efficiency. Again, the emittances of the beam were calculated and were found be $\varepsilon_{x_{rms}} = 3.8 \pm 0.2\, eV\mu s$, $\varepsilon_{y_{rms}} = 6.6 \pm 0.1\, \pi\, mm\, mrad$ and $\varepsilon_{z_{rms}} = 84.9 \pm 0.5\, \pi\, mm\, mrad$.

4.2.4 Matching the Test Ion Source Beam to the Deceleration System

The emittance of the beam when it leaves the four-way switch doesn't completely overlap with the the acceptance of the deceleration system. It was decided to include a second quadrupole triplet after the four-way switch to match the outgoing beam to the deceleration system, with the second triplet identical to the

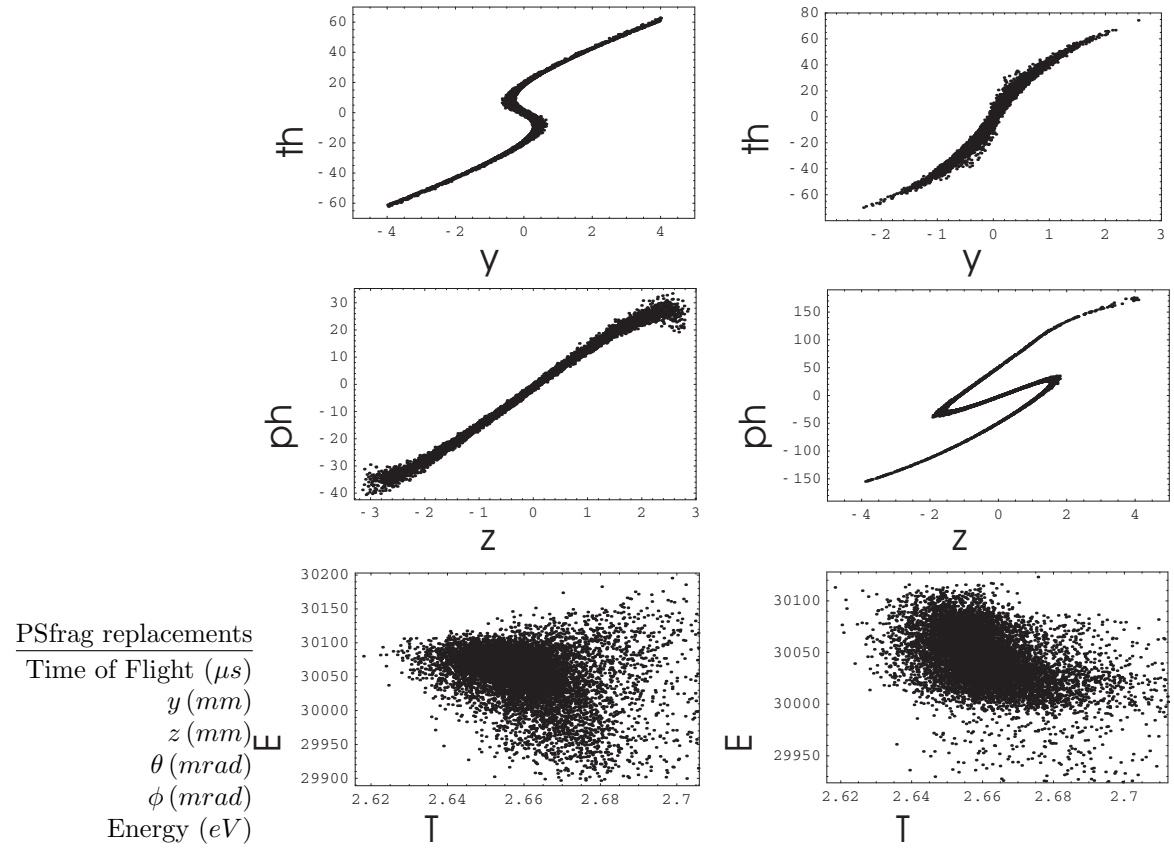

PSfrag replacements

Time of Flight (μs)
$y\,(mm)$
$z\,(mm)$
$\theta\,(mrad)$
$\phi\,(mrad)$
Energy (eV)

Figure 4.20: The emittances of the beam after it passes through the four-way switch with the first quadrupoles focusing action in the xz- plane (left) and the yz- plane (right).

first. It was placed a distance of 26 mm from the four-way switch and the end of the triplet was 10 mm away from the ground tube. The triplet was mounted at 45° to the vertical.

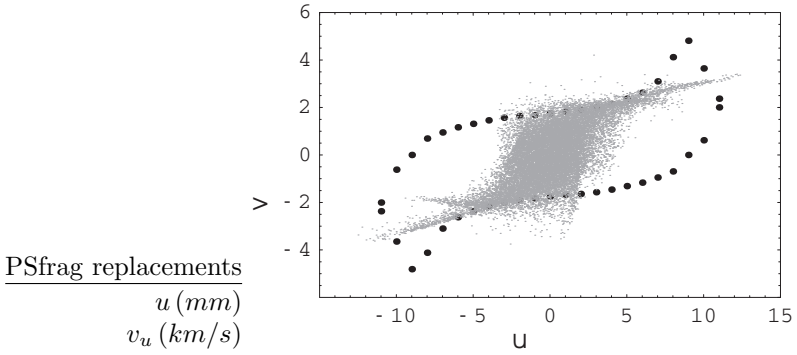

Figure 4.21: The transverse emittances of the ion beam after transformation by the quadrupole triplet (gray) and the acceptance of the deceleration system (black).

The transverse emittance of the beam as it exits the four-way switch with respect to an axes at 45° and 135° to the vertical were found by rotating the data from the previous section. The ideal transfer matrices were then used to find the emittance of the beam after the quadrupole triplet. The voltages required for the triplet in order to get the best match between the emittance of the beam and the acceptance of the deceleration system were then found. The best match occurred when the first quadrupole of the first triplet had its focusing action in the xz- plane and with $V_{Q4} = \pm 2300\,V$ and $V_{Q5} = \pm 4400\,V$ (see figure 4.21). These potentials are weaker than those applied to the first quadrupole triplet and hence the effects of filamentation are expected to be smaller in the second quadrupole. A full simulation of the ions trajectories from the ion source through to the deceleration was then carried out (see figure 4.22). The beam was transported through the whole system with 64% efficiency. The emittances of the beam as it exited the deceleration system were then found, using equation B.16, to be $\varepsilon_{x_{rms}} = 4.7 \pm 0.4\,eV\mu s$, $\varepsilon_{y_{rms}} = 1085.0 \pm 0.2\,\pi\,mm\,mrad$ and $\varepsilon_{z_{rms}} = 495 \pm 0.2\,\pi\,mm\,mrad$ (see figure 4.23). There are increases in the transverse emittances of the beam. This is due mainly to the fact that a deceleration of the beam is non-conservative (energy is taken from the system) and also to non-linearities in the deceleration system. Comparison between the maximum acceptance of the RFQ and the simulated emittance of the test ion beam shows that 91% of the beam should be transmitted.

Small losses of the beam occurred due to ions hitting the first deceleration plate and the RFQ front plate. The biggest cause of beam loss was due to the ions not having enough longitudinal energy to enter into the cooler. The deceleration optics were set so as the focal point would be exactly at the entrance

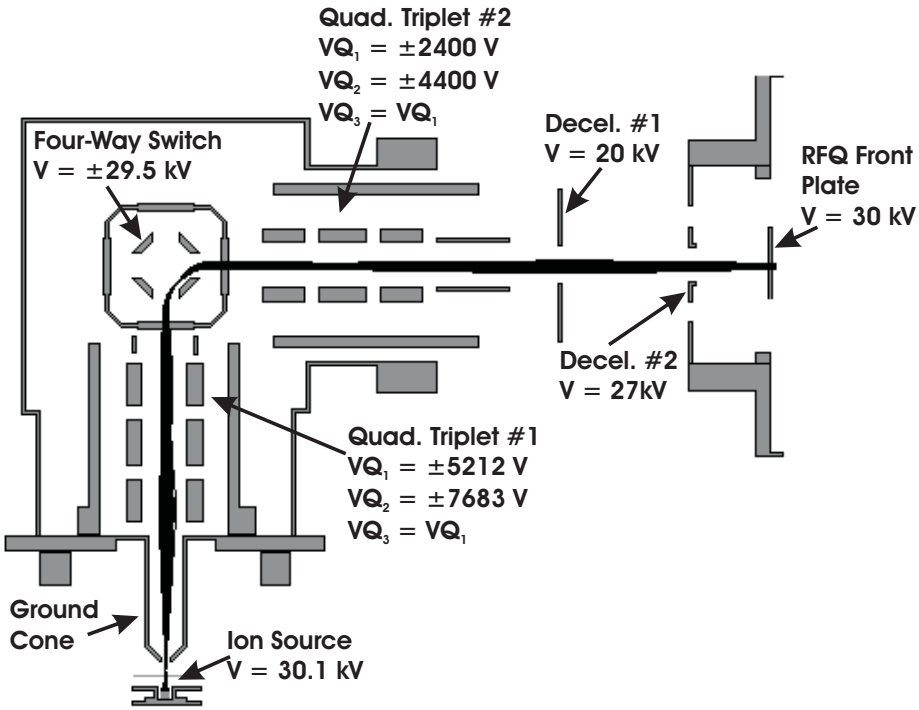

Figure 4.22: Schematic of the entire front end of the experimental setup (ion source, four-way switch and deceleration optics). Also shown are some simulated trajectories of the beam through the system.

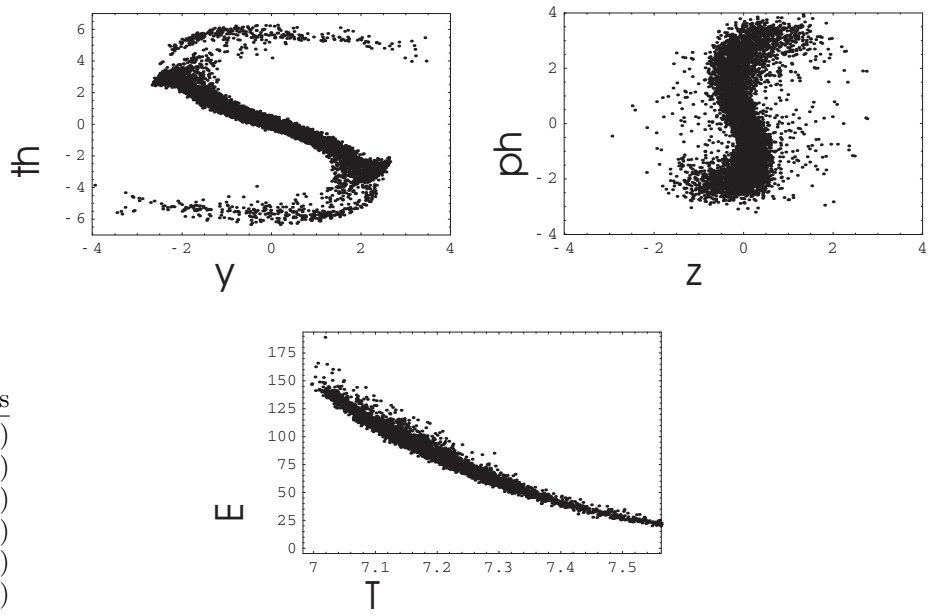

PSfrag replacements
$z\,(mm)$
$y\,(mm)$
Time of Flight (μs)
$\theta\,(mrad)$
$\phi\,(mrad)$
Energy (eV)

Figure 4.23: The emittances of the beam as it passes through the front plate of the RFQ.

of the RFQ. The ratio of the ions kinetic energy in the longitudinal direction to its energy in the radial direction is at its lowest at the focal point. Thus, better efficiency should be achievable by setting the focal point either slightly in front of or slightly behind the entrance aperture. This means that a larger component of the ions energy will be in the longitudinal direction at the entrance to the RFQ and hence increase the probability of the ion being admitted.

The average energy of the ions was found to be $90.6 \pm 0.3\,eV$. However, the plot of the longitudinal emittance reveals one of the weaknesses of the simulation method. The plot shows the ions having a maximum energy of $150\,eV$ at the entrance of the RFQ however there was only a $100\,V$ difference in potential between the RFQ and the ion source. Due to the large size of the system being simulated the potential had to be calculated for three separate geometries. The apparent gain in energy comes from a poor match between the potentials where the geometries meet. This means that the simulation will overestimate the injection efficiency as some ions that make it into the RFQ in the simulation will not have the necessary energy in reality.

4.3 Experimental Tests of the Source and Injection Optics

Before the installation of the four-way switch the ion source was tested by mounting a Faraday cup at the top of the first quadrupole. The source was floated at a potential $30100\,V$ above ground. A $4\,V$ potential was then placed over the source and after heating up a steady current of around $1.88\,A$ was drawn from the heating power supply. An approximate beam current of $40 \pm 2\,nA$ was measured from the ion source although the current was observed to fluctuate with time.

The four-way switch was then installed along with the second quadrupole and the deceleration optics. It was decided to mount a Faraday cup above the four-way switch. This would allow the beam current from the source to be measured for direct comparison to the current at later stages in the test system.

The voltages expected from the simulations were applied to the first quadrupole and the four-way switch. The first deceleration plate was connected to a voltage divider circuit which was used to measure the beam current impinging on the plate. The second quadrupole and second steerer were then set so as to steer the beam into the deceleration plate. The voltages on the first quadrupole and on the four-way switch were then tuned so as to maximize the current on the first deceleration plate.

A second Faraday cup was mounted inside the RFQ box behind the entrance aperture. The beam current on both the plate with the aperture and the Faraday cup was measured and the optics tuned so as to minimize the current on the plate and maximize the current on the cup.

The Faraday cup inside the RFQ box measured a fairly steady beam current of $9 \pm 0.2\,nA$ whilst the Faraday cup above the four-way switch measured a beam current of $33.8 \pm 0.5\,nA$. This showed that only about 24% of the beam entering the four-way switch was making it into the RFQ box. Also after around ten minutes the beam current inside the box was observed to start to drift back towards zero.

4.4 Comparison of Experiment to Simulations

A summary of the voltages applied to the electrodes in the experimental setup are shown in table 4.2 along with values obtained through the simulations. The experimental voltages applied to the first set of quadrupoles appear to be in good agreement with the simulated values. However there seem to be significant differences between the voltages applied to the other electrodes although as we will see these results can be interpreted by further use of the simulations.

There were two major physical differences between the simulated and the experimental system. First, an error in the manufacturing process lead to one of the flanges on the cross that held the ion source being welded on at a 17° angle to that required. Hence, the first quadrupole sat an an angle of 17° to that simulated. As shown this should not effect the required voltages to be

Electrode	V_{sim} (kV)	V_{exp} (kV)
Ion Source	30.1	30.1
Extractor	29.1	29.1
1^{st} Quadrupole	5.2	5.3
2^{nd} Quadrupole	7.7	7.5
Four-Way Switch +VE	29.5	26.2
Four-Way Switch -VE	-29.5	-26.5
4^{th} Quadrupole	2.3	3.3
5^{th} Quadrupole	4.4	5.0
1^{st} Decel.	20	23.5
2^{nd} Decel.	27	26.5

Table 4.2: Comparison of simulated and experimental values for the voltages applied to the injection system electrodes.

applied to the first quadrupole triplet. However, due to non-linear effects in the system this will effect the emittance of the beam as it exits the four-way switch. Secondly, the thickness of the electrodes in the four-way switch, h, is slightly different in the simulated system due to the rough grid size used to define the electrodes. This explains the difference in the simulated and the actual voltages on the four-way switch.

The effect of varying the potentials on the deceleration plate is to change the focal length of the deceleration system. The system was simulated in SIMION and it was found that the experimentally applied potentials moved the focal point $3\,mm$ downstream of the RFQ front plate. As noted in the simulations section this should help improve the transfer efficiency of ions into the cooler. These changes also effect the acceptance of the deceleration system. This combined with the rotation of the first quadrupole triplet can be used to explain the observed voltages on the second triplet. The ions trajectories were simulated through the rotated quadrupole and the four-way switch and the new emittances found. The ideal transfer matrices for the quadrupole triplet were then applied to the data at the experimentally observed voltages. The modified acceptance of the deceleration system was found in SIMION and this was compared to the calculated emittances after the quadrupole triplet (see figure 4.24). In one plane there was perfect overlap between the emittance and the acceptance. In the other plane the match was not as good, this suggests that although the experimental configuration may represent a local maxima in the transmission efficiency of the ions a better match may still be possible.

The system was re-simulated in SIMION to try and understand the primary causes of the beam losses. In the simulation the experimentally observed potentials were applied to all but the four-way switch electrodes. These simulations showed 47% transmission of the ion beam into the RFQ with 39% of the beam lost through collisions with the RFQ front plate and the remaining 14% lost in the four-way switch. The experimentally observed drift in the beam current was

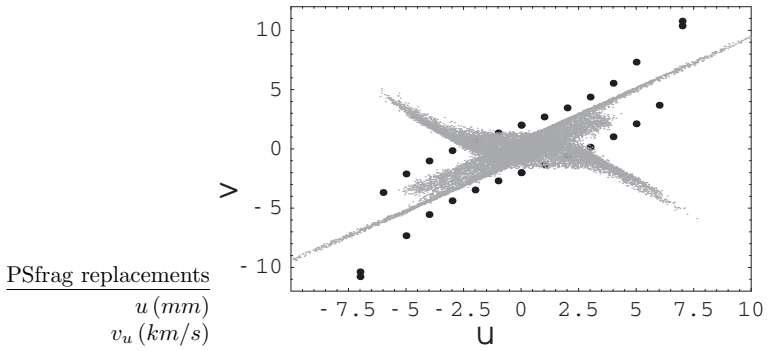

Figure 4.24: Comparison between the new acceptance of the deceleration system and the emittance of the beam as it enters the ground tube.

almost certainly due to a build up of charge somewhere in the injection system. Intuitively it would seem that this drift would most likely occur when the ions are at their lowest energy i.e. at the entrance to the RFQ. However, due to the large potentials on the electrodes in this region it would be very difficult for enough charge to build up to effect the ions trajectories. As the ions pass through the four-way switch they still have high kinetic energy. However, as the detector is a long way downstream of the switch only a small change in the angle with which the ions exit the device would be required to cause the beam current to drift. It therefore seems most probable that the beam drift is caused by charge build up in the four-way switch.

The point of the test ion beam setup is not only to test the RFQ, but also to test the injection and extraction optics for the system. The injection optics were designed around the parameters of the ISAC beam which has rms transverse emittances on the order of $5\,\pi\,mm\,mrad$ and longitudinal energy spreads on the order of $5\,eV$. Simulations of the beam as it exits the four-way switch show that due to filamentation in the first quadrupole triplet the emittance of the beam can be as high as $100\,\pi\,mm\,mrad$ and has a longitudinal energy spread of around $100\,eV$. This is not in anyway representative of the ISAC beam and as such is impossible to test the RFQ within its design parameters.

The filamentation of the beam can either be reduced by changing the length of the first quadrupole triplet or by altering the properties of the beam so that it is better suited to the current triplet. The length of the quadrupole was determined by the size of the cross in which it is mounted and so cannot be altered. The beam extracted from the source was very wide and highly divergent. This means that when it is transported through the quadrupole triplet it's outer edge is always relatively far away from the center of the triplet which increases the effects of filamentation due to the fringe field between the electrodes. The properties of the beam from the source are due to a combination of it's being brought to a sharp focus as it passes through the aperture of the

extractor plate and the long length of the ground tube. It was though that increasing the size of aperture in the extractor plate would change the focal properties of the source so as to make the beam less divergent at the entrance to the quadrupole triplet. However, simulations showed that the effect of this would be small and it would only be possible to move the focal point of the beam by a few millimeters. Another method for altering the beams properties is to collimate it before it enters the first quadrupole. The ideal place for the inclusion of the collimator would be in the field free region inside the extraction cone.

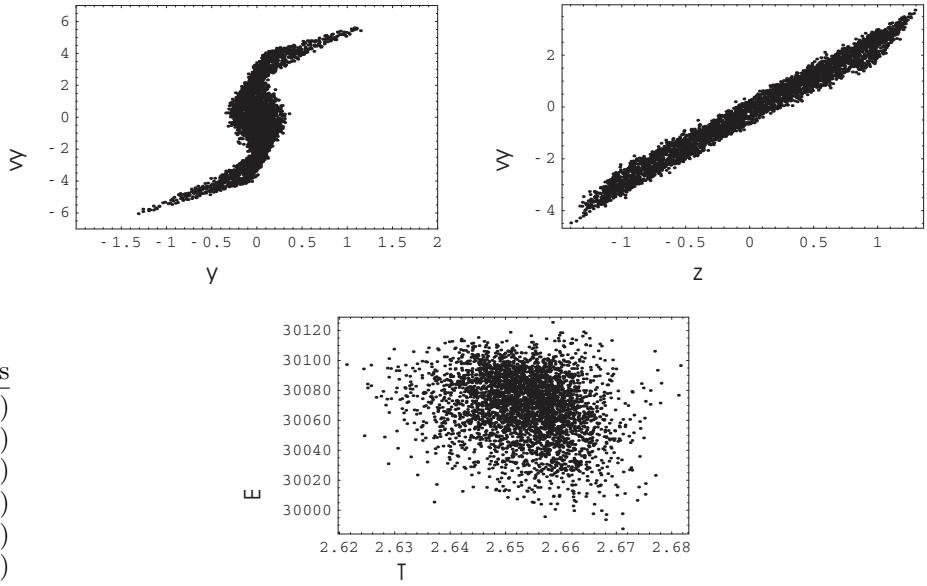

PSfrag replacements
$y\,(mm)$
$z\,(mm)$
$v_y\,(km/s)$
$v_z\,(km/s)$
Energy (eV)
Time of Flight (μs)

Figure 4.25: The emittances of the collimated beam as it exits the four-way switch. The effects of filamentation are still visible but they are greatly reduced.

Simulations were carried out of the system with a $2\,mm$ radius collimator at the exit of the ground tube. The simulations showed that this would reduce the beam intensity by about 50%. The effects of filamentation were found to be much smaller on the collimated beam (see figure 4.25). The emittances of the beam when it left the four-way switch were found to be $\varepsilon_{x_{rms}} = 0.7 \pm 0.01\,eV\mu s$, $\varepsilon_{y_{rms}} = 8.9 \pm 0.1\,\pi\,mm\,mrad$ and $\varepsilon_{z_{rms}} = 4.3 \pm 0.1\,\pi\,mm\,mrad$. These transverse emittances are much closer to that of the ISAC beam and hence are better suited to testing the system. It was found that a 100% match between the transverse acceptance of the deceleration system and the emittance of the collimated beam was possible (see figure 4.26). The longitudinal energy spread was still on the order of $40\,eV$ however further SIMION simulations showed that the collimated beam could be transported into the RFQ with 99.8% efficiency.

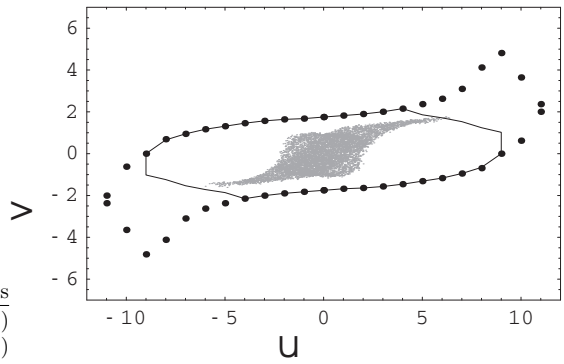

PSfrag replacements
$u\,(mm)$
$v_u\,(km/s)$

Figure 4.26: The emittance of the collimated beam after the second quadrupole overlaps completely with the acceptance of the deceleration optics.

Chapter 5

Summary and Outlook

The motivation for the construction of a gas-filled, square-wave-driven RFQ ion trap was presented. Some practical considerations when designing such a trap were shown using the ideal equations of motion of the ions and a viscous drag model. The acceptance of the trap was calculated as a function of operating parameter q. The maximum acceptance was found to occur at a value for $q \approx 0.32$. The space charge limit of the trap was also investigated. In DC mode it was found that the system could accept a maximum current of around $2.3\,\mu A$ with $q = 0.49$. In pulsed mode a maximum space charge limit of $3.2\,pC$ was found with $q = 0.39$. The temperature of ions in the trap was defined from consideration of the ions motion and well known results from statistical physics.

A Monte Carlo code was written in order to simulate the interaction of ions with a neutral gas. The algorithm improved upon previous work by including a thorough treatment of the interaction probability of the ions with the gas. The code reproduced the experimentally observed mobility of lithium in helium within experimental error. The code was also used to simulate the mobility of cesium in helium with only small deviation from experimental observations. The cooling of cesium in the trap was simulated using the code. The cooling time was found to be around a factor two longer than that predicted by the simple viscous drag model and to be of the order of $600\,\mu s$ at a gas pressure of $2.5 \times 10^{-2}\,mbar$. The final temperature of the of the ion cloud was studied as a function of q. For $q < 0.4$ the final temperature of the ions was found to be less than $400K$ with the temperature rising exponentially as a function of q.

The extraction of the ion beam from the trap was simulated and the final emittance of the cooled beam was found at a value for $q = 0.3$. It was found that the exact emittance of the beam was dependent on the extraction method but for cesium in helium rms transverse emittances on the order of $3\,\pi\,mm\,mrad$ and longitudinal emittances of $2\,eV\mu s$ were obtainable at an extraction energy of $2.5\,keV$.

All the elements needed for a test ion source system have been constructed and testing of the RFQ is underway. SIMION simulations of the ion source optics needed to transport the beam from the ion source to the deceleration system were carried out as per the final design. These showed that only 64% transfer of beam from the test ion source into the RFQ was possible. Experimental results were obtained for the transfer of beam into the RFQ showing only 24% efficiency. The results were interpreted via simulation of the actual system. It was seen that the beam from the test ion source was not representative of the ISAC beam and had longitudinal and transverse emittances that

exceeded the designed acceptance of the deceleration system. However, the simulations also showed that by simply collimating the beam before it enters the first quadrupole triplet a truer representation of the ISAC beam could be obtained. This would eliminate nearly all of the beam losses with 99.8% of the collimated beam making it into the RFQ.

Simulations of the complete cooling system are now at a highly developed level. However, only the cooling of a single ion species has been simulated in any detail. Simulations of the cooling of ions over the complete mass range will be required so as to optimize the cooling process in each mass regime. The effects of ion-ion interactions have also been neglected. These will have to be included in order to truly understand the final properties of the cooled ion clouds. The exact acceptance of the EBIT is still unknown and so it is not clear if the emittance of the cooled bunch will be small enough for good transmission. If further cooling is required, the use of some kind of differential barrier inside the trap may be considered so as to lower the gas pressure in the extraction region and hence the effects of RF heating.

The test setup for the RFQ is constructed and complete. A collimator is being installed in the test ion source and this will allow for better test of the deceleration system. The RFQ has been constructed and tests of the system are underway. An emittance meter is being made so that the beam properties upon extraction from the system can be fully analyzed and compared to simulation.

Bibliography

[Amo02] M. Amorerri et al., *Nature* **419**, 456 (2002).

[Ave04] B. Averth, Private Communication (2004).

[Bar03] M. J. Barnes and G. D. Wait, *Pulsed Power Conference*, (2003).

[Ber02] I. Bergström et al., *Nucl. Instrum. Methods A***487**, 618 (2002).

[Bin04] B. B. Blinov, D. L. Moehring, L. -M. Duan, C. Monroe, *Nature* **428**, 153, (2004).

[Ble36] J. P. Blewitt, *Phys. Rev.* **50**, 464 (1936).

[Blu98] R. Bluhm et al., *Phys. Rev. D* **57**, 3932 (1998).

[Bol96] G. Bollen et al., *Nucl. Instrum. Methods A* **368**, 675 (1996).

[Bol01] G. Bollen, *Nucl. Phys. A* **693**, 3 (2001).

[Bol03] G. Bollen and S. Schwarz, *J. Phys. B* **36**, 941 (2003).

[Bro86] L. S. Brown and G. Gabrielse, *Rev. Mod. Phys.* **58**, 233 (1986).

[Cla04] J. A. Clark et al., *Phys. Rev. Lett.* **92**, 192501 (2004).

[Cou58] E. D. Courant and H. Synder, *Annls. Phys.* **3**, 1 (1958).

[Dah00] D. A. Dahl, *Int. J. Mass Spectrom.* **3**, 200 (2000).

[Daw95] P. H. Dawson, *Quadrupole Mass Spectometry and its applications*, Elsevier Scientific Publishing Company, New York (1995).

[Dil01] J. Dilling, *Direkte Massenmessungen an exotischen Kerne mit SHIPTRAP und ISOLTRAP*, Ph.D. Thesis, Universität Heidelberg (2001).

[Dil03] J. Dilling et al., *Nucl. Instrum. Methods B* **204**, 492 (2003).

[Din02] Li Ding et al., *Int. J. Mass Spectrom.* **221**, 117 (2002).

[Dom02] M. Dombsky et al., *Nucl. Phys. A* **701**, 486 (2002).

[Eid04] S. Eidelman et al., *Phys. Lett. B* **592**, 1 (2004).

[Elf99] M. T. Elford, I. Røeggen and H. R. Skullerud, *J. Phys. B* **32**, 1873 (1999).

[Ell78] H. W. Ellis et al., *Atomic Data and Nuclear Data Tables* **22**, 180 (1978).

[Fer34] E. Fermi, *Z. Phys.* **88**, 161 (1934).

[Flo83] G. Floquet, *Ann. Ecole. Norm. Sup. Paris* **12**, 47 (1883).

[Gab02] G. Gabrielse et al., *Phys. Rev, Lett.* **89**, 213401, (2002).

[Gam36] G. Gamow and E. Teller, *Phys. Rev* **49**, 895 (1936).

[Gra80] G. Gräff et al., *Z. Phys. A* **297**, 35 (1980).

[Had04] O. Hadary, M. Barnes and G. Wait, *Distributed Capacitance of TITAN RFQ Driver and RFQ Structure, Extraction Electrode Considerations and Power Dissipation in the Driver*, TRIUMF Design Note TRI-DN-04-26 (2004).

[Her01] F. Herfurth et al., *Nucl. Instrum. Methods A* **469**, 254 (2001).

[Her03] F. Herfurth et al., *J. Phys. B* **36**, 931 (2003).

[Jok04] A. Jokinen et al., *Phys. Rev. C* **70**, 011301 (2004).

[Kan03] A. Kamdar, private communication (2003).

[Kep02] D. Kielpinski, C. R. Monroe and D. J. Wineland, *Nature* **417**, 709 (2002).

[Kim97] T. Kim, *Buffer Gas Cooling of Ions in a Radio Frequency Quadrupole Ion Guide*, Ph.D. Thesis, McGill University (1997).

[Kob73] M. Kobayashi and T. Maskawa, *Prog. Theor. Phys.* **49**, 652 (1973).

[Kon95] M. Konig et al., *Int. J. Mass. Spectrom.* **142**, 95 (1995).

[Kon02] N. V. Konenkov, M. Sudakov and D. J. Douglas, *J. Am. Soc. Mass. Spectrom.* **13**, 597 (2002).

[Kra88] K. S. Krane, *Introductory Nuclear Physics*, John Wiley and Sons (1988).

[Kug92] E. Kugler et al., *Nucl. Instrum. Methods B* **70**, 41 (1992).

[Lan04] K. Langanke, *Lect. Notes Phys.* **652**, 173 (2004).

[Law00] A. M. Law and W. D. Kelton, *Simulation, modeling and analysis*, McGraw-Hill (2000).

[Law77] J. D. Lawson, *The physics of charged-particle beams*, Claredon Press - Oxford (1977).

[Lun03] D. Lunney, J. M. Pearson and C. Thibault, *Rev. Mod. Phys.* **75**, 1021 (2003).

[McD73] E. W. McDaniel and E. A. Mason, *The Mobility and Diffusion of Ions in Gases*, John Wiley and Sons (1973).

[Mei18] E. Meissner, *Schweizer Bauzeitung* **72**, 95 (1918).

[Mon95] C. Monroe et al., *Phys. Rev. Lett.* **75**, 4011 (1995).

[Mor03] D. J. Morrissey et al., *Nucl. Instrum, Methods B* **204**, 90 (2003).

[Mun79] G. Münzenberg et al., *Nucl. Instrum. Methods A* **161**, 65 (1979).

[Nie01] A. Nieminen et al., *Nucl. Instrum. Methods A* **469**, 244 (2001).

[Par95] J. H. Parks and A. Szoke, *J. Chem. Phys.* **103**, 1422 (1995).

[Pen97] H. Penttilä et al., *Nucl. Instrum. Methods B* **126**, 213 (1997).

[Pip53] L. A. Pipes, *J. App. Phys.* **24**, 902 (1953).

[Rai03] S. Rainville, J. K. Thompson and D. E. Pritchard, *Science* **303**, 334 (2004).

[Ric73] J. A. Richards et al., *Int. J. Mass Spectrom. and Ion Phys.* **12**, 339 (1973).

[Rob03] S. Robertson and Z. Sternovsky, *Phys. Rev. E* **67**, 046405 (2003).

[Rol88] C. E. Rolfs and W. S. Rodney, *Cauldrons in the Cosmos*, University of Chicago Press (1988).

[Sav97] G. Savard et al., *Nucl. Phys. A* **626**, 353 (1997).

[Sch98] S. Schwarz, *Manipulation radioaktiver Ionenstrahlen mit Hilfe einer Paulfalle und direkte Massenmessungen an neutronenarmen Quecksilberisotopen mit dem ISOLTRAP-Experiment*, Ph.D. Thesis, Universität Mainz (1998).

[Sik03] G. Sikler et al., *Nucl. Instrum. Methods B* **204**, 482 (2003).

[Sud02] M. Sudakov and E Nikolaev, *Eur. J. Mass. Spectrom.* **8**, 191 (2002).

[Tan03] U. Tanaka et al., *J. Phys. B* **36**, 545 (2003).

[Tan95] J. N. Tan, J. J. Bollinger and D. J. Wienland, *Proc. Fifth Symp. on Frequency Standards and Metrology*, 427 (1995).

[Tho94] R. C. Thompsom et al., *J. Mod. Opt.* **41**, 1087 (1994).

[Tol67] R. C. Tolman, *The Principles of Statistical Mechanics*, Oxford University Press (1967).

[Tow03] I. S. Towner and J. C. Hardy, *J. Phys. G* **29**, 197 (2003).

[Van01] R. S. Van Dyck Jr., S. L. Zafonte and P. B. Schwinberg, *Hyperfine Interactions* **132**, 163 (2001).

[Vaz02] J. Vaz, *Precision Mass Measurements of Some Isotopes of Platinum*, Ph.D. Thesis, University of Manitoba (2002).

[Wan66] G. H. Wannier, *Statisitical Physics*, John Wiley and Sons (1966).

[Wer03] G. Werth et al., *Nuc. Instrum. Methods B* **205**, 1 (2003).

[Wil03] D. H. Wilkinson, *J. Phys. G* **29**, 189 (2003).

[Wol87] H. Wollnik, *Optics of Charged Particles*, Academic Press Inc. (1987).

Appendix A

Penning Trap Mass Spectrometry

A.1 Mass Measurements with a Penning Trap

The motion of an ion in an ideal Penning trap is the superposition of three harmonic oscillations. The first is simply the motion of the ion in the applied magnetic field, with frequency ω_-, and is known as the magnetron motion, the second is the harmonic oscillation of the ion in the applied electrostatic field, with frequency ω_z, and is known as the axial motion and the third is due to the precession of the ion's magnetic moment in the applied electric field, with frequency ω_+, and is known as the reduced cyclotron motion. The true cyclotron frequency of an ion in such a trap is given by [Bro86]:

$$\omega_c^2 = \omega_+^2 + \omega_-^2 + \omega_z^2, \tag{A.1}$$

and is related to the ion's charge-to-mass ratio by:

$$\omega_c = \frac{q}{m} \cdot B, \tag{A.2}$$

where q is the ion's charge, m is it's mass and B is the strength of the applied magnetic field. Hence, if both the applied field and the charge of the ion are known a measurement of the cyclotron frequency will yield the ion's mass. There exist two well known methods by which the cyclotron frequency of a single ion held in a Penning trap can be measured:

- The Time of Flight (TOF) method [Gra80]. The magnetron and reduced cyclotron motions of an ion in a Penning trap can be coupled via the application of a quadrupolar electric field of maximum amplitude E_0 [Kon95] with components:

$$\begin{aligned} E_x &= E_0\ y\ \cos(\omega_0 t), \\ E_y &= E_0\ x\ \cos(\omega_0 t). \end{aligned} \tag{A.3}$$

  Such a field causes an oscillatory conversion of the high radial energy cyclotron motion into the low radial energy magnetron motion and back again, with periodicity T_r, when the resonance frequency $\omega_0 = \omega_c$ is applied.

An ion orbiting in a magnetic field oriented in the z- direction has magnetic moment:

$$\vec{\mu} = (\frac{E_r}{B})\hat{z}, \tag{A.4}$$

where E_r is the radial energy of the ion. This radial energy is given simply by:

$$E_r = \frac{1}{2}m\left((\omega_-\rho_-)^2 + (\omega_+\rho_+)^2\right), \tag{A.5}$$

where ρ_- and ρ_+ are the amplitudes of the magnetron and reduced cyclotron motions respectively. If such an ion is pulled (electrostatically) through a magnetic field gradient that is aligned with the z- axis the resulting force in the z- direction is:

$$F_z = -\frac{\mathrm{d}}{\mathrm{d}z}\ \vec{\mu}\cdot\vec{B}(z). \tag{A.6}$$

Hence, we see that the ions radial energy will be converted into longitudinal kinetic energy. Thus a measurement of the time it takes for an ion to traverse a fixed distance after this conversion will yield a relative measure of the ions initial radial energy.

If an ion is prepared in a state such that it is initially in a pure low energy magnetron motion and then a quadrupolar field is applied, at the resonant frequency, for a time $t = \frac{n}{2}T_r$, where n is an integer, then the pure magnetron motion will be converted into a pure reduced cyclotron motion. The radius of the ions cyclotron motion after the conversion will be identical to the radius of the ions magnetron motion before the conversion. The angular frequency of the reduced cyclotron motion is typically much larger ($\omega_+ \gg \omega_-$) than that of the magnetron motion and as such the ion has higher radial energy after the conversion. If the frequency of the applied quadrupolar field is slightly shifted from that of the resonant frequency the conversion will not be complete. Thus, by looking at the time of flight of the ions as a function of the applied frequency of the quadrupolar field a measurement of the cyclotron frequency can be made (see figure A.1).

- The fast Fourier Transform Ion Cyclotron Resonance (FT-ICR) method. For this non-destructive method the image currents induced in the trapping electrodes are detected when the ions oscillate under the effect of the applied fields (see figure A.2). The Fast Fourier Transform of the image current yields both ω_z and ω_+ directly and using the fact that [Bro86]:

$$\omega_- = \frac{\omega_z^2}{2\ \omega_+}, \tag{A.7}$$

the cyclotron frequency can be found. For this method to work accurately it is necessary to use a resonant circuit with a large suppression of the electronic noise produced by the detection equipment.

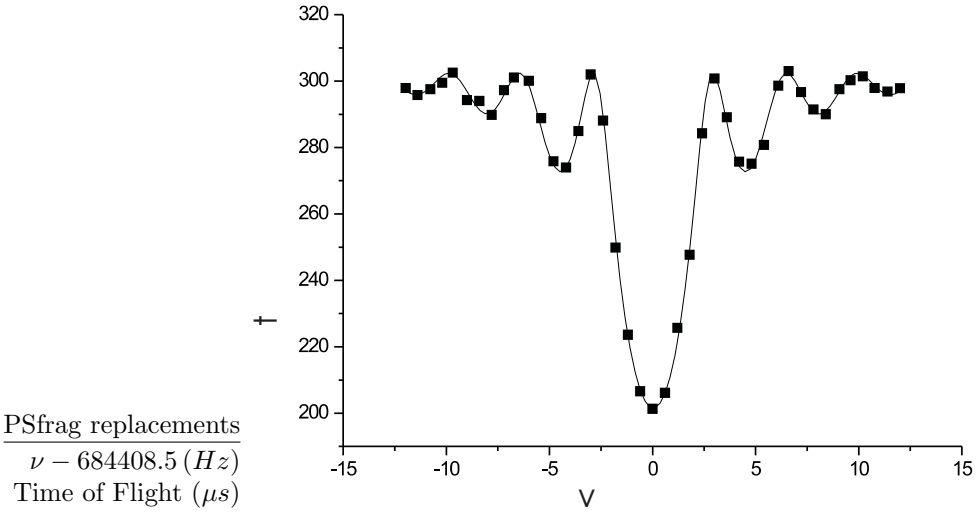

Figure A.1: TOF spectrum from a measurement of the mass of cesium 133. Taken from [Dil01].

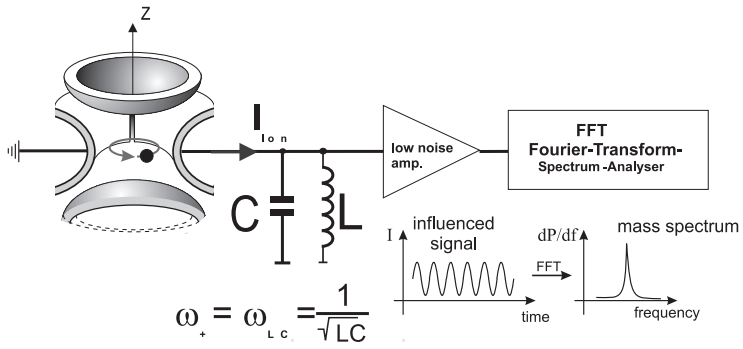

Figure A.2: A typical setup for the FT-ICR method. The induced signal is passed through a parallel LC circuit, to filter out noise, before it is amplified. The Fourier transform of the signal is then taken. From [Dil01].

A.2 Facilities for Precision Mass Measurements

In this section an overview of the state of the art Penning trap mass measurement systems is given. The first part gives details of off-line systems for stable ions where relative accuracies of up to 1×10^{-11} have been reached. The second part looks at systems for short-lived radioactive ions. In such systems not only are the ions unstable, and hence shorter time is available for the measurement, but also the ions are produced outside of the trap and hence have to be prepared for injection into the Penning trap mass spectrometer.

A.2.1 Off-Line Facilities

- MIT ICR. A Penning trap system developed by D. E. Pritchard's group at the Massachusetts Institute for Technology (MIT), and successfully operated for over ten years, it recently relocated to Florida State University. The MIT ICR trap is a cryogenically cooled Penning trap mass spectrometer where ions are created in the trap via the ionization of a neutral gas. The group has developed a system for directly comparing the relative frequencies of two different species of ions in the trap at the same time, one reference mass and one ion of interest, via the FT-ICR method [Rai03]. This allows them to reduce a number of the systematic uncertainties associated with precision traps, most importantly fluctuations in the magnetic field. Mass measurements have been demonstrated with accuracies of $\delta m/m \approx 1 \times 10^{-11}$.

- SMILETRAP. The SMILETRAP facility, located at the Manne Siegbahn laboratory in Stockholm, uses an EBIS (Electron Beam Ion Source) in order to produce a highly charged beam of stable ions. These are subsequently past through an analyzing magnet, in order to select a specific charge-to-mass ratio, before injection into a cylindrical Penning trap. The ions are then passed into a hyperbolic Penning trap where mass measurements are made via the TOF method [Ber02]. Measurements have been made on a number of ions with accuracies in the range of $\delta m/m \approx 1 \times 10^{-9}$ to 1×10^{-10}.

- UW-PTMS. The PTMS (Penning Trap Mass Spectometry) group at the University of Washington uses a cryogenically cooled precision Penning trap in order to make mass measurements via the FT-ICR method [Van01]. Cooling the trap lowers the pressure inside the trap to around $1 \times 10^{-18}\, mbar$ thus reducing the effects of collisions with contaminants in the trap. This allows them to achieve accuracy of the order of $\delta m/m \approx 1 \times 10^{-10}$.

A.2.2 On-Line Facilities

- ISOLTRAP. Radioactive ion beams are created at the ISOLDE facility at CERN, Geneva, via the ISOL (Isotope Separator On-Line) method [Kug92]. The $60\, keV$ ion beam produced is collected in a gas-filled RFQ,

then transferred to a gas-filled Penning trap, for isobar separation, before being passed into a $6\,T$ precision Penning trap where the mass measurements are made using the TOF method [Bol96].

The ISOLTRAP group was the first to show that Penning trap mass spectrometry could be performed on short-lived species. The system has since been used to measure the masses of over 250 nuclides to an accuracy of around $\delta m/m = 5 \times 10^{-8}$ for half-lives of around $50\,ms$ [Her03].

- JYFLTRAP. At the cyclotron laboratory of the University of Jyväskylä, Finland, the IGISOL (Ion Guide Isotope Separator On-Line) method is employed in order to produce low energy (40 to $60\,keV$) heavy ion beams [Pen97]. The quality of these beams is then improved by the use of a gas-filled RFQ before injection into a tandem (isobar separator and precision trap) $6\,T$ Penning trap system for mass measurements. This trap came on-line in 2003 and made its first measurements on some zirconium isotopes ($t_{1/2} \approx 1\,s$) with $\delta m/m \leq 5 \times 10^{-7}$ [Jok04].

- SHIPTRAP. Medium to heavy mass radionuclides are produced via fusion-evaporation reactions at the SHIP (Separator for Heavy Ion reaction Products) at GSI Darmstadt with energies of around $100\,keV/u$ [Mun79]. This beam is then slowed down to thermal energies in a high pressure ($\approx 100\,mbar$) gas stopping cell, extracted and bunched in an RFQ, before injection into a $6\,T$ tandem Penning trap system. Results of the first on-line measurements were published in 2003 [Sik03].

- CPT. The Canadian Penning Trap is currently situated at the Argonne National Laboratory, USA. Beam from the ATLAS accelerator hits a solid target producing high energy recoil products ($E \approx 50\,MeV/u$) which are then put through an Enge magnetic separator. The beam is decelerated using a gas stopping cell, then cooled and bunched in a gas-filled RFQ, it is further passed through an additional Paul trap for isobar separation before injection into a $6\,T$ precision Penning trap [Sav97]. The masses of around 100 unstable ion species have been measured with a typical precision of $\delta m/m = 1 \times 10^{-8}$ for half-lives as low as $1\,s$ [Cla04].

- LEBIT. Located at Michigan State Universities National Superconducting Cyclotron Laboratory (MSU/NSCL), construction and testing of the LEBIT (Low Energy Beam and Ion Trap) system is nearing completion [Bol03]. The device uses a gas stopping cell in order to thermalize the high energy beam ($E \geq 100\,MeV/u$) delivered by the A1900 fragment separator [Mor03]. The beam is subsequently extracted from the cell and delivered to a $9.4\,T$ Penning trap system using first a gas filled linear Paul trap for cooling and then a second linear trap where the beam is bunched.

Appendix B

Emittance and Acceptance

B.1 The Concept of Emittance

The quality of an ion beam is best described using the concept of emittance. The ideal ion beam is a group of identical particles all travelling with the same velocity, i.e. in a common direction of motion. However, in reality such an ideal beam is not achievable. Instead the ions will have a small spread in energy, (for on-line facilities typically 1 to 100 eV) which is characteristic of the ion production and acceleration method, as well as having small angular divergences (typically 1 to 100 $mrad$) from the common direction of motion (see figure B.1). In order to quantify how the properties of a beam differ from the ideal case we

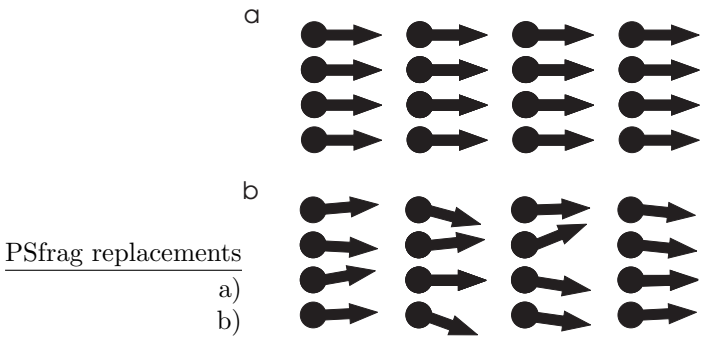

Figure B.1: a) In an ideal beam all the particles have identical velocities. b) In a more realistic beam the ions have velocities that deviate slightly from the ideal case.

can define three emittances as the areas that the beam occupies in momentum-position phase space with respect to three cartesian coordinate axes. The ideal beam has zero emittance. The larger the emittance of the beam the further it deviates from the ideal case. If we define the z- axis as the common direction of motion of our beam it is usual to denote the area occupied in the (x, p_x) and the (y, p_y) phase spaces as the transverse emittances and the area in the (z, p_z) phase space as the longitudinal emittance. Using the small angle approximation it is easy to show that the transverse velocities of the ions are proportional to their angular divergences. Hence, it is common to give transverse emittances as the area occupied in the (x, θ_x) and (y, θ_y) spaces in units of $\pi \cdot mm \cdot mrad$.

It is also common practice to give the longitudinal emittance as the area of the beam in energy-time phase space, in units of $eV \cdot \mu s$.

An ion beam can be considered to be a cloud of particles in six dimensional phase space, (x, y, z, p_x, p_y, p_z), with each of the individual particles following its own unique temporal evolution. According to Liouville's theorem, the volume of such a cloud will remain constant as a function of time under the application of conservative forces even though the shape of the cloud will, in general, change [Tol67]. If, as is generally the case, the forces acting in the x-, y- and z- directions are independent of each other then the areas of the three individual sub-spaces, (x, p_x), (y, p_y) and (z, p_z), must also be conserved even though the shape of their boundaries can change with time. Therefore according to Liouville's theorem the three emittances of an ion beam are constant under the application of conservative forces.

B.2 The Concept of Acceptance

When designing electromagnetic devices to transport, manipulate and analyze ion beams it is important to ensure that the devices make efficient use of the beam. This is even more so when operating with radioactive nuclei where production methods are fairly cumbersome and often only small production yields can be achieved.

Consider the simple example of a narrow drift tube; if the beam entering the tube is too wide the edges of the beam will be lost (see figure B.2a) and if the beam entering the tube is too divergent then it will hit the walls (see figure B.2b). From this simple example we can see that the tube has an acceptance profile in position-momentum phase space, in order for the beam to be transported through the tube without losses it is necessary for the transverse emittance of the beam to overlap completely with this acceptance profile.

PSfrag replacements
a)
b)

Figure B.2: (a) A wide parallel beam enters a narrow tube. A large proportion of the beam is lost. (b) A narrow diverging beam enters a narrow tube. Again a large proportion of the beam is lost.

Consider the example of an electrostatic barrier with an ion beam incident on it. If the height of the barrier is set equal to the mean kinetic energy of the incoming beam then all the ions with kinetic energies less than the mean will be stopped whereas ions with kinetic energies greater than the mean can pass

the barrier. Now, consider a voltage supply used to bias the potential barrier with an inherent ripple such that the barrier height oscillates between a value slightly less than the lowest energy of the beam and a value slightly higher than the highest energy of the beam, in this case the number of ions passing the barrier will oscillate as a function of time (see figure B.3). This system has an acceptance in energy-time phase space and again for a beam to pass through the system without losses its longitudinal emittance must completely overlap with this acceptance.

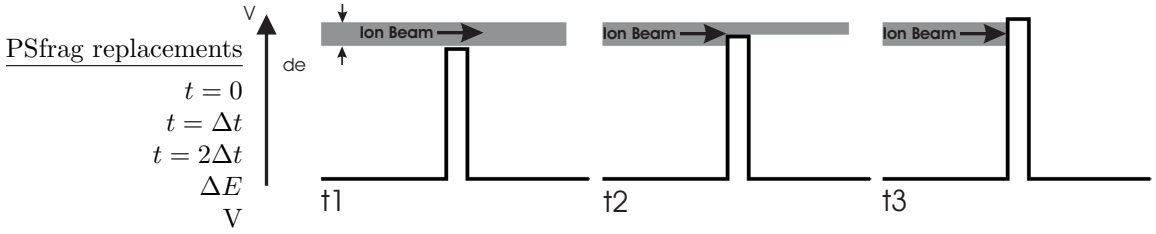

Figure B.3: A beam with energy spread ΔE impinges on a electrodynamic barrier. At time $t = 0$ all the beam passes above the barrier whereas at time $t = 2\,\Delta t$ the whole beam is stopped.

In general, we conclude that all physical systems have an acceptance in six dimensional phase space. Efficient transport of an ion beam through a system relies on the matching of the beam emittance to the system's acceptance. If the beam's volume in phase space completely overlaps with the systems acceptance then the beam will be transported through the system without loss.

B.3 Mathematical Description of Emittance

The definition of emittance presented here is that typically used for lower energy non-relativistic beams. This definition is not normalized meaning that direct comparisons between the emittances of beams with different energies should not be made. For a good overview of the material presented see [Law77].

In practice the best ion beams achievable are produced with Gaussian profiles in both position and velocity. This means that the distribution of particles in position-momentum space can be described by a two dimensional Gaussian with the rms emittance defined as the area, A, of the ellipse bounding the distribution at one standard deviation divided by π (see figure B.4):

$$\varepsilon_{rms} = \frac{\mathrm{A}}{\pi}, \tag{B.1}$$

Such an ellipse is typically defined using the Twiss parametrization where:

$$\varepsilon_{rms} = \gamma x^2 + 2\alpha x\dot{x} + \beta\dot{x}^2, \tag{B.2}$$

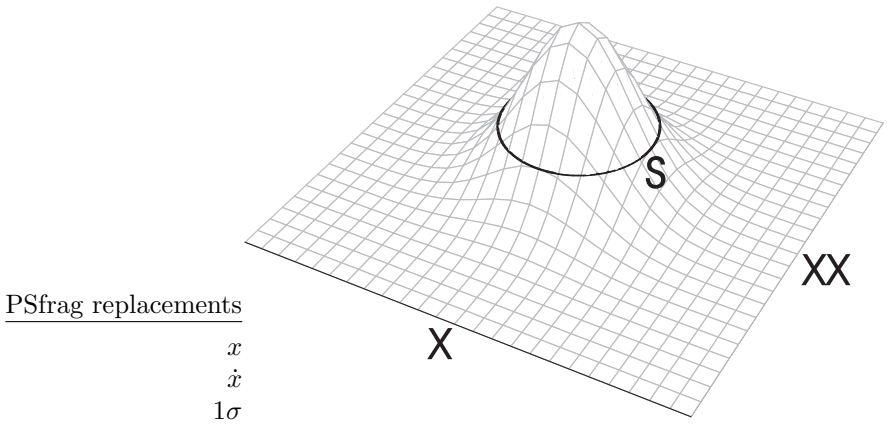

Figure B.4: The rms emittance is defined as the area of the ellipse bounding the normal distribution at one standard deviation divided by π.

and:

$$x_{max} = \sqrt{\varepsilon_{rms}\beta}, \tag{B.3}$$

$$\dot{x}_{max} = \sqrt{\varepsilon_{rms}\gamma}, \tag{B.4}$$

$$x' = \alpha(\varepsilon_{rms}/\gamma)^{\frac{1}{2}}, \tag{B.5}$$

$$\dot{x}' = \alpha(\varepsilon_{rms}/\beta)^{\frac{1}{2}}, \tag{B.6}$$

$$\beta\gamma - \alpha^2 = 1, \tag{B.7}$$

where x_{max}, $\dot{x}_{max}$, x' and $\dot{x}'$ are defined as shown in figure B.5).

The sigma matrix is also another common representation of the emittance where:

$$\sigma = \varepsilon_{rms} \begin{pmatrix} \beta & -\alpha \\ -\alpha & \gamma \end{pmatrix} = \begin{pmatrix} \sigma_{11} & \sigma_{12} \\ \sigma_{12} & \sigma_{22} \end{pmatrix}, \tag{B.8}$$

$$\sigma_{11} = x_{max}^2, \tag{B.9}$$

$$\sigma_{22} = \dot{x}_{max}^2. \tag{B.10}$$

The emittance is given by:

$$\varepsilon_{rms} = \sqrt{|\sigma|} = \sqrt{\sigma_{11}\sigma_{22} - \sigma_{12}^2}. \tag{B.11}$$

In the field of optics lenses, prisms and mirrors are used to control the passage of light through a system. In ion optics electromagnetic fields are used to control the passage of charged particles through a system. In analogy to the well know matrix method in optics it is possible to define a transfer matrix, $\boldsymbol{M}$, for a system of ion optics such that:

$$\begin{pmatrix} x \\ \dot{x} \end{pmatrix}' = \boldsymbol{M} \begin{pmatrix} x \\ \dot{x} \end{pmatrix} = \begin{pmatrix} m_{11} & m_{12} \\ m_{21} & m_{22} \end{pmatrix} \begin{pmatrix} x \\ \dot{x} \end{pmatrix}. \tag{B.12}$$

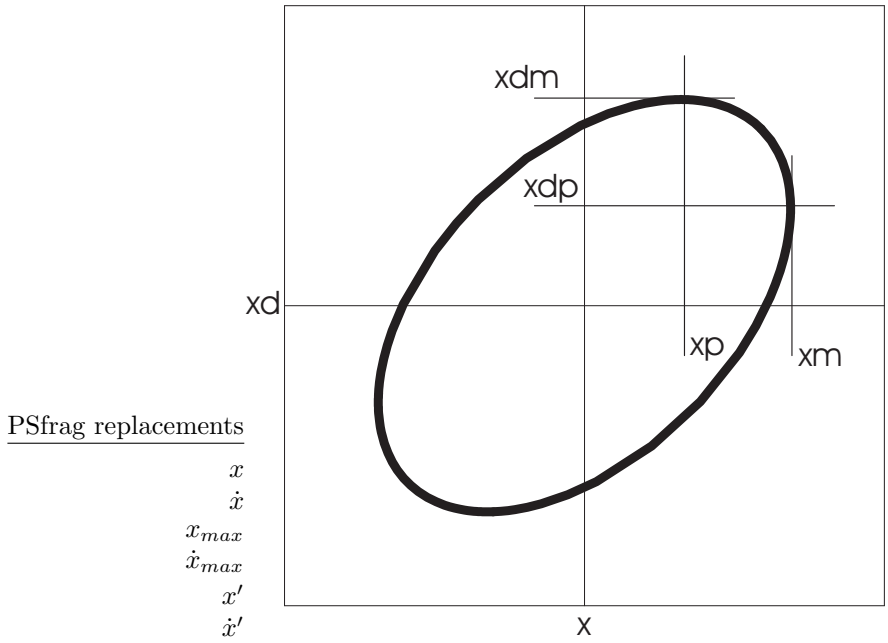

Figure B.5: The Twiss parameters of an ellipse can be related to the points shown (see equations B.3, B.4, B.5 and B.6).

If the transfer matrix for a system is know the transformation of the beams sigma matrix as it passes through the system can be calculated as:

$$\sigma' = \boldsymbol{M}\sigma\boldsymbol{M}^T \tag{B.13}$$

where $\boldsymbol{M}^T$ is the transpose of the matrix $\boldsymbol{M}$.

The Gaussian density distribution of the beam in position-momentum phase space can be expressed in terms of the sigma matrix coefficients as:

$$\rho(x, \dot{x}) = \frac{1}{2}\pi\varepsilon_{rms}\exp[-\frac{1}{2}\vec{x}^T\sigma^{-1}\vec{x}], \tag{B.14}$$

where:

$$\vec{x} = \begin{pmatrix} x \\ \dot{x} \end{pmatrix}. \tag{B.15}$$

Hence, if the density distribution of the particles is measured the emittance can be found by fitting a Gaussian to it. However, if the beam is not Gaussian the more general relationship:

$$\varepsilon_{rms} = 4\sqrt{\langle x^2\rangle\langle\dot{x}^2\rangle - \langle x\dot{x}\rangle^2}, \tag{B.16}$$

can be used to determine the emittance, where the angle brackets, $\langle\rangle$, denote the average of the values over the two dimensional phase space.

$\varepsilon/\varepsilon_{rms}$	1/4	1	4	6	9
Percentage of particles enclosed	15	39	87	95	99

Table B.1: Scaling factors to convert rms emittance into other commonly used forms.

The rms emittance of a beam encompasses around 39% of its ions. Different definitions of emittance in common use give the area in phase space containing other percentages of the beam. For a Gaussian beam the rms emittance can be easily converted to the emittance containing any percentage of the beam by multiplication of a scaling factor. Some typical scaling factors are given in table B.1.

Appendix C

The Square-Wave Generator

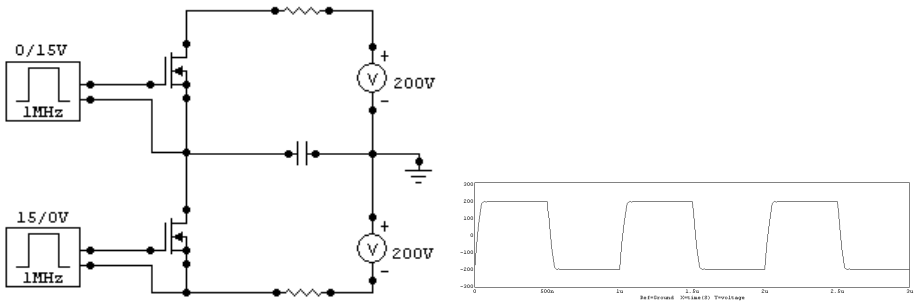

Figure C.1: A simple push-pull system for creating a high amplitude square-wave. The wave is generated by alternatively forward biasing the gate-source junctions of the MOSFETs. Each trigger floats at the respective source voltage. This ensures that the MOSFETs remain forward biased as the source voltage changes. The waveform shows the voltage between the MOSFETs as a function of time.

The square-wave was generated using fast switching MOSFETs (Metal-Oxide-Semiconductor Field-Effect Transistor). A simple signal amplifier can be generated by using two such MOSFET's in a push-pull configuration (see figure C.1). A method for stacking a series of MOSFETs such that high voltages, $V \leq 25\,kV$, could be switched with repetition rates of up to $77\,kHz$ had already been developed at TRIUMF for use in the MuLan experiment at the Paul Scherrer Institute in Switzerland [Bar03]. Each MOSFET was placed on a separate circuit board electrically isolated from ground. Power was magnetically coupled to the board via an inducting core and the trigger signal relayed fiber optically. This meant that the common voltage on each board could follow the voltage on the MOSFET's source ensuring that the gate-source junction remained forward biased regardless of the voltage on the source. The square wave generator used was based on this system. The whole system can simply be considered as a square-wave-driven RC circuit. The RFQ presents a capacitative load, along with the capacitance of the MOSFETs themselves and the capac-

itance of all the wires etc used to connect the driver to the RFQ rods. There is also a resistance in the circuit so as to limit the current passing through the MOSFETs. The repetition rate is limited by the rise time of the voltage which is dependant on the RC time constant for the circuit. The system was designed to switch a maximum peak-to-peak voltage of $400\,V$ at frequencies of up to $1\,MHz$. Two stacks of three DE375-102N12A MOSFETs from Directed Energy Incorporated were used to create each phase of the square-wave. These MOSFETs have fast switching times ($\approx 5\,nS$), can operate with a maximum voltage between the drain and the source equal to $1\,kV$ and can be operated with a maximum current between the collector and the emitter of $72\,A$. To generate a square wave of $400\,V_{pp}$ only requires two MOSFETs. However, by stacking the chips the power dissipated by each of the chips is reduced increasing the maximum frequency at which it is possible to drive the MOSFETs. Staking the MOSFETs also has the desirable effect of reducing the total capacitance of the stack as their individual capacitances add in series. It also allows for further MOSFETs to be added in the future making it possible to switch voltages larger than $1\,kV$. Detailed simulations and experimental measurements of the total capacitance of the RFQ system were carried out and the total capacitance found to be around $1500\,pF$ [Had04]. Assuming that the system is symmetrical this means that each pair of rod represents a capacitance of $750\,pF$. A resistance of $75\,\Omega$ was used to limit the current through the MOSFETs. This gives an RC time constant for the circuit of $\tau = 56\,ns$ and a rise time ($10\% \rightarrow 90\%$) equal to $124\,ns$. At an operating frequency of 1 MHz the combined rise and fall time is approximately 10% of the period of the applied RF.

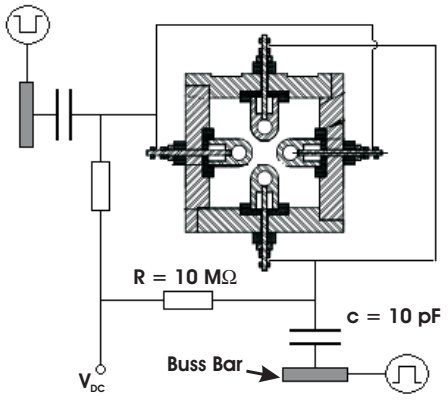

Figure C.2: The AC potential is coupled to the electrodes via a capacitor and the DC potential via a resistor. A resistance is chosen that is large compared to the impedance of the RFQ such that the AC signal doesn't flow into the DC supply.

The system was constructed and tested by driving the RFQ rod structure.

To minimize the length and hence the capacitance of the connecting wires the driver was mounted on the lid of the RFQ box. The square-wave was then put onto the RFQ electrodes via coupling capacitors (see figure C.2). The voltage over the MOSFETs was supplied by a single supply. A square-wave was generated between $400\,V$ and ground. The coupling capacitors converted this to a wave between $\pm 200\,V$. The longitudinal potential was supplied from separate DC power supplies and then added to the AC signal using coupling resistors. The value of the resistance, $10\,M\Omega$, was chosen such that it was much larger than the impedance of the RFQ. This ensured that the RF did not flow into the DC supply. The resulting waveform is shown in figure C.3. The fall time on channel two is longer than expected. This is because all of the required $75\,\Omega$ current limiting resistors had not been obtained from the manufacturers at the time the image was taken and so a higher resistance was used.

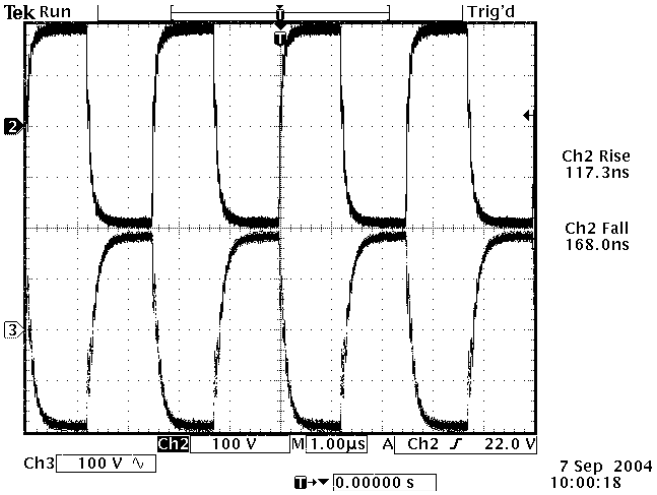

Figure C.3: Oscilloscope screen shot of both phases of the applied waveform taken directly from the RFQ rods. Both waves have a $400\,V$ peak-to-peak amplitude and are set to oscillate at a frequency of $500\,kHz$.

The pulsing of the potential on the electrodes in the trapping region required to extract the ions from the trap is simply achieved by switching the DC bias applied to the RF field. For this purpose a simple two MOSFET switch was used. Such a switch had previously been developed at McGill University. The switch provides pulses of $100\,\mu s$ duration at frequencies of up to $2\,kHz$ with rise times less than $10\mu s$.